Improved Frequency Domain Measurement Techniques for Characterizing Power Amplifier and Multipath Environments

A Dissertation
Presented to
The Academic Faculty

by

Michael Dean McKinley

In Partial Fulfillment
of the Requirements for the Degree
Doctor of Philosophy in
Electrical and Computer Engineering

Georgia Institute of Technology
August, 2008

Improved Frequency Domain Measurement Techniques for Characterizing Power Amplifier and Multipath Environments

Approved by:

_____
Dr. J. Stevenson Kenney, Advisor

_____
Dr. Madhavan Swaminathan

_____
Dr. Gregory D. Durgin

Date approved:_____

This dissertation is dedicated to

my father and mother,

my father-in-law and mother-in-law,

my dear wife, Susan,

and

the Holy Trinity

Acknowledgements

A great many persons and organizations have helped me make this dissertation possible. First of all, I am forever indebted to my advising professor, J. Stevenson Kenney. Prof. Kenney provided me with many years of research assistantships. Amidst the many demands on him, Prof. Kenney carved out generous amounts of time for his students. His advisement, insight and flexibility were invaluable to my research at Georgia Tech. Furthermore, his high standards of integrity engendered trust and loyalty. I am truly grateful for the privilege of studying under Prof. Kenney.

I also greatly appreciate my advisor at NIST, Dr. Kate Remley. Dr. Remley gave me the opportunity to work with her at NIST in Boulder, CO. Her amiability made me look forward to every work day. Her technical acumen and eye for detail helped make my measurements worth seeing and my finished papers worth reading.

I am grateful to the members of my dissertation committee, Prof. J. Stevenson Kenney, Prof. Gregory D. Durgin and Prof. Madhavan Swaminathan, for their willingness to critique this dissertation. I am grateful to Dr. Michael Trippe of ANADIGICS for participating in reviewing this dissertation and to Dr. Wyman Williams of ANADIGICS for reviewing the multipath sections of the dissertation.

Special thanks go to my colleagues Hyunchul Ku, who started me out measuring power amplifiers using two-tone tests, and to Youngcheol Park, who helped me source errors in my power amplifier measurements.

Special thanks also go to several persons at NIST for their help. Dr. Dylan Williams' critiques of my papers and presentations were especially helpful. Maciek Myslinski first generated the 55-tone multisine that were used in the multipath

measurements. Dr. Andrew Dienstfrey gave considerable aid in determining the mathematics of spectral smearing. Dr. Robert Johnk, Dr. Dennis Camell and Galen Koepke gave generously of their antenna supplies, cable supplies and time for the multipath measurements.

Special thanks go to Danam Corporation for their supply of power amplifiers to test and for Eungsic Park's help in measuring them. I am grateful to Cree, Inc. for supplying many of our power amplifiers. I am thankful to Public Safety for sponsoring the multipath work at NIST. I am thankful for the willing participation of the following members from industry when publishing a paper on a vector signal analyzer technique: Ken Voelker, product manager, Agilent Technologies; Abhay Samant, RF software group manager, National Instruments; Bill Byrom, application engineer, Tektronix; Kevin Thomason, application engineer, Rohde and Schwarz; Eric Hakanson, design engineer, Anritsu Company.

I also wish to thank my father and mother. They gave my three siblings and me unique visions for our specific talents. While loving us with all their hearts, they challenged us to take on difficult endeavors and encouraged us through them. I am forever grateful for them.

I am thankful to my father-in-law and mother-in-law for giving me a family here in Atlanta and for giving me my wonderful wife.

My dear wife, Susan, supported me sacrificially throughout my time at Georgia Tech. Though a native of Atlanta, she took it in stride when an internship opportunity arose in Colorado and dealt with the many logistics it presented. For one averse to

change, she adjusted well to my nomadic existence and still encouraged me greatly along the way.

Last but not least, I thank the Holy Trinity. God has guided me, helped me and been a refuge to me in my many times of need. I am eternally grateful.

Table of Contents

List of Figures

List of Tables

List of Abbreviations

16QAM	16-symbol quadrature amplitude modulation
64QAM	64-symbol quadrature amplitude modulation
AC	alternating current
ACLR	adjacent channel leakage ratio (a.k.a. ACPR)
ACPR	adjacent channel power ratio (a.k.a. ACLR)
ADC	analog-to-digital converter
AM	amplitude modulation
AM/AM	amplitude-to-amplitude modulation (distortion)
AM/PM	amplitude-to-phase modulation (distortion)
AR	ADC amplitude resolution
ARB	arbitrary waveform generation function
AWGN	additive white Gaussian noise
BER	bit error ratio
BPSK	binary phase-shift keying
CCI	co-channel interference
CDMA	code-division multiple access
CP	cyclic prefix
DC	direct current
DFT	discrete Fourier transform
DMM	digital multimeter
DSRC	Dedicated Short-Range Communication
DUT	device under test
EVM	error vector magnitude
FDM	frequency-division multiplexing
FDMA	frequency-division multiple access
FER	frame error ratio
FFT	fast Fourier transform
FOM	figure of merit
IFFT	inverse fast Fourier transform
IIR	infinite impulse response (function)
IMD	intermodulation distortion
IMD3	third-order intermodulation distortion
IMD5	fifth-order intermodulation distortion
IMD7	seventh-order intermodulation distortion
ISI	inter-symbol interference
LAN	local-area network
LDMOS	laterally-diffused metal-oxide-semiconductor field-effect transistor
LDMOS	laterally-diffused MOS
LN	linear and nonlinear (behavioral model)
LOS	line of sight
LQTI	linear quasi-time-invariant (channel)

LSNA	large-signal network analyzer
LTI	linear time-invariant (channel)
LTV	linear time-varying (channel)
MER	memory effects ratio
MEVM	multisine error vector magnitude
NTI	nonlinear time-invariant (channel)
OFDM	orthogonal frequency-division multiplexing
OIP3	third-order output intercept point
OV	overvoltage
PA	power amplifier
PAPR	peak-to-average power ratio
PDF	probability density function
PEP	peak envelope power
QPSK	quadrature phase-shift keying
RBW	resolution bandwidth
RF	radio frequency
RFPM	RF (peak) power meter
RMS	root-mean-square
SA	spectrum analyzer
SG	signal generator
SMA	Stealth microwave amplifier
SNIR	signal-to-noise-plus-interference ratio
SNR	signal-to-noise ratio
TDMA	time-division multiple access
TW	time window (length of)
TWTA	traveling-wave tube amplifier
VEE	Virtual Engineering Environment
VNA	vector network analyzer
VSA	vector signal analyzer
VSG	vector signal generator
WLAN	wireless local-area network (LAN)

Summary

This work focuses on fixing measurement inaccuracies to which models and figures of merit are susceptible in two wireless communication environments: power amplifier and multipath. To emulate or rate the performance of these environments, models and figures of merit, respectively, are often used. The usefulness of a model depends on how accurately and efficiently it emulates its real-world counterpart. The usefulness of a figure of merit depends on how accurately it represents system behavior. Most discussions on the challenges and trade-offs faced in modeling nearly always focus on the complexity of the device or channel of interest and the resultant difficulty in describing it. Similarly, figures of merit are meant only to summarize the performance of the device or channel. At some point, either in generation or verification of a model or figure of merit, there is a dependence on measured data. Though the complexity and performance of the device or channel are challenges by themselves, there are other significant sources of distortion that must be minimized to avoid errors in the measured data. For this work, the unique distortion of power amplifier and multipath environments is considered, and then errors in measurement which would obscure these distortions are eliminated. Specifically, three measurement issues are addressed: 1) identifying measurement setup artifacts, 2) achieving consistent measurement results and 3) reducing variations in the environment. This work contributes to increasing the accuracy of microwave measurements used in the modeling of nonlinear high-power amplifiers and used in figures of merit for power amplifiers and multipath channels.

Ch. 1: Introduction

1.1. Motivation

Since the inception of digital wireless communications, there has been a growing demand for higher data rates and to allow an ever-increasing number of users in this mobile medium. To accommodate these demands, designs have simultaneously incorporated both wider bandwidths and bandwidth economization techniques. In many cases, like with orthogonal frequency division multiplexing, these have also led to more stringent timing and linearity requirements.

In digital wireless communications, there are two prominent signal distortion environments: power amplifiers and multipath channels. The power amplifier is a nonlinear time-invariant environment (NTI), and the multipath is a linear time-varying (LTV) environment. Both environments degrade the in-band and out-of-band metrics of a system. Both are sources of error vectors in band, which increases error vector magnitude (EVM) and of spectral regrowth out of band, which increases the adjacent channel power ratio (ACPR). For this dissertation, both distortion environments are analyzed.

In power amplifiers, a common design challenge is to achieve an optimum combination of linearity and efficiency, which trade off with each other. In transmission, devices have to contend with ever-increasing numbers of interferers and the challenge of frequency reuse inherent in cellular networks. Multipath effects, which are worst in urban areas, give rise to many copies of a signal that have been delayed in time and shifted in frequency. In addition to the usual path loss, these effects result in signal fading.

Augmenting the complexity that all the aforementioned items add to the design, compressed design schedules drive the demand for reliable and efficient models and meaningful figures of merit. Practical designs, which use these models, need a connection to real-world counterparts. This connection is made through measurement. Unreliable measurements give inaccurate models. Inaccurate models yield poor simulation results. A reliable measurement helps ensure a good real-world connection for the model. For this work, a power amplifier model was extracted in large part from measured two-tone data, and its usefulness depended on the accuracy of the measured data.

Figures of merit are also integral to design and evaluation of wireless systems and environments. A good figure of merit for measuring out-of-band distortion is the adjacent channel power ratio (ACPR), and a good figure of merit for in-band distortion is the error vector magnitude (EVM). Both the nonlinear time-invariant power amplifiers and the linear time-varying multipath environment will degrade the values of these figures of merit. In the power amplifier (PA) environment, the main measurement obstacle came from artifacts in the measurement equipment. In the multipath environment, artifacts arose from both the measurement equipment and time variances from the channel. To

enable direct comparison of any consecutive measurements, artifacts from both sources had to be reduced.

1.2. Research Goals

The goal of this research is not to develop new models for PA and multipath environments but rather, in these environments, to fix measurement distortions to which models and figures of merit are susceptible.

For the PA environment, a nonlinear PA behavioral model was extracted. A low peak-to-average two-tone signal, with its third-, fifth- and seventh-order intermodulation distortion (IMD3, IMD5 and IMD7, respectively) products, was used to map the nonlinearities inside and outside of a code-division multiple access (CDMA) band. The average power was swept to cover the full dynamic range of the PA. The tone spacing was swept to cover the range of memory effect delays. Through model extraction, this work allowed the prediction of the behavior of a power amplifier to a CDMA signal by using a two-tone signal. One issue was the sensitivity that the measurement setup needed when measuring the intermodulation distortion (IMD) products. Theoretically, a change of 1 dB in the fundamental tones results in a 3 dB change in the IMD3 for a Class A amplifier. Since some memory effects are on the order of 1 dB, such a change would obscure them. In fact, a typical measurement setup adds anomalies to the signal and measured results, effectively obscuring these memory effects. The resulting corrupted data hinder the accuracy of the extracted model.

For the multipath environment, EVMs of various orthogonal frequency-division multiplexing (OFDM) modulation types were compared to each other and directly to a

similar figure of merit (multisine error vector magnitude: MEVM) from a statistically-similar 55-tone multisine. This enhanced the view of the multipath environment and showed the practicality of substituting periodic signals for aperiodic ones in this type of measurement.

Whereas the two-tone measurements mapped a band of frequencies extending well into the out-of-band frequencies, the intentions for the multisine measurements were to compare signals in a certain band that were measured in a time frame within which the environment remained static. Multipath environments are usually synonymous with being linear and time varying. However, using careful techniques, a linear quasi-time-invariant multipath environment was obtained, which enabled the comparison of instances of EVM and MEVM that were calculated from sequentially-taken measurements. This setup also requires that other artifacts, inherent in the measurement equipment itself, do not spoil the measurement of the channel.

1.3. Dissertation Outline

The second chapter covers power amplifier modeling and introduces seven different behavioral models: Volterra, memoryless, quasi-memoryless, Wiener and Hammerstein, Wiener-Hammerstein and parallel Weiner. It uses the Volterra series to illustrate the need for high accuracy when measuring two-tone signals.

The third chapter again introduces the parallel Wiener model used to model memory effects in PAs. The chapter details two main sources of measurement inaccuracy and how they were eliminated. It shows the clean results that enabled the extraction of a

parallel Wiener behavioral model which is markedly improved over quasi-memoryless models when memory effects are present.

The fourth chapter discusses the multipath environment and the concept of time variance, illustrating how this adds uncertainty to propagating signals. It introduces three classic models used to describe narrowband multipath environments: Gauss, Rayleigh and Rice. The chapter then discusses the channel in wideband terms.

The fifth chapter covers accuracy in multipath measurements for both bursted and periodic signals. It discusses OFDM and its figure of merit, EVM. Then it discusses multisine generation and calculates a similar figure of merit, MEVM. Measurement issues are discussed next for both OFDM and multisine signals. Finally, results from three different measurement environments are discussed for OFDM and multisine: linear time-invariant, linear time-varying and linear quasi-time-invariant.

Chapter 2: Power Amplifier Models

2.1. Introduction

Power amplifier (PA) distortion is the first of two main signal distortion environments addressed in this work. Power amplifiers introduce nonlinearity into the signal. This presents some specific challenges to measurement and modeling, especially when operating at the high end of the dynamic range of the PA, near the 1-dB compression point of the PA (P_{1dB}), the output level where the gain of the PA decreases by 1 dB. The PA operates more linearly when backed off from this point. But the efficiency degrades significantly, and the energy that would normally be radiated as RF is instead dissipated as heat in the PA [1]. In the first case, for example, a back off of 3 dB for a Class B amplifier results in its efficiency dropping from a theoretical high of 78.5% to 55.5% [1]. Since the PA consumes most of the power in the transmitting device, this

reduced efficiency is often an unacceptable trade off. Linearization offers a way around this dilemma. Linearization methods, such as predistortion, feedback and feedforward, allow improvement in linearity while operating in the more efficient operating region of the PA.

In PA applications, a signal needs to be transmitted at a specified power level. As a result, the options are whether to run a PA inefficiently (but linearly) or efficiently (but nonlinearly) at the specified output power level. The first case requires the PA to be physically larger than the second case. Due to the low efficiency of the first PA, it will consume a significant portion of the total energy to achieve this goal. In the second case, the PA is physically smaller and operates more efficiently, which allows it to consume less energy. The trade off for higher efficiency is the added nonlinearities from the PA. However, with linearization, the aim is to gain back some level of the linearity while still operating in the high efficiency region of the PA.

Another challenge with linearization is the presence of memory effects in a PA. The heating of a PA when amplifying a signal will often change its characteristics. When the next signal arrives, these changes distort it differently than the previous signal. This limits the effectiveness of linearization techniques that rely on memoryless behavior. Models that take memory effects into account can be used to gauge the effectiveness of these linearization methods when memory effects are present.

2.2. Types of Models

In general, there are three ways to model PAs [2], [3]. The first is the physics-based model. This model includes information taken from the dimensions and physics of

the device. The second is a circuit-based model, which uses electrical circuit elements and circuit theory. The circuit-based model is most commonly used when characterizing solid-state amplifiers [4], [5]. These two models easily become too complex and thus inefficient when modeling systems. The third is the black-box-based, or behavioral-based, model. This model comes from the input-output relationship of a system and commonly uses linear and nonlinear stages to imitate the input-output relationship of the power amplifier for a subset of signals [4]. The resulting model is computationally efficient and can be represented with relatively simple mathematical expressions.

2.3. Types of Behavioral Models

For this work, there were three types of power amplifiers considered: memoryless nonlinear systems, quasi-memoryless nonlinear systems and nonlinear systems with memory [2]. These PAs are represented by various types of nonlinear behavioral models. This section introduces seven nonlinear behavioral models that are useful in emulating the behavior of PAs. It starts with the Volterra model and then covers six black-box models: memoryless, quasi-memoryless, Wiener, Hammerstein, Wiener-Hammerstein, and parallel Wiener. Other models are briefly mentioned. This chapter summarizes the model extraction method used for the parallel Wiener model and illustrates the need for accurate measurement data for the PA models.

2.3.1. Volterra Model

The Volterra PA model is a polynomial model and is represented by the Volterra series. The Volterra series is closely joined with the Taylor series [6]. As such, they have

similar primary constraints. The Taylor series is constrained to representing weak nonlinearities, since the series require the input to be constrained to a small deviation about a fixed (bias) point. Strong nonlinearities result in large deviations, which go beyond the capabilities of the Taylor series. Volterra shares this constraint to weak nonlinearities.

Another issue with Volterra is its complexity. Since the Volterra series quickly becomes extremely complex and unmanageable beyond the third order, it necessitates truncation. Unlike the Taylor series, Volterra series has a memory capability since it tracks the phase information of the signal and of its harmonic and intermodulation products, thus giving it many more terms to represent.

Since the Volterra series builds upon the Taylor series, it helps to start with Taylor. The equations for this are taken from [5]. The Taylor series describes the output response (i) to the minor deviations of a small signal (v) around a relatively large bias point (V_0). For the series itself, the bias point will be subtracted out

$$i = f\left(V_0 + v\right) - f\left(V_0\right), \tag{2.1}$$

which reduces it to the deviation around the bias point:

$$i = \frac{d}{dV} f\left(V\right)\Big|_{V=V_0} \cdot v + \frac{1}{2}\frac{d^2}{dV^2} f\left(V\right)\Big|_{V=V_0} \cdot v^2 + \frac{1}{6}\frac{d^3}{dV^3} f\left(V\right)\Big|_{V=V_0} \cdot v^3 + \cdots \tag{2.2}$$

Simplifying, by representing the derivatives as separate variables, results in

$$i = g_1 \cdot v + g_2 \cdot v^2 + g_3 \cdot v^3 + \cdots \tag{2.3}$$

where $g_k = \frac{1}{k!}\frac{d^k}{dV^k} f(V)\Big|_{V=V_0}$.

For the Taylor series above, the small-signal voltage, *v*, was used as the input signal and the small-signal current, *i*, as the output signal. Using a general time-domain input signal of s and a general time-domain output signal of w, the time-domain Volterra series, up to the third order, can be represented as [5]

$$\begin{aligned} w(t) &= \int_{-\infty}^{\infty} h_1(\tau_1) s(t-\tau_1) d\tau_1 + \int_{-\infty}^{\infty}\int_{-\infty}^{\infty} h_2(\tau_1,\tau_2) s(t-\tau_1) s(t-\tau_2) d\tau_1 d\tau_2 + \cdots \\ &\cdots \int_{-\infty}^{\infty}\int_{-\infty}^{\infty}\int_{-\infty}^{\infty} h_3(\tau_1,\tau_2,\tau_3) s(t-\tau_1) s(t-\tau_2) s(t-\tau_3) d\tau_1 d\tau_2 d\tau_3 + \cdots \end{aligned} \tag{2.4}$$

where s is the input signal delayed by time τ_k, and h—which describes the time-domain impulse response for a nonlinear channel—is the Volterra kernel in the time domain, defined mathematically as

$$\begin{aligned} h_n(\tau_1,\tau_2,\ldots,\tau_n) &= \frac{1}{(2\pi)^n} \int_{-\infty}^{\infty}\int_{-\infty}^{\infty}\cdots\int_{-\infty}^{\infty} H_n(\omega_{q1},\omega_{q2},\ldots,\omega_{qn}) \\ &\cdot \exp[j(\omega_{q1}\tau_1 + \omega_{q2}\tau_2 + \cdots + \omega_{qn}\tau_n)] \cdot d\omega_{q1} d\omega_{q2} \ldots d\omega_{qn} . \end{aligned} \tag{2.5}$$

The delays in time (τ_k) are embedded in the input signal but not in the impulse response, which indicates that this is a time-invariant system. Thus, Volterra is an appropriate model for PAs since they are nonlinear and time invariant.

Each of the integrals in (2.4), can be represented by an n^{th} order Volterra operator

$$I_n[s(t)] = \int_{-\infty}^{\infty} \cdots \int_{-\infty}^{\infty} h_n(\tau_1, \ldots, \tau_n) s(t-\tau_1) \cdots s(t-\tau_n) d\tau_1 \cdots d\tau_n \ . \tag{2.6}$$

This then can be represented as a schematic of the Volterra model, as shown in Figure 2.1.

For the frequency-domain representation of Volterra, [5] uses V to represent the input signal. For a periodic input [6], the frequency-domain Volterra series up to the third order is given as [5]

$$w(t) = \frac{1}{2} \sum_{q1=-Q}^{Q} V_{s,q1} H_1(\omega_{q1}) \exp[j(\omega_{q1})t] + \cdots$$

$$\cdots \frac{1}{4} \sum_{q1=-Q}^{Q} \sum_{q2=-Q}^{Q} V_{s,q1} V_{s,q2} H_2(\omega_{q1}, \omega_{q2}) \exp[j(\omega_{q1} + \omega_{q2})t] + \cdots \tag{2.7}$$

$$\cdots \frac{1}{8} \sum_{q1=-Q}^{Q} \sum_{q2=-Q}^{Q} \sum_{q3=-Q}^{Q} V_{s,q1} V_{s,q2} V_{s,q3} H_3(\omega_{q1}, \omega_{q2}, \omega_{q3}) \exp[j(\omega_{q1} + \omega_{q2} + \omega_{q3})t] + \cdots$$

where H is the Volterra kernel in the frequency domain:

$$H_n(\omega_{q1}, \ldots, \omega_{qn}) = \int_{-\infty}^{\infty} \cdots \int_{-\infty}^{\infty} h_n(\tau_1, \ldots, \tau_n) \exp[-j(\omega_{q1}\tau_1 + \cdots + \omega_{qn}\tau_n)] d\tau_1 \cdots d\tau_n \ . \tag{2.8}$$

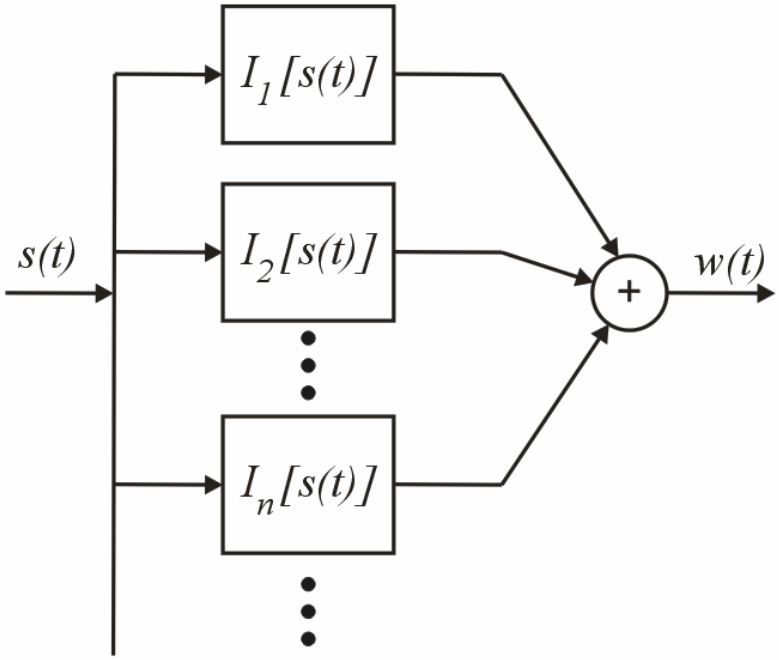

Figure 2.1: Schematic view of the Volterra model [6].

Through the Fourier transform, the time-domain representation of Volterra is equivalent to the frequency-domain representation. Thus, a frequency-domain modeling technique, such as the two-tone test in this work, can be made applicable to the time domain, where a digital signal is generated and observed.

In the Volterra model, the amplitude of a fundamental tone that fluctuates around its intended setting will result in much higher errors in the intermodulation and harmonic components. If the fundamental tones are set higher than intended, the IMD3, for example, will be measured as higher than if the fundamental tones were set correctly. If the fundamental tones are set lower than intended, the IMD3 will be read as lower than if the fundamental tones were set correctly. Furthermore, since the amplitude of the IMD3 have a cubic dependence on the amplitudes of the fundamental tones; the error in the

IMD3 also has a cubic dependence on the difference between the intended and actual levels of the fundamental tones.

This relation can be illustrated with a Taylor series—to which Volterra reduces when its phase information is eliminated—similar to that of (2.3) but with just voltages [1]:

$$v_o = a_1 v_i + a_2 v_i^{\,2} + a_3 v_i^{\,3} + \cdots \tag{2.9}$$

Next a two-tone representation of the input is made:

$$v_{in}(t) = A\left[\cos(\omega_1 t) + \cos(\omega_2 t)\right], \tag{2.10}$$

where A is the amplitude and ω_1 and ω_2 are the operating frequencies of the fundamental tones subject to $\omega_2 = \omega_1 + \Delta\omega$.

Up to the third order, this results in

$$v_o(t) = a_1 A\left[\cos(\omega_1 t) + \cos(\omega_2 t)\right] + a_3 A\left[\cos(\omega_1 t) + \cos(\omega_2 t)\right]^3 + \cdots \tag{2.11}$$

Expanding these terms and then focusing on the fundamental terms and the third-order intermodulation products, results in

$$\begin{aligned} v_o(t) = &\left(a_1 A + \frac{9 a_3 A^3}{4} \right)\left[\cos(\omega_1 t) + \cos(\omega_2 t)\right] + \cdots \\ &\cdots + \frac{3 a_3 A^3}{4}\left\{\cos\left[(2\omega_1 - \omega_2)t\right] + \cos\left[(2\omega_2 - \omega_1)t\right]\right\} + \cdots \end{aligned} \tag{2.12}$$

Expressing the coefficients of (2.12) in decibels and retaining only the dominant terms, produces

$$20\log_{10}\left(a_1 A+\frac{9a_3A^3}{4}\right)\cong 20\log_{10}\left(a_1 A\right)=20\log_{10}\left(a_1\right)+20\log_{10}\left(A\right)$$

for the fundamental term and

$$20\log_{10}\left(\frac{3a_3A^3}{4}\right)=20\log_{10}\left(\frac{3a_3}{4}\right)+60\log_{10}\left(A\right)$$

for the third-order intermodulation term. As can be seen on the right-hand side of these two expressions, a variation in A that produces 1 dB of variation at the fundamental tones will result in a 3 dB variation in the IMD3. As a corollary, an IMD3 on the order of 1 dB would require the amplitudes of the fundamental tones to be set with an error that is < 0.3 dB to avoid its being masked by cancellation or amplification.

Furthermore, it can be shown that 1 dB of variation in the fundamental tones would also result in 5 dB of variation in the IMD5 and 7 dB of variation in the IMD7. The parallel Wiener model extracted from these two-tone measurements used the IMD products up to the seventh order, which underscores the importance of reducing these errors that get magnified at other frequencies.

As shown in the above equations, the Taylor series illustrate that obtaining IMD3 depends in part on accurate amplitude settings for the fundamental tones. In this work, the goal was to ensure that the fundamental tones fluctuated no more than 0.1 dB over a frequency spacing of 10 kHz up to 5 MHz. The process by which this was done, and the

subsequent reduction in the measurement error vectors of the IMD, will be discussed further in Chapter 3.

2.3.2 Memoryless Model

In general, memoryless implies two things in a nonlinear system. First, the immediate output of a memoryless system depends only on the immediate input power envelope to that system and not on any past inputs. This means that the system characteristics are unchanged between inputs. Second, the system distorts the signal only in amplitude and not in phase [2]. This allows the power amplifier to be represented by a single amplitude-to-amplitude modulation (AM/AM) transfer function, as shown in Figure 2.2.

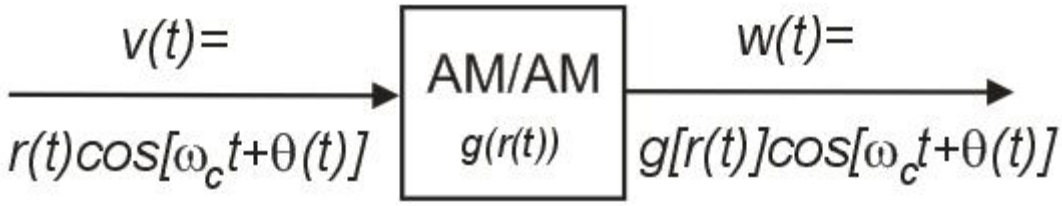

Figure 2.2: One-box memoryless model.

This behavioral model has limitations similar to the quasi-memoryless model, which contains both AM/AM and amplitude-to-phase modulation (AM/PM) effects. The PA block is represented by a narrowband AM/AM transfer function. Blachman provides a detailed analysis of the memoryless nonlinearity in [7]-[9].

Mathematically, the memoryless model can be described by the following complex functional input-output relationship [10]:

$$\bar{y}(t) = \overline{G}\left[\bar{x}(t)\right] . \tag{2.13}$$

where $\bar{x}(t)$ and $\bar{y}(t)$ are the instantaneous input and output, respectively, of the system and $\overline{G}$ is a function solely of the amplitude of $\bar{x}(t)$, as shown in Figure 2.2.

The memoryless model is a one-box model and is often represented by Taylor series [1]. The memoryless model represents AM/AM distortion only [2]. Furthermore, this model is mainly used to model weak nonlinearities at one bias level and at one operating frequency [1]. Thus, it is not a good candidate for wideband applications with multiple decibels of dynamic range as needed in this work, where the response of a 30 W Class AB laterally-diffused metal oxide semiconductor (LDMOS) PA module to a CDMA signal, which has a bandwidth of 1.25 MHz, needs to be emulated.

2.3.3. Quasi-Memoryless Model

There are two nonlinear behavioral models that are commonly called memoryless. The first is a one-box model and represents only AM/AM distortion characteristics and, strictly speaking, is properly called the memoryless model. The second is a two-box model that represents both AM/AM and AM/PM distortion characteristics and is properly called the quasi-memoryless model [2]. Often this quasi-memoryless model is simply called memoryless and is represented by a single box that includes both its AM/AM and AM/PM effects, as shown in [3]. For instance, in [10] the author labels a model that

describes both AM/AM and AM/PM distortion as being memoryless. However, a PA will often exhibit significant memory effects, even when its power is backed off from P_{1dB}, via its asymmetries and other fluctuations in IMD that are, as shown in the Volterra model, due to phase modulation. When the vectors of the IMD and fundamental frequencies add, the phase differences cause the resultant amplitude asymmetries and fluctuations. As a result, since AM/PM effects are essentially memory effects, it is best in this work involving PAs with memory effects to distinguish between memoryless and quasi-memoryless models.

The quasi-memoryless model does not show any substantial frequency-selective effects but rather demonstrates only AM/AM and AM/PM distortion behavior [10]. The quasi-memoryless nonlinear system does have some thermally-induced memory effects, which appear as IMD asymmetry [1], but these are about the same time length as the period of the RF carrier [2]. In this case, the PA block is represented by AM/AM and AM/PM distortion boxes. Figure 2.3 presents a schematic view of and analytical relations for this model.

The mathematical relationship in Figure 2.3 represents the AM/AM with $g[r(t)]$ and the AM/PM with $\phi[r(t)]$, where $r(t)$ is the input amplitude. Since the memory effects represented by this model are so short—on the order of the RF carrier—this relationship indicates that the AM/AM and AM/PM depend solely on the current input signal.

In general, AM/AM and AM/PM functions are obtained by scaling a single tone over a range of power or, extending to cover IMD, by scaling a two-tone signal over a range of power [11]. In a Class A amplifier, AM/PM becomes a concern only as it nears the P_{1dB} of the PA [1]. However, well below the compression region, Class AB shows

several degrees of AM/PM effects for every 1 dB step in the output power of the PA [1]. Single-tone tests are typically used to find AM/PM effects near compression. However, with these effects showing up well below compression in PAs that are something other than Class A, there is a motivation for using two-tone measurements instead.

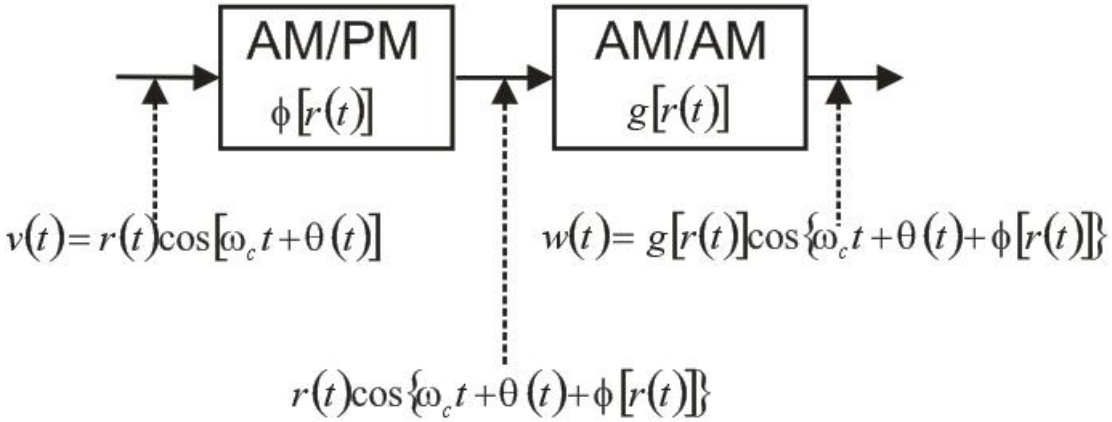

Figure 2.3: Cascade quasi-memoryless nonlinear model [2].

An advantage in constructing the memoryless and quasi-memoryless models is that they can be extracted from vector network analyzer (VNA) measurements. The VNA gives higher measurement accuracy than other appropriate instruments, such as a spectrum analyzer (SA) or a power meter. However, the VNA can only make single-tone measurements. Just as the measurement is narrowband, so the model tends to work well only when representing narrowband signals. As such, the memoryless and quasi-memoryless models run into limitations in describing nonlinearities with memory effects, which happen increasingly as the bandwidth and the output power in a power amplifier increase.

2.3.4. Wiener and Hammerstein Models

The Wiener model is a two-box model that was developed as one solution to the overwhelming complexity of the Volterra model, to the weak-nonlinearity limitation of the Volterra model and to the difficulty in measuring Volterra kernels. It also is an attempt to represent some of the memory effects displayed by nonlinear systems. The following paragraphs discuss some issues with the Volterra model.

Volterra is difficult to implement in a working application. First, it is formidable to measure the Volterra kernels of a system due to how deeply they intermix. To get these kernels, the input of each Volterra operator would somehow have to be isolated from the overall system. This is a practical impossibility. Second, Volterra series easily diverges. The series converges only for small signal amplitudes [6].

Since the Volterra operators are indistinguishable from each other in measurement for a practical, infinite-order system and have convergence issues for large signal amplitudes, approximations to Volterra that get around these issues must be used [6]. The Wiener model gets around the limited convergence inherent in Volterra by using orthogonal functions. This works for functions in a similar fashion to how orthogonality works for vectors. This also gets around the inability to measure Volterra functionals since these functionals are orthogonal and not all intermixed. The trade off for the increased range allowed by the orthogonal functionals is some sacrifice in accuracy.

One of the loosened standards relates to how the error is calculated. Volterra requires that the derivatives of error approach zero. For Wiener, only “the area under the square of the error [need] approach zero” [6]. This allows its solutions to converge over a larger range.

With Volterra systems of infinite order, the operators intermix such that they are nearly impossible to separate from each other. With Wiener, the operators are functionals that are orthogonal and of finite order. An orthogonal series only needs to converge in the mean. This is a looser convergence criterion than for Volterra—where the series itself must converge—and allows Wiener to represent a larger collection of nonlinear systems than Volterra.

Figure 2.4 gives the cascade-connection structure for the Wiener model. Wiener combines the two boxes of the quasi-memoryless model into its second box, which gives its static nonlinearity relation, and precedes this with a linear filter box, which encompasses the memory effects. These are shown in Figure 2.4. As indicated on the figure, the first box is named after Wiener. This model is the basis for the parallel Wiener model presented in a later section.

The Hammerstein model, shown in Figure 2.5, is also a two-box model and is similar to the Wiener model. This model switches the places of the two boxes presented by Wiener so that the memoryless nonlinear static function precedes the linear dynamic filter. The second box is named after Hammerstein.

Both the Wiener and Hammerstein models allow the representation of some memory effects in nonlinear systems. Due to their small-signal frequency response, they are able to be measured using a VNA. By having just one linear filter, they are also easier to extract than those of a three-box model, which is covered in the next section. In the case of the Wiener model, its structure also parallels the action of some amplifiers, like the traveling-wave tube amplifier (TWTA) [3].

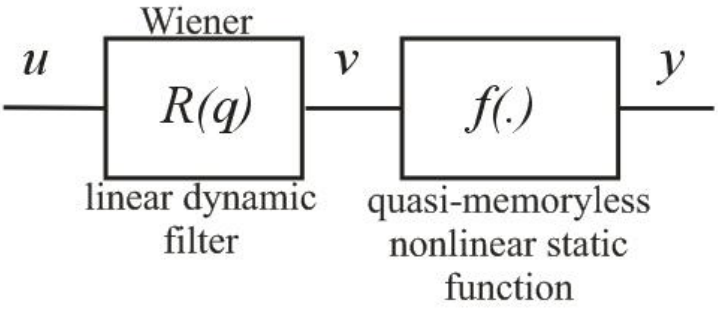

Figure 2.4: Wiener structure, shown in a cascade connection [12].

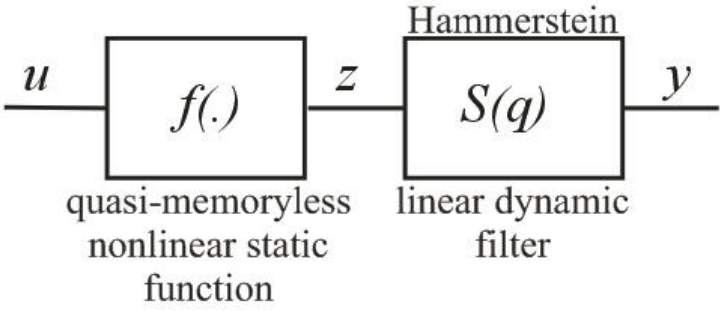

Figure 2.5: Hammerstein structure in a cascade connection [12].

Though both Wiener and Hammerstein models have advantages over Volterra when extracting a model, they still have issues of their own. They both have convergence challenges, which have been addressed in multiple works [13]-[25]. Separating the linear response from the nonlinear response and the complexity needed in each of these responses often presents difficulties [13], [17], [19], [23], [26]-[28].

However, it is not the extraction issues that are the limitation for this work. In the end, the models are not able to capture the level of complexity presented by the wide-band, high power PAs used here. The Wiener and Hammerstein models have difficulty capturing the AM/AM and AM/PM curves that are due to envelope frequencies. These AM/AM and AM/PM curves have long time-constant memory effects that are not adequately represented by the single linear system of either model. Furthermore, they

lack the level of frequency dependence needed in this work for modeling wideband signals.

2.3.5. Wiener-Hammerstein Model

The Wiener-Hammerstein model is a three-box behavioral model [12], [29], which is shown schematically in Figure 2.6. This model combines the Wiener and the Hammerstein (two-box) models into one three-box model and is more effective than either of these two-box models at fitting the model to data curves [3], which leads to a model that better represents the behavior of the PA. Like the Wiener and Hammerstein models, this model describes PA behavior using nonlinear static and linear dynamic functions. In this case, the resulting Wiener-Hammerstein model sandwiches the nonlinear, quasi-memoryless static function between two linear dynamic functions.

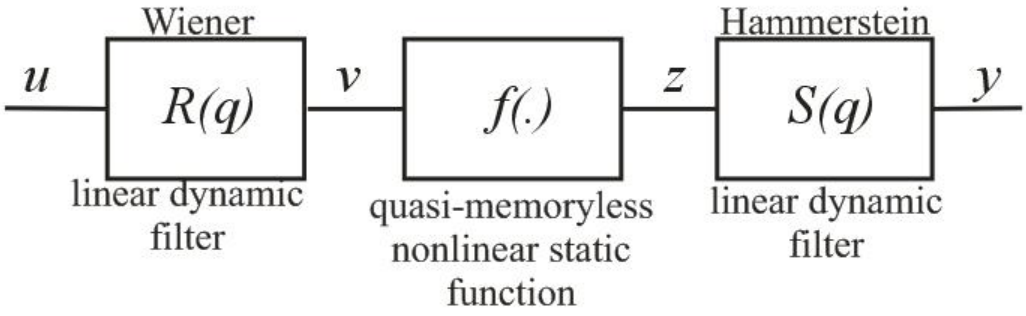

Figure 2.6: Wiener-Hammerstein structure in a cascade connection [12].

The center box in Figure 2.6 introduces the AM/AM and AM/PM (i.e., the components of the quasi-memoryless model) behavior of the device at the center frequency. It is static since it does not take into account the deviations of the distortion of the device from these AM/AM and AM/PM curves when operating at a wide bandwidth. This is where the two cascaded linear filters contribute. They add frequency-dependent

distortion effects. Since they are normalized to the center frequency, it allows them to represent only how the distortion changes the AM/AM and AM/PM over the band in which the model was extracted [29]. Since memory effects show frequency dependence, this allows the two filters to account for memory effects.

For the Wiener-Hammerstein model, the resolution of the two dynamic systems while extracting often leads to convergence issues. As stated previously, difficulty in distinguishing kernels from measurements is one of the motivations for using a model other than Volterra. Some techniques for deciphering the two dynamic systems of the Wiener-Hammerstein model are covered in [12], [30], [31].

Classically, the linear filters of the Wiener-Hammerstein model are extracted using a single-tone measurement technique [29]. Though this tone is swept over the passband and over the range of power of the device, this still only allows the model to acquire short-term memory effects. When short-term memory effects—such as those excited by a narrowband signal—are the only memory effects of concern, this type of extraction approach for the Wiener-Hammerstein models may be used. If a wider-band signal is used when extracting the model with this method, then the extraction error increases as the bandwidth increases [29].

Since AM/AM and AM/PM effects in the nonlinear model are static, and since the linear filters are normalized to the operating, or center [29], frequency, the Wiener, Hammerstein and the Wiener-Hammerstein models are not functions of the operating frequency [2]. Also, when more than one tone exists, these tones are going to have unique magnitudes and phases that result in unique interactions for each time instance, a level of dynamics which this model, when extracted using a single tone, cannot describe [2], [4].

Though the Wiener-Hammerstein model is often extracted from single-tone measurements, a method is given in [4] for extracting it from two-tone measurements, and a method is given in [31] for extracting it from a random-phase multisine excitation. Since, in the two-tone approach, the SA measures the intermodulation products with this method, the technique will allow the capture of the reaction of the PA to the modulation envelope. For the approach that uses a random-phase multisine to excite the PA, they were able to decipher nonlinear effects appearing in the passband by omitting some sine wave components in the passband.

These last two techniques, plus one found in [32], are some examples of ways to extend the capabilities of the Wiener-Hammerstein model from narrowband PA behavior to wideband PA behavior.

One of the limitations of this model is that its one branch has to represent all the linear and nonlinear effects of the PA. When the PA is in compression, the nonlinear components are readily distinguished from the linear components. However, the level of error in predicting memory effects increases as the PA backs off from P_{1dB}. This is due to the increasing dominance of the in-band signal over the in- and out-of-band nonlinear components. That is, when the PA operation backs off from P_{1dB}, the linear components dominate. In addition, the nonlinear components, due to their stochastic nature, can be falsely taken for noise when the PA is backed off from P_{1dB}. A recent approach to dealing with this limitation is given in [31], where some of the sine wave components in the random-phase multisine were omitted. This allowed the nonlinear components in the passband to be measured without interference from the dominant linear signal. The downside of this method is the cost of the large-signal network analyzer (LSNA) needed

to make the measurements. This work preceded the method in [31] and used the parallel Wiener model to represent nonlinear components in the presence of dominant linear components when the PA is backed off from P_{1dB}.

2.3.6. Parallel Wiener Model

The previous models dealt mostly with memoryless nonlinearities and nonlinearities with short-term memory effects, which limit the application of the models to narrowband signals. This section covers the parallel Wiener model, based off a model originally developed by Schetzen [33]. The parallel Wiener model expands the capability of the behavioral model to long-term memory effects, which allows it to model wideband signals. Asymmetries between the upper and lower IMD and variations in the IMD with the frequency spacing of a two-tone test are caused by the long-term memory effects of the PA.

It is called a parallel Wiener model since it is composed of several Wiener systems of the type presented in Section 2.3.4 and in [6] attached in parallel [33], as shown in Figure 2.7. This model is extracted from the IMD taken from two-tone measurements that have been varied in power and in frequency spacing. Magnitude variations and asymmetry in the IMD, obtained during a two-tone measurement, reveal short- and long-term memory effects, which then can be incorporated into this model.

The first branch in Figure 2.7 contains a linear time-invariant (LTI) system in cascade with a nonlinear (static) quasi-memoryless AM/AM and AM/PM model extracted from single-tone measurements. Next, the error between the model and the two-tone measured data is calculated. To reduce this error a parallel branch, which this time

includes a combination of a long-delay linear time-invariant (LTI) system and a nonlinear quasi-memoryless system in cascade, is added. The AM/AM and AM/PM curves for this branch are derived from the complex envelope transfer function that is derived from two-tone measurements, which gives the intrinsic characteristics of the device, and the probability density function (PDF) of a CDMA signal [2]. The PDF of a CDMA signal readjusts the weighting of the IMD of the two-tone signal so that the model represents the behavior of the PA when excited by a CDMA signal, which has a higher PAPR than the two-tone signal. Additional branches, also composed of long-delay LTI systems in cascade with nonlinear quasi-memoryless systems, are added to further reduce the error between the model and the measured data. These additional branches allow the representation of dynamic AM/AM and AM/PM, which are due to memory effects. Each branch added in parallel reduces the mean square error between the model and measured data. The acceptable error level is a function of the needs of the modeler, and branches are added until the desired level is reached [2]. If the desired error level is set too low, then the output noise dominates the estimation of additional paths once the optimum number of branches is reached [34]. The linear time-invariant branch allows a long delay to be added to account for the memory effects with long time constants [2].

In general, the black-box models mentioned previously suffer in accuracy as the PA is backed off from P_{1dB}. This is because the linear components of the output signal become increasingly dominant relative to the nonlinear components the further the PA is backed off from P_{1dB}. Since the parallel Wiener model represents the dominant linear component with its small AM/AM and AM/PM static nonlinear components in its first branch, this leaves its subsequent branches to represent the memory effects which, when

the PA is in back off, are much less dominant than the linear component and easily mistaken for noise due to their stochastic nature [31], [35].

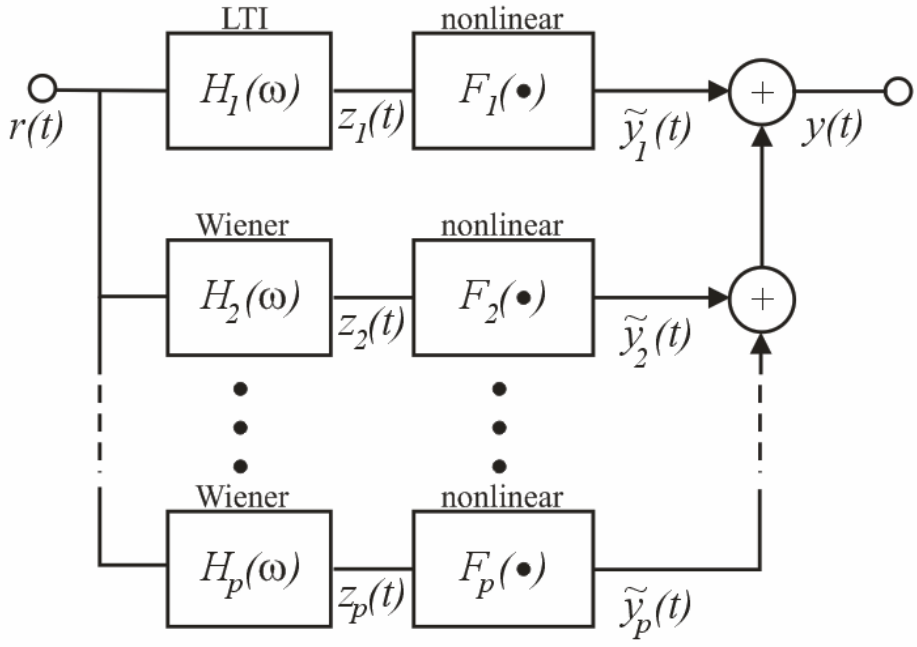

Figure 2.7: Parallel Wiener model [2].

This extraction method produces a model that represents both power dependence and envelope-frequency dependence for a wideband signal. Power dependence is well represented as memoryless or quasi-memoryless. Envelope-frequency dependence, on the other hand, implies a dependence on signal inputs prior to the current time, which is the memory of the system [2]. Memory effects can be seen as a type of hysteresis, where there is some lingering effect from past inputs, in the input/output relationship. For a two-tone signal, the general equation for output of a PA with memory effects is [2]

$$w(t) = \left|F(r,\omega_m)\right| \cos\left[\omega_c t + \theta(t) + \angle F(r,\omega_m)\right] . \tag{2.14}$$

The function $F(r,\omega_m)$ shows the dependence of the output on both the input amplitude (r) and frequency spacing (ω_m) of a two-tone signal.

Admittedly, this model has more complexity than others presented as estimations of Volterra. However, this complexity enhances its ability to predict nonlinear phenomena arising from memory effects. For a 45 W Class B PA, this model improved ACPR prediction over the quasi-memoryless model, derived from single-tone measurements, by 4 dB near the carrier band [2]. This same amplifier exhibits variations in IMD with respect to frequency spacing of up to 10 dB. However, as data in the next chapter show, it is common for amplifiers to have fluctuations in the IMD as low as 1 dB, which would indicate a need for precise measurements of the IMD products.

A figure of merit, called the memory effects ratio (MER), is calculated to illustrate the level of contribution made by memory effects to the nonlinear components in the output signal from a PA [36]. MER ($\|y_2\|_2$) calculates the two-norm of the output of a PA with memory (y) less the output of a quasi-memoryless PA (y_1). Mathematically, this is given as

$$MER = \|y_2\|_2 = \|y - y_1\|_2 \ . \tag{2.15}$$

PAs with higher memory effects result in a larger MER than PAs with lower memory effects. A higher MER indicates lower linearity improvement in a PA due to quasi-memoryless predistortion. This indicates a decreased improvement in ACPR when quasi-memoryless predistortion is used for linearization. The ACPR improvement may be high in the backed off regions of a PA (up to 10-20 dB for MERs of 0.15-0.35 in [36]), but, in [36], they were shown to be as low as 1-2.5 dB, when nearing compression. This

motivates the need to eliminate errors in the measurements that can lead to ≥1 dB of error in the IMD. The MER also helps to quantify the need for a model, like the parallel Wiener model, that is able to accurately represent memory effects within a PA both when it is backed off and when it is in compression.

Besides its added complexity, another disadvantage of the parallel Wiener model is that, for this method, it requires several hours to acquire all the two-tone data from which it is extracted. This is for two reasons. The first is that the tones must be swept over a range of power and frequency spacing. The second is that the need for a high level of accuracy in the measurements necessitates a longer overall measurement time. These issues are detailed in Chapter 3.

2.3.7. Other Behavioral Models

Thus far, three classes of models have been introduced. The first class is the Volterra model. The Volterra model tracks the amplitudes and phases of all harmonic components and intermodulation distortion products. The second class is the memoryless and quasi-memoryless models. These models are good to use when a PA is narrowband has little to no memory. The third class is the linear-nonlinear black-box models: Wiener, Hammerstein, Wiener-Hammerstein and parallel Wiener. These models are able to represent memory effects in PAs.

A fourth class of models is the memory polynomial models. The memory polynomial model is considered an abridged version of the Volterra series [37], and, just as the linear-nonlinear models, it has many applications and forms. Whereas the Wiener-Hammerstein model is a continuous-time model, the memory polynomial is a discrete-

time model. A typical memory polynomial uses delay taps followed by static nonlinear functions [2]. Since memory polynomial models are a class by themselves—and each type of model within this class could fill its own section—they are only briefly mentioned here for completeness. Some examples of memory polynomial models are given in [2], [37], [38].

2.4. Conclusions

This chapter covered the first source of distortion in wireless systems addressed in this dissertation: nonlinear time-invariant distortion in PAs. PAs exhibit nonlinear behavior when operated at their optimum efficiency. This behavior has prompted much work on linearization techniques to improve the linearity of the output of the PA while maintaining its efficiency.

Of the PA models, Volterra is the most exhaustive in tracking nonlinear components. It follows all the amplitude and phase components of all the nonlinearities from the PA. Using the power series to represent a Class A amplifier, it was shown that a 1 dB fluctuation in the fundamental term results in a 3 dB fluctuation in the IMD3. It follows from this that a 1 dB fluctuation in the fundamental tones will also result in a 5 dB fluctuation in the IMD5 and a 7 dB fluctuation in the IMD7. As will be shown in Chapter 3, many memory effects—manifested by IMD3 asymmetries and deviations from the typical 3 dB slope for every 1 dB of increased power—are on the order of 1-2 dB. Thus, it is important to maximize the accuracy of the power setting for the fundamental tones at each frequency separation.

In this work, a parallel Wiener model was extracted from two-tone data, which was weighted using the PDF of a CDMA signal. Though more complex than similar black-box models (Wiener, Hammerstein and Wiener-Hammerstein models), the parallel Wiener model allowed the memory effects showing up in the IMD products, which are often 30-40 dB below the fundamental tones, to be represented by separate Wiener branches. These branches are in parallel with the main branch that represented the short-term memory effects and the quasi-memoryless behavior of the PA. This allowed more accurate modeling of the memory behavior of the PA than the other black-box models and allowed the effectiveness of quasi-memoryless predistortion on a PA with memory to be quantified through the calculation of the MER.

In order to quantify the effectiveness of quasi-memoryless predistortion on a PA with memory, it was critical to have measurements that would capture IMD fluctuations and asymmetries on the order of 1 dB. The model had to capture both these fine variations and be able to represent the long time delays that accompany these.

Chapter 3: Two-Tone Measurement Accuracy

3.1. Introduction

As mentioned in Chapter 2, the purpose of this work is to extract a model that accounts for long-term memory effects in power amplifiers. The intention is that this model could then be used to improve predistortion, which has the advantages of being stable and wideband [1]. Despite these advantages, predistortion often has the disadvantage of being an open-loop linearization method that requires an accurate PA model for prediction. The accuracy of the parallel Wiener model used in this work depends on the accuracy of the measurements of the IMD3, IMD5 and IMD7 of the PA module.

A PA nonlinearly distorts signals that pass through it. The purpose of predistortion is to reduce these nonlinear components by distorting the signal in an

opposite manner to that of the PA such that it cancels the nonlinear components added by the PA. In this work, accurately measured data allowed the extraction of a parallel Wiener model. This precise model improved the prediction of spectral regrowth by up to 4 dB over the quasi-memoryless model for a 45 W Class B power amplifier [39].

3.2. Memory Effects

The parallel Wiener model developed in [39] has the potential to extend the capabilities of predistortion. In the past, predistortion was most commonly directed at correcting only AM/PM [1]. The parallel Wiener model is one solution to the challenge of correcting distortion due to AM/AM, AM/PM and memory effects with long time constants. This inclusion of memory effects improves the prediction of the behavior of a PA when excited by a CDMA signal. Measurements of the ACPR of a PA with a CDMA signal compare well with that predicted by the parallel Wiener model [39].

In this work, memory effects were the main focus of the modeling. The high-power PA modules measured had nonlinear components with memory effects. Memory effects create asymmetry between upper and lower IMD levels, and the asymmetry varies with power level and tone spacing. The unique memory characteristics in these high-power PA modules limit the ability to linearize them using traditional quasi-memoryless predistortion linearization techniques.

In [39], it was demonstrated that these memory effects would show similar limitations for a given nonlinear system whether it has CDMA or a range of two-tone signals passing through it. In [40], a model was extracted based on the IMD, and it agreed well with the ACPR measurements of a CDMA signal. The input power level and tone

spacing of the two-tone signal were varied to extract the intrinsic characteristics the PA module.

A key component to extracting an accurate model for the PA is first to obtain measured data that accurately represent the behavior of the PA itself. However, the measurement setup often adds unwanted effects into the measured data and thus obscures the behavior of the PA. An example in this test setup was a frequency-dependent variation in the power level of the fundamental tones being applied to the DUT. This type of variation in the fundamental tones outside of the PA is amplified in the IMD of the PA, as predicted in Chapter 2. For the 30 W two-stage Class AB LDMOS PA module presented in this work, memory effects produced asymmetry between the upper and lower IMD3 that ranged from <0.5 dB to >10 dB. Such asymmetry is illustrated in Figure 3.1.

In Figure 2 of [41], it shows asymmetry in IMD3 magnitude for an LDMOS PA that ranges from 0 dB up to just over 2 dB and IMD3 phase asymmetry ranging from 0° up to 35°. Unwanted variations in the fundamental tones change the asymmetry properties of the data, which changes the perceived memory characteristics of the PA. This effect will be illustrated in this chapter.

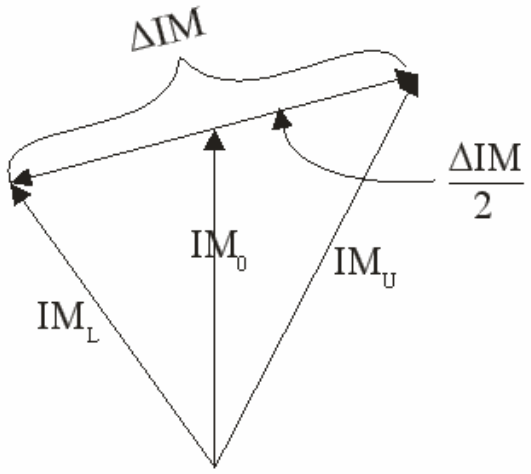

Figure 3.1: Graph illustrating IMD asymmetry [41]. ΔIM = total error, which is the difference between IM_u and IM_L.

Theoretically, a change of 1 dB in the fundamental tones will result in a 3 dB change in the IMD3, a 5 dB change in IMD5 and a 7 dB change in IMD7 for a Class A amplifier. For this work, the LDMOS PAs were operating as Class AB. Class AB amplifiers often portray less predictable levels of fluctuation in their IMD products and so the fluctuation predicted by Class A operation can only be used as a rough estimation for these products. A comparison of fundamental tones with varying levels to its IMD products is given in Figures 3.2 and 3.3 for a practically memoryless 10 W LDMOS Class AB amplifier. Figure 3.2 plots the fundamental tones and IMD products over a range of power and tone spacing. Figure 3.3 focuses on the points at the highest power level and plots the fundamental tones and the IMD products on the same scale. The variations in the fundamental tones are not as apparent in Figure 3.3(a) as they were in Figure 3.2(a). However, by examining both Figures 3.2 and 3.3, it can be seen that the variations in IMD3, IMD5 and IMD7 track those in the fundamental and that the fundamental variations are magnified in the IMD3, IMD5 and IMD7. The difference

between the highest and lowest points is 0.4 dB for the fundamental tones, 1.6 dB for the IMD3, 1.8 dB for the IMD5 and 2.2 dB for the IMD7. Normalizing the fundamental tones to 1 dB would give the IMD results shown in Table 3.1. The table also shows what the values would be theoretically if the amplifier were operated as a Class A. It is obvious from Table 3.1 that, though the IMD products do reflect and magnify the variation of the fundamental tones, the amount of variation is not easily predictable for Class AB amplifiers. Nevertheless, it appears that there will be at least 3-4 dB of variation in the IMD products for every 1 dB of variation in the fundamental tones.

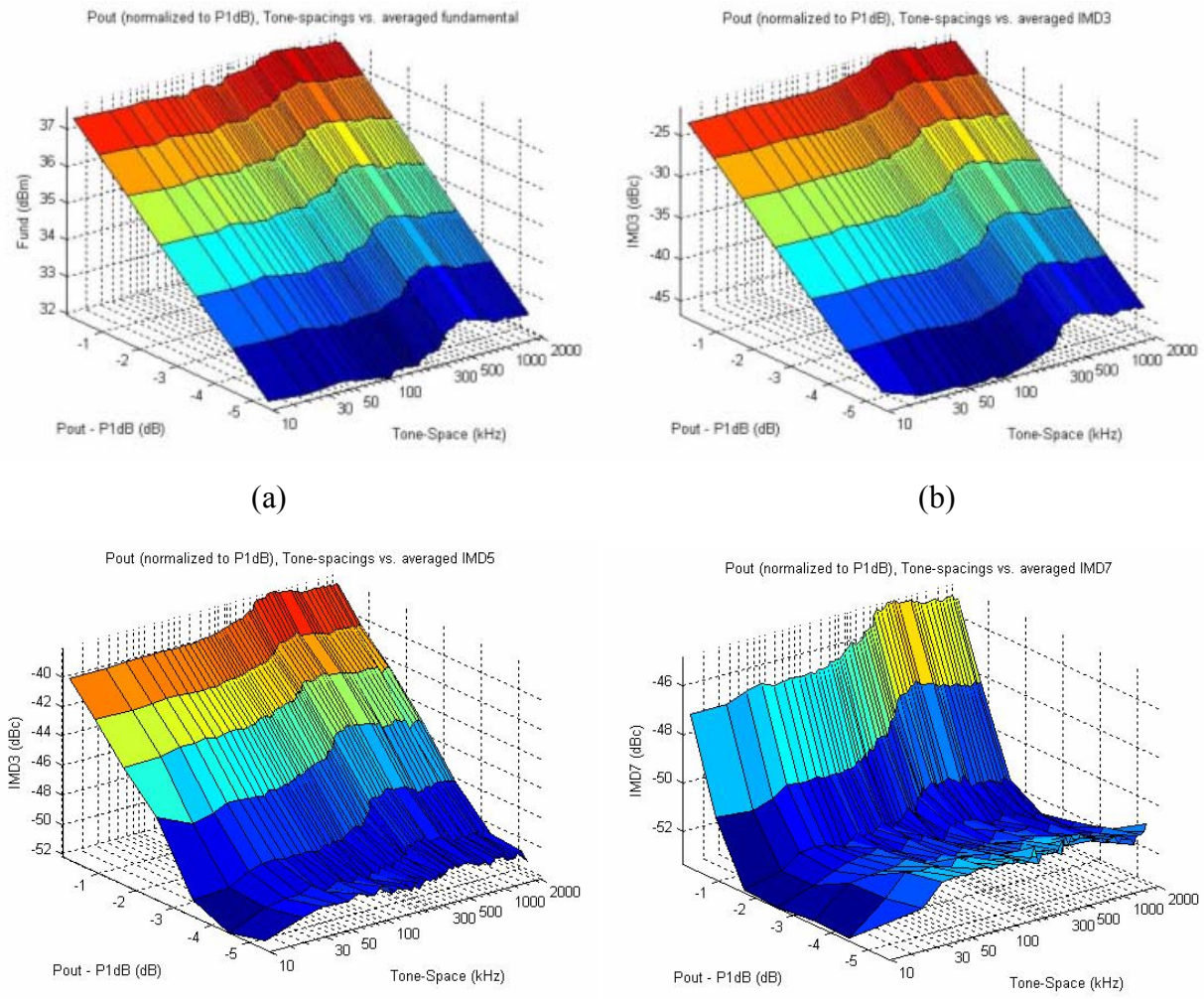

Figure 3.2: A 10 W, practically memoryless, Class AB LDMOS power amplifier. This shows the IMD3, IMD5 and IMD7 variations reflecting that of the fundamental tones.

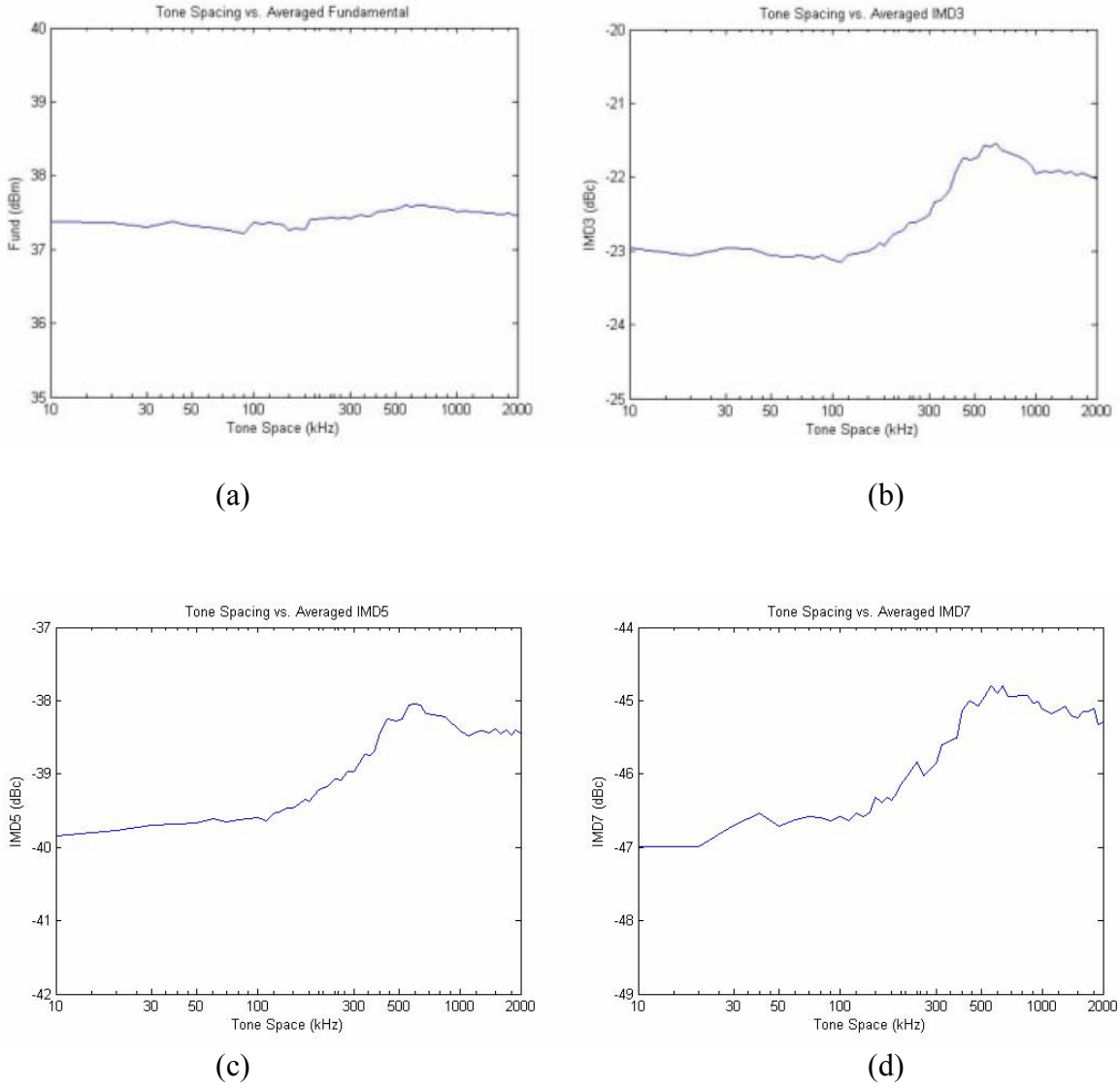

Figure 3.3: Graphs of the highest power level from Figure 3.2.

Table 3.1: Variations in fundamental tones and the resulting behavior of their IMD products at P_{1dB}.

Amplifier	ΔFundamental (dB)	ΔIMD3 (dB)	ΔIMD5 (dB)	ΔIMD7 (dB)
Class A (Theory)	1	3	5	7
10 W Class AB	1	4	4.5	5.5

3.3. Two-Tone Measurement Setup

The focus in this chapter is the measurement technique used to achieve a high level of resolution when measuring intermodulation distortion products. In order to do this, several effects from the measurement setup itself needed to be eliminated or corrected. The measurement setup that was used is shown in Figure 3.4. The arbitrary waveform generation (ARB) function in the Agilent E4432B vector signal generator (VSG) produced the two fundamental tone components. The reference signal of the signal generator is attached to the Agilent E4404B spectrum analyzer (SA), which measured the amplitudes of the fundamental tones and IMD products up to the seventh order in the upper and lower sidebands. The Agilent 34401A digital multimeter (DMM) measured the drain voltage and current. The Boonton 4531 RF power meter (RFPM) measured average power and, to protect the device under test (DUT), was used to prevent P_{IN} from surging. The instrument control program was Agilent VEE Pro 6.0.

Also shown in Figure 3.4 are several attenuators, cables and a power divider, which are all wideband. Besides these, the VSG, the preamp and the isolators all can affect the signal amplitude over the 5 MHz frequency band of the fundamental tones.

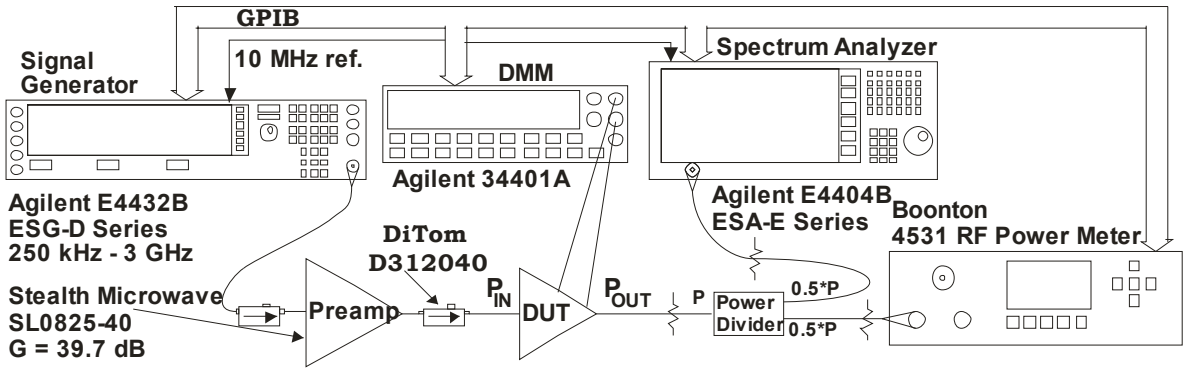

Figure 3.4: Two-tone measurement setup for high-power amplifiers [42].

3.4. Measurement Setup Artifacts

It is essential that the fundamental tones and IMD are as free as possible from measurement error over the bands in which they operate. For the fundamental tones, an accurate input power to the DUT over its 5 MHz bandwidth had to be ensured. For the IMD, acceptable linearity in the VSG and preamp had to be ensured. For all tones and products, values measured by the spectrum analyzer had to be made trustworthy. Without these precautions, the measurement setup played a significant role in distorting memory effects.

With a PA that has an output power of 100 mW or less and has a gain of at least 10 dB, a linearity as good as -80 dBc for the input signal for certain setups can be achieved by feeding a signal directly from the VSG to the test PA [43]. However, the PAs used in this experiment operated at a high output power and did not supply a gain high enough such that the DUT could reach its P_{1dB} using the VSG alone to supply its P_{IN}. This chapter gives results on two amplifiers that require a higher P_{IN} than the VSG could produce: a 30 W two-stage Class AB LDMOS PA module (1.95 GHz) and a 170 W peak-

envelope power (PEP) LDMOS PA (880 MHz). In addition to a linear VSG, these PAs require a highly linear preamplifier: a Stealth Microwave Amplifier (SMA) in this experiment. It has a P_{1dB} of 40 dBm and a third-order output intercept point (OIP3) of 50 dBm. At the highest output power level of operation, which was 25 dBm, this gave a worst-case IMD3 of < -50 dBc.

Even with the setup in Figure 3.4, measurement artifacts crept into the results. Figure 3.5 shows a graph of one of these early fundamental tone measurements of a 30 W two-stage Class AB LDMOS PA. This graph should show a constant slope as the power increases and zero slope across the frequency axis, which represents the spacing of the tones in frequency. However, there are miscellaneous distortions and even incorrect input power settings. Specifically, for a tone spacing range of 50-100 kHz, variations in P_{OUT} from the DUT can be seen in Figure 3.5 for output power levels of approximately $P_{OUT} - P_{1dB} = -10\,dB$ and higher. This has two potential sources. The first is that the P_{IN} was lower than intended. The second is that the nonlinear behavior of the SA caused it to incorrectly read the relative power levels of the tones. This can occur when its span and resolution bandwidth (RBW) are changed. Another anomaly is seen at a tone spacing of 10 kHz. In this case, there is an incorrect power setting three steps below the highest P_{OUT} level shown. This was a programming error. In any case, all these distortions were due to either operator error or undesirable effects from the measurement setup.

Memory effects cause intermodulation distortion asymmetries that, relative to the carrier, can be small and thus hard to detect. For example, the IMD3 is 30-40 dB down from the carriers, as shown later in Figures 3.12 and 3.14, and the linearity due to memory is 10-20 dB below the memoryless nonlinearity [40]. The minor fluctuations in

the IMD3 due to memory effects were often 1 dB or less, as shown later in Figure 3.14, and they needed to be resolved in order to extract their memory effects [40].

The next few subsections go step-by-step and show the various artifacts encountered in these measurements and how each was dealt with. The clearest way to illustrate the errors and the subsequent solutions is to first address how the tones and IMD products were measured and then to follow it with how the desired P_{IN} level was ensured.

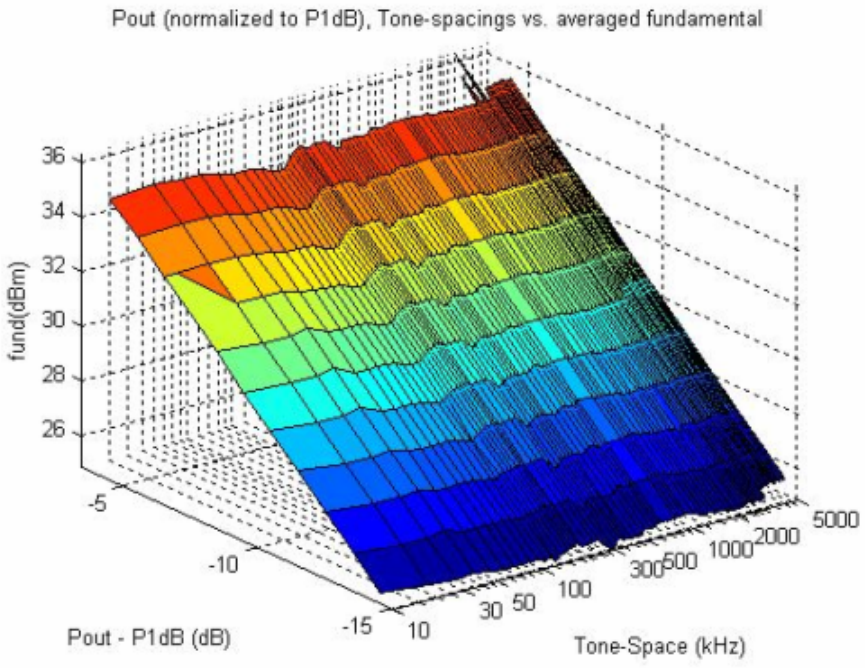

Figure 3.5: An early measurement of the fundamental tones of a 30 W Class AB LDMOS PA.

3.4.1. Spectrum Analyzer Artifacts

The first issue to cover is that of glitches in the levels measured by the SA. Figure 3.6 shows a graph of fundamental tones and IMD3 for a 30 W Class AB LDMOS PA module. Taking the differences between the amplitudes of the upper and lower fundamental tones, as shown in Figure 3.6(a), and upper and lower IMD3, as shown in Figure 3.6(b), highlights 12 spikes in the fundamental tones and nine spikes in the IMD3. These spikes are glitches in the amplitudes measured by the SA. A positive spike indicates that the peak amplitude of the upper frequency component was captured and the peak amplitude of the lower frequency component was missed. A negative spike indicates that the peak amplitude of the lower frequency component was captured and the peak amplitude of the upper frequency component was missed.

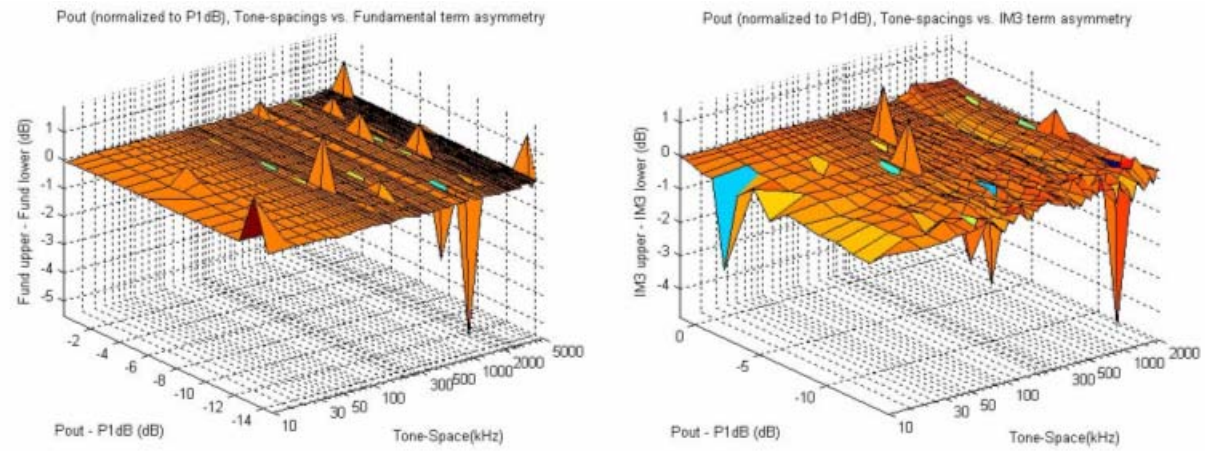

(a) (b)

Figure 3.6: Fundamental and IMD3 asymmetry graphs of a 30 W two-stage Class AB LDMOS PA module. By taking the difference between the upper and lower tones and products measured, these graphs highlight the glitches in the measurement. Each spike shown in these graphs illustrates a measurement glitch.

The source of these measurement glitches was the SA peak search function. When run remotely by the program Agilent VEE, this function would miss peaks often enough that its use had to be discontinued. To work around this, each peak and the marker were centered on the SA before recording the point. Even with this precaution, a number of glitches were still received. To further improve things, averaging was enabled in the SA. This presented a trade off between measurement accuracy and measurement time. Increasing the number of averages by one increased the test time by a few seconds per point measured. Since the total number of points measured in a test was around 11,000 points, these tests easily took up to 15 hours to complete. In the end, the optimum setting for the averaging was three. This reduced the number of glitches to 1 per 600 points measured by the SA. For the ~11,000 points measured, this would result in ~18 glitches for all fundamental tones and IMD. Reducing the glitches this much made it practical for these points to be manually measured for verification or interpolated with reasonable accuracy.

Figure 3.7 shows the results of the efforts to eliminate glitches for the fundamental tones of the same PA module. Using averaging and the careful placement of measurement markers, it can be seen that there are no peaks rising above 0.5 dB, which indicates an absence of glitches in the data. Instead, the fundamental tones are highly uniform and their differences do not exceed 0.08 dB.

Another key issue with the SA is its nonlinearity [4]. Though only power ratios, and not the absolute power, are required, it is imperative that the spectrum analyzer operate as linearly as possible. It was found that this presented a sizeable trade off in time. At first, to reduce measurement time, a loop was run in the control program to

detect when the bandwidth of the IMD products exceeded that of the span of the SA, and the span and RBW of the SA were increased to fit all the IMD products within its span. This cut measurement time by a factor of eight. However, the results were unusable. As the RBW was increased, it also increased the amount of power allowed into the SA. As a safeguard at select span/RBW thresholds, the SA would switch to a higher attenuation at its front end. Doing that broke the continuity of the measured amplitude points, which resulted in a sharp transition in the result recorded by the SA [4].

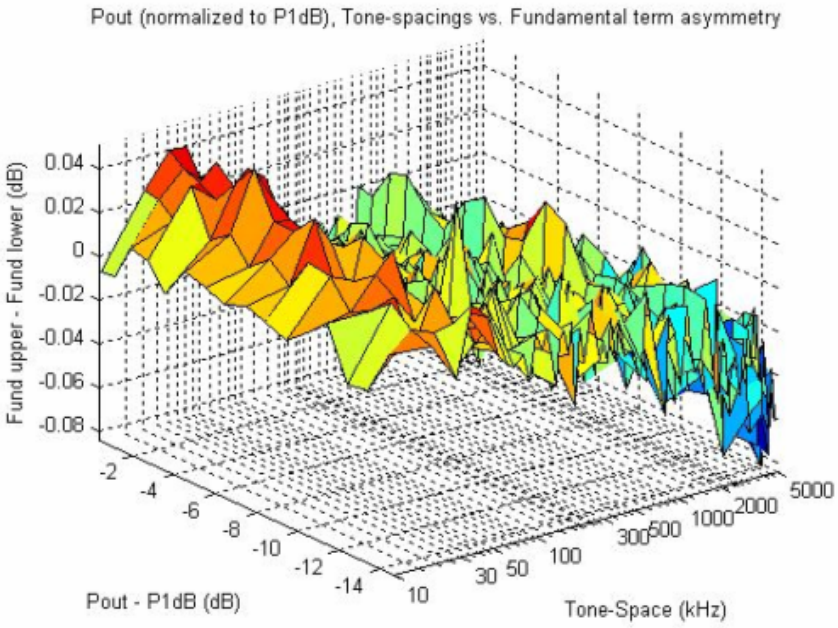

Figure 3.7: This is a graph of the fundamental tones for the 30 W Class AB LDMOS PA module. This graph illustrates by its flatness the elimination of glitches in the final measured points [42].

Figure 3.8 shows what can happen when this approach is taken. Though these graphs have no glitches in them, the amplitudes of their measured tones are far from flat for any given power level. The figure gives the average of the upper and lower fundamental tones over the 5 MHz bandwidth. In Figure 3.8 (a), a graph shows the averages of the upper and lower fundamental tones with respect to fundamental tone

spacing in frequency for a 170 W PEP LDMOS PA module at three different power levels. Sharp transitions in power levels read by the SA are easily seen here at several tone-space settings. Figure 3.8 (b) shows this more clearly by focusing on one of these power levels. In this graph, which should be a relatively flat line, the high and low points measured were 51.7 and 50.5 dBm, respectively. This gave a maximum variance of 1.2 dB, which was due solely to the nonlinear behavior of the SA. In Figure 3.8(b), amplitude variations can be seen at nearly every point. Sharp transitions occurred at 10 different tone spacings: 40, 70, 130, 280, 380, 950, 1000, 1250, 1800 and 2900 kHz. Sharp transitions indicate changes in input attenuation in the SA at select span/RBW thresholds [4], and gradual transitions indicate changes in the span and RBW. Some settings, such as the level of attenuation for the RF-in port, were set to be changed automatically by the SA itself. Other settings, like the span and RBW, were specified by the user.

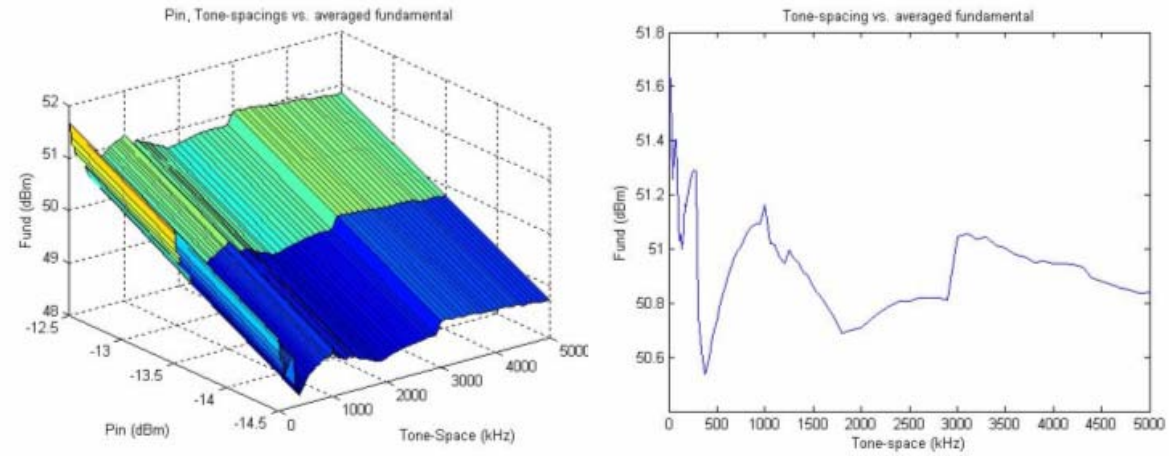

(a) (b)

Figure 3.8: Part (a) is a graph of the average of upper and lower fundamental tones vs. frequency spacing in a 170 W PEP LDMOS PA module when the span and RBW of the SA varies. This is shown for three power levels. Part (b) is a graph of the average of upper and lower fundamental tones vs. frequency spacing in the same 170 W PEP LDMOS PA module for a P_{IN} of -12.5 dBm.

This problem was addressed by fixing the span and RBW settings on the SA. The span was fixed to 50 kHz and the RBW to 300 Hz. Fixing the span and the RBW results in a set attenuation level on the SA for all measurements and a set amount of bandwidth over which the SA could read power. This eliminated such variations in the amplitudes recorded by the SA.

3.4.2. Setting P_{IN}

Even with the aforementioned precautions, a measurement of this setup without the DUT still shows variations in the fundamental tones, as shown in Figure 3.9, which would then be applied to the PA. In this case, the isolators, which do not have a flat frequency response, are suspect. Though free of glitches and sharp variations present in earlier measurements, Figure 3.9 shows variations in path loss for the fundamental tones based on the spacing between the two fundamental tones. Since this relates to the steps used to ensure an accurate P_{IN} to the DUT in Figure 3.4 and to calibrate the setup, an explanation for the steps taken to account for the preamp and the passives in the measurement is presented next.

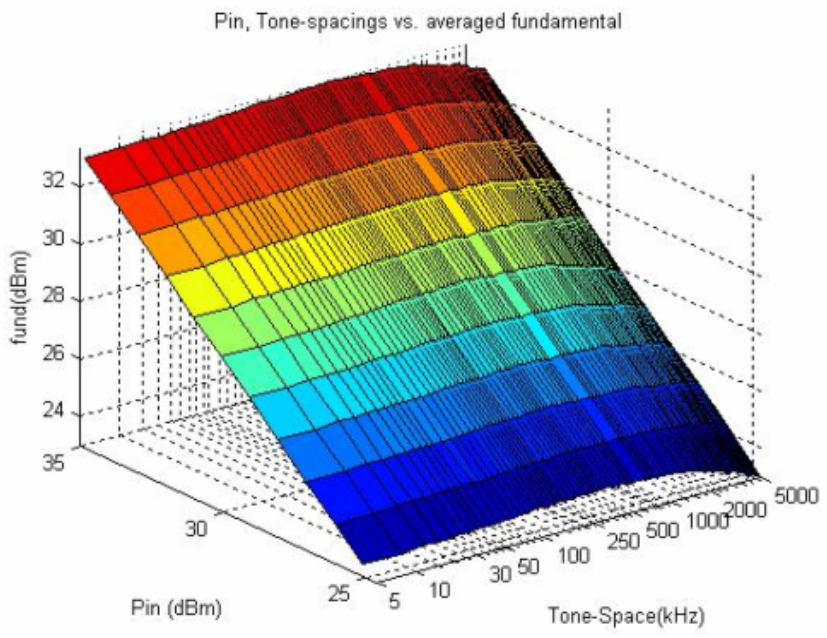

Figure 3.9: Variations in the fundamental signal from the test setup [42].

There were two main steps to the calibration: accounting for the passives with an Agilent 8753E VNA and accounting for the full setup, including the preamp, by a two-tone thru measurement. Since the setup has many cables, attenuators and isolators, it was necessary to measure each stage with the VNA. S_{11} and S_{21} of the passives were measured at the center frequency of operation in the following stages: VSG to preamp, preamp to DUT, DUT to SA and DUT to RFPM. This step allowed compensation for the path loss and allowed the P_{IN} to the DUT to be set to within 1 dB of what was intended. The result of this effort is shown in Figure 3.9. A different view of this same result is shown in Figure 3.10. In this figure, the difference between all the measured points and the maximum measured point for each power level is taken. In this way, the variation for this setup is shown not to exceed 0.7 dB. Figure 3.10(b) shows that the variation at the highest power setting from part (a) does not exceed 0.6 dB.

Figure 3.11 shows the measurements of the fundamental tones for the 30 W two-stage Class AB LDMOS PA module when the measurement setup still has these variations. Just as in Figure 3.10, this figure shows the difference between all the measured points and the maximum measured point for each power level. Notice that, though this is not patterned as nicely as the results shown in Figure 3.10, this does show variations of just over 0.35 dB over the range of tone frequency spacing at the highest power level, as shown in Figure 3.11(a). Taken at more power levels, Figure 3.11(b) shows the variations exceeding 1.5 dB.

To improve the flatness of the fundamental tones, a two-tone thru measurement was taken. For this step, the setup is connected as shown in Figure 3.4 but without the DUT. The run sweeps the power over several decibels and the tone spacing over a range of frequencies. The fundamental tone measurements taken from this sweep are shown in Figure 3.9, where the power range measured was truncated in the graph to make variations in fundamental tone amplitudes easier to see. The original power settings for the VSG were from -35 dBm up to 0 dBm, which brought the SMA up to its P_{1dB} of 40 dBm. Note that the variations in Figure 3.9 appear to depend solely on the frequency spacing of the fundamental tones and to be independent of the power level.

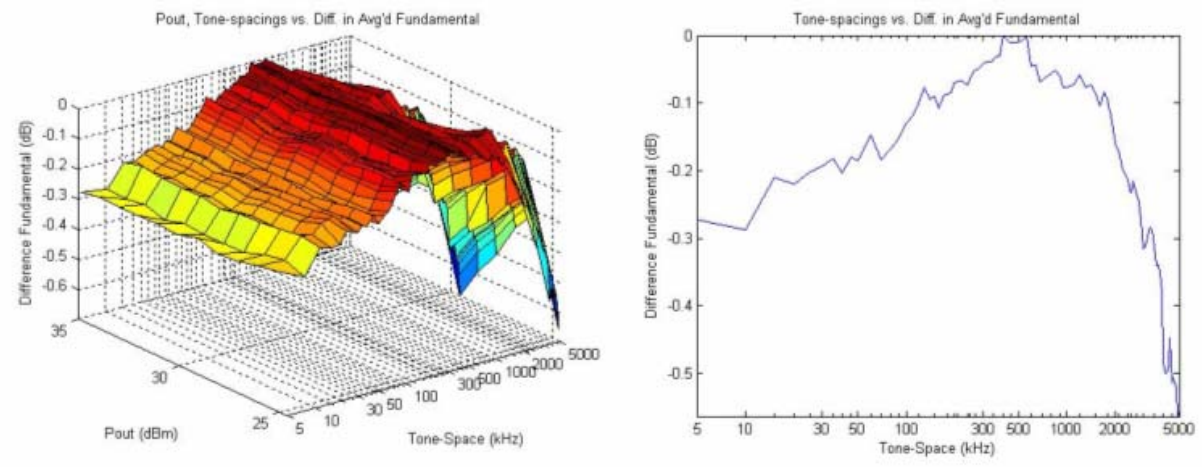

(a) (b)

Figure 3.10: Graph (a) shows the difference between the maximum point measured at each power level in Figure 3.9 and all other points measured at that power level. Graph (b) focuses on the difference given at an output power of 33 dBm.

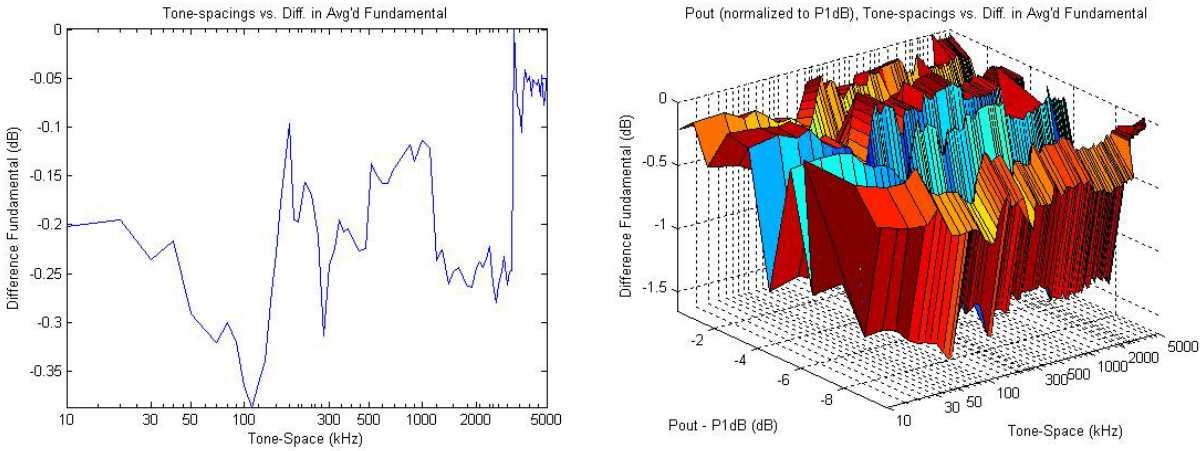

(a) (b)

Figure 3.11: Graphs of the fundamental tone measurements of a 30 W Class AB LDMOS PA taken without a two-tone thru calibration.

From this two-tone thru measurement, a calibration file was made. The calibration file contained five columns of data: the signal generator (SG) amplitude setting for the calibration run, the two fundamental tone levels measured from this run, the tone spacing

and the input signal amplitude the DUT would need. The data in this file were used to eliminate the variations in input power to the DUT.

The IMD products are not included in the calibration file. Since IMD3 was <-50 dBc at the SMA output power of 25 dBm, it gave acceptable accuracy for the model to be extracted. Though the IMD3 is 30 dB higher for this two-tone test than it would be using the setup in [43], this quantity can be improved by using a preamplifier with a higher OIP3. Typically, the cost of an amplifier increases exponentially in proportion to the linearity it is able to achieve.

When calibration steps were completed, the DUT was added back into the setup so that it resembled Figure 3.4. Before running the test, the maximum P_{IN} for the DUT had to be set to ensure that the DUT reached, but did not exceed, its P_{1dB}. The settings in the calibration file were changed to ensure this maximum P_{IN}. Though many memory effects were revealed well below the P_{1dB} of the DUT, the DUT had to be run into compression for some of the modeling [39].

After the maximum P_{IN} was ensured, VEE, the measurement control program, took data from the calibration file entry-by-entry. VEE averaged the levels of the fundamental tones it extracted from the calibration file, took the difference between that calculated average and the ideal P_{IN}, and then added this difference to the original VSG amplitude setting used in the calibration run. The result was that the VSG plus the preamp gave an amplitude-leveled P_{IN} to the DUT. Also amplitude measurements were adjusted within VEE to account for attenuation in the setup. Finally, the VSG used its ARB function to generate the two fundamental tones.

To measure each tone, the SA placed the marker and the tone to be measured in the horizontal center of its screen. In this manner, the amplitudes of the upper and lower fundamental tones, the IMD3 products, the IMD5 products and the IMD7 products were measured and recorded. VEE then changed the tone spacing or power level, and the SA measured another set of tones and products.

When the measurements of the 30 W two-stage Class AB LDMOS PA module were rerun using this calibration method, there was a marked improvement in the flatness of the fundamental tone levels measured, as shown in Figures 3.12 and 3.13. In Figure 3.12(a), it can readily be seen that the flatness of the fundamental tones has improved. Even after going through the PA, these fundamental tones are more level than the fundamental tones measured in the thru run shown in Figure 3.9. It is interesting to note from Figure 3.10, which displays the variance from the maximum point in each power level, that the improvement in the effects of leveling the P_{IN} of the fundamental tones is reduced the closer the measurement is to the noise floor.

3.5. Comparison of IMD Measurements

As the Volterra model illustrates, the IMD products intermix with each other. That is, the IMD3, for example, is the sum not just of third-order vectors but also of third- and fifth-order (and even seventh-order) vectors and not just third-order vectors. In [2], the author uses the complex signal domain to illustrate that these third- and fifth-order vectors all add in phase for the memoryless PA. This results in symmetrical IMD3 in the upper and lower sidebands.

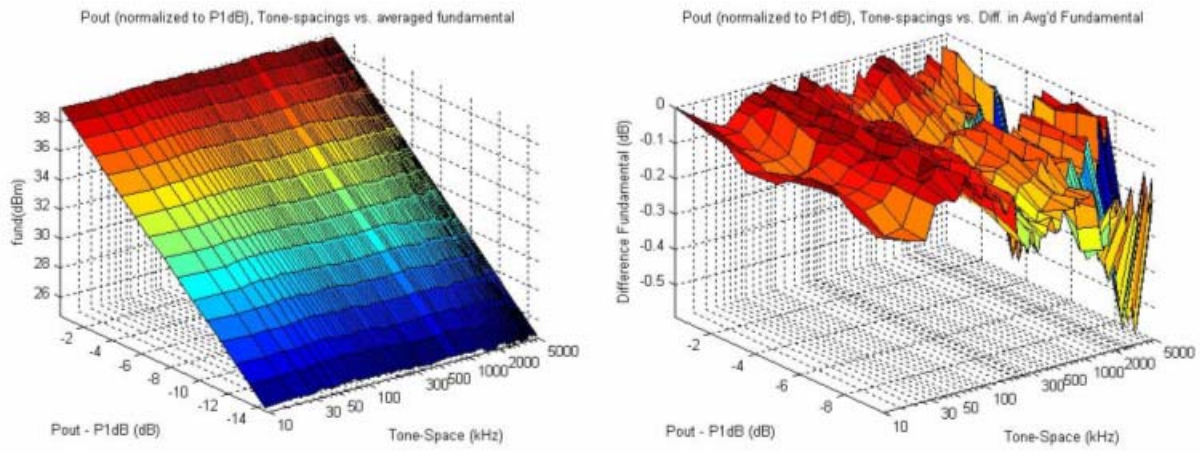

(a) (b)

Figure 3.12: (a) Fundamental signal average for a 30 W two-stage Class AB PA module when setup is calibrated [42]. (b) Same data taken as a difference from the maximum point in each power level measured.

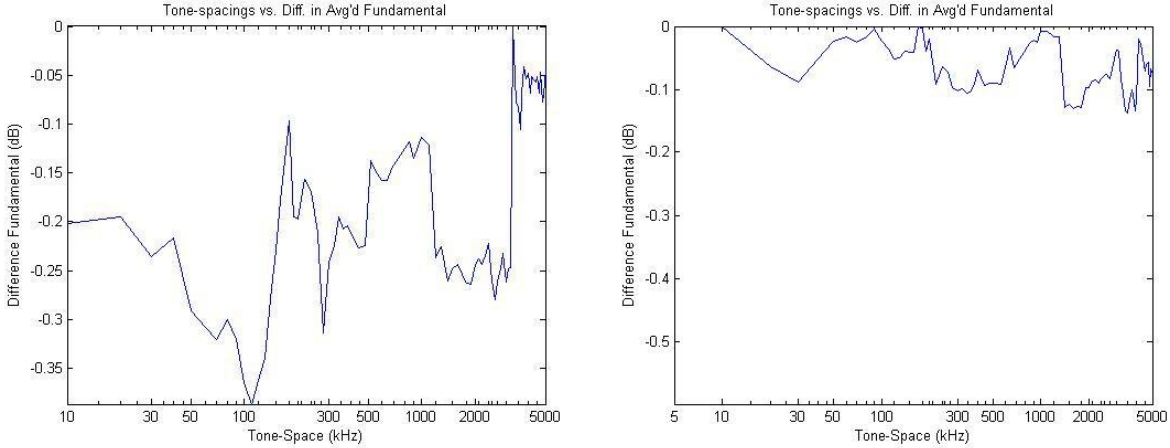

(a) (b)

Figure 3.13: Variance in fundamental tones for the highest power level of the 30 W two-stage Class AB LDMOS PA module without (a) and with (b) calibration.

For the quasi-memoryless PA, there is both phase and amplitude distortion. Though the amplitudes are symmetrical, the third- and fifth-order phases in the upper and lower sidebands are offset from each other. These phase offsets result in different levels of constructive and destructive addition in the IMD3 of the upper and lower sidebands,

which results in their being asymmetric. Furthermore, these phase offsets, which are due to AM/PM, change based on the magnitude of the input signal.

When strong memory effects are present in a PA, the magnitudes of third- and fifth-order vectors become asymmetrical and their phases are also offset. This makes them add unpredictably. Whereas in the memoryless or quasi-memoryless cases where errors in data can be easily observed as scalar differences in magnitude in expected IMD behavior, it is not so straightforward for the case of the PA with memory. For the PA with memory, the accuracy of the model can be severely impacted by data taken in an uncalibrated setup. As will be shown in this section, errors in data taken from an uncalibrated setup versus data taken from a calibrated setup can give two very different models from the same PA.

3.5.1. Memoryless PA

At the highest power level, shown in Figure 3.13, the average fluctuation in the fundamental tone changed from approximately 0.2 dB before calibration to about 0.05 dB after calibration. The motivation for reducing the fluctuation in the fundamental tones is to reduce its influence on the IMD products. From the behavior of the 10 W LDMOS memoryless PA, an appropriate goal would appear to be to reduce the unwanted fluctuation in IMD products to where they are below any change in the IMD products due to the PA. This assumes the fluctuations are added on top of the already-present IMD product and are done so in phase. It does not assume that the fluctuations would cause a fundamental change in the behavior exhibited by the IMD. Assuming these things, the question is how much did this improvement in the fundamental tones also improve the

IMD products? Since, due to the clear correlation seen between a change in fundamental tones and the IMD products, this appears to be a good assumption for the memoryless 10 W Class AB LDMOS PA, the analysis here will start with comparing this PA to the theoretical behavior of a memoryless Class A PA.

Table 3.2 shows what can be expected theoretically when the amplifier is operating as Class A. The improvement for IMD3 is 0.45 dB, 0.75 dB for IMD5 and 1.05 dB for IMD7. For the 10 W Class AB amplifier, the improvements would be 0.6 dB for IMD3, 0.675 for IMD5 and 0.825 dB for IMD7.

Table 3.2: Projected change in IMD resulting from flattening the frequency response of the fundamental tones for Class A and Class AB memoryless amplifiers as they near compression.

Type	ΔFund. (dB)	ΔIMD3 (dB)	ΔIMD5 (dB)	ΔIMD7 (dB)
Class A (uncal)	0.2	0.6	1.0	1.4
Class A (cal)	0.05	0.15	0.25	0.35
10 W Class AB (uncal)	0.2	0.8	0.9	1.1
10 W Class AB (cal)	0.05	0.2	0.225	0.275

Relative to the behavior of a Class A PA, fluctuation in the fundamental tones effects either a greater (IMD3 for the 10 W case) or lesser (IMD5 and IMD7 for the 10 W case) change in the IMD. Though this relationship has not been reduced to analytical terms in this work, it is easy to see that the variation in the IMD products is connected to the variation in the fundamental tones. That is, where the fundamental tones increased or decreased in power, the IMD products increased or decreased, respectively. It should be noted from the measurements of the memoryless 10 W Class AB LDMOS PA that the effects of fluctuations in the fundamental tones were only seen above the noise floor.

3.5.2. PA with Memory

Figure 3.14 shows the IMD3 measurement results for the 30 W two-stage Class AB LDMOS PA module with memory. The left-hand figures show measurements taken before the setup was calibrated. The right-hand figure shows measurements taken on a calibrated test setup.

The IMD3 graphs—especially the ones showing asymmetry—most clearly show a difference between the uncalibrated and calibrated measurements of a PA. Since IMD3 is approximately 20 dB above IMD5 and 25 dB above IMD7, both of which are close to the noise floor, it is able to be clearly analyzed over several decibels of power. Its level to IMD5 and IMD7 also make it the dominant component in the extracted parallel Wiener model. Graphs of the IMD3 taken with and without calibration are shown in Figure 3.14.

For the well-behaved, practically memoryless 10 W LDMOS PA, it was seen in Figures 3.2 and 3.3 and in Table 3.1 that its IMD varied with the fundamental tones in an easily-seen pattern when above the noise floor. However, for this 30 W LDMOS PA module, the effects of variation in the fundamental tones change the asymmetry markedly, making the two different measurements appear to be of two different amplifiers altogether. This is most clearly seen in IMD3. It is seen to a lesser degree in IMD5 and IMD7.

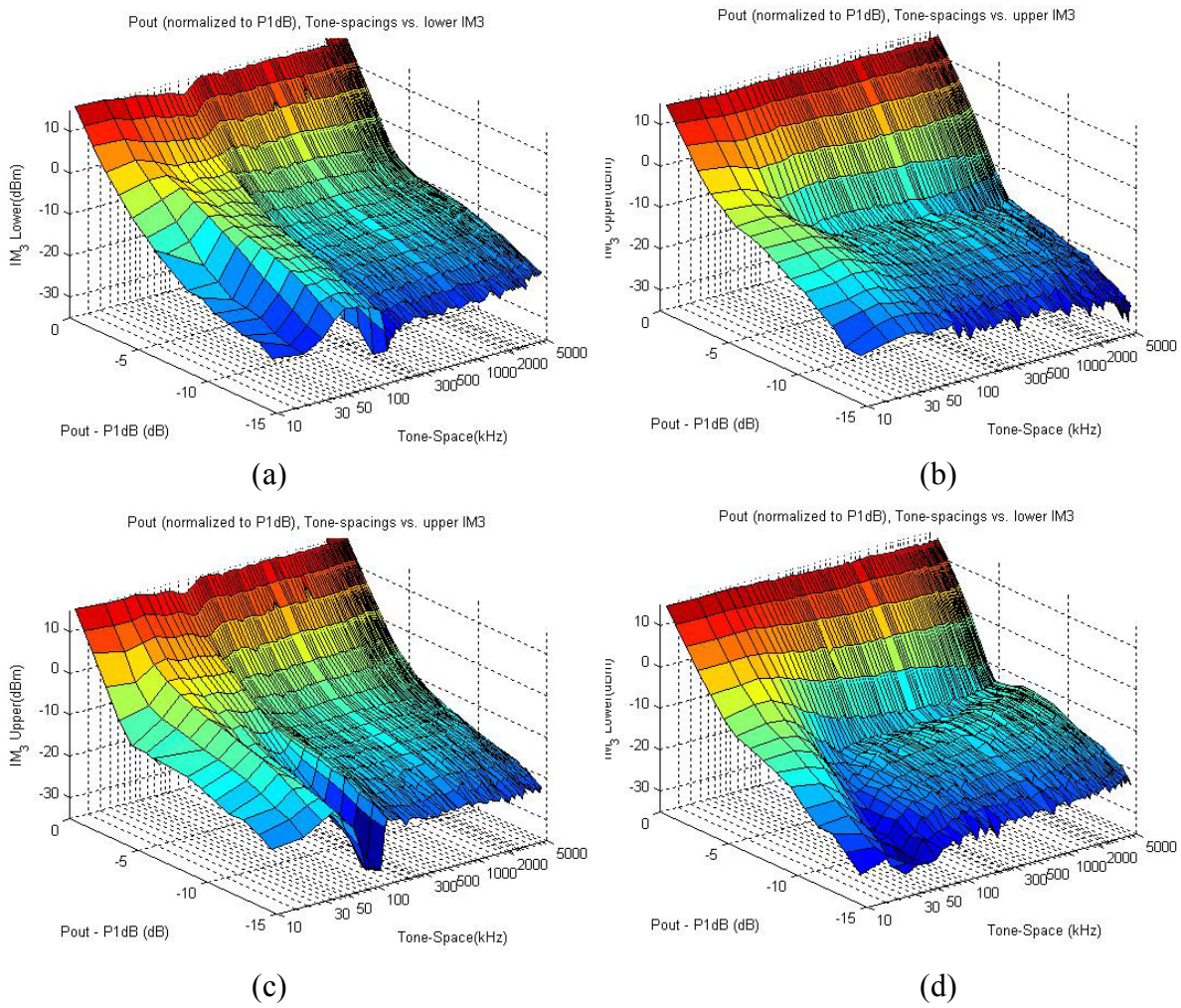

Figure 3.14: Two IMD3 measurements of the same 30 W two-stage Class AB LDMOS PA module. The figures on the left are those taken with an uncalibrated setup. The figures on the right are from the calibrated setup. The IMD3 in the lower sideband is given by (a) and (b). The IMD3 in the upper sideband is given by (c) and (d).

For the IMD3 asymmetry, it can easily be seen when comparing Figure 3.14 (e) and (f) that the uncalibrated IMD3 is weighted differently in most places and is inverted in some places. Table 3.3 lists several points taken from these graphs to illustrate this. Depending on the level of fluctuation in the fundamental tones, they can either change the weighing of the final IMD or even invert their asymmetry such that the IMD3 in the

upper and lower sidebands switch as to which is more dominant. Together these effects make the PA measured with the uncalibrated setup appear to be a different PA from that measured using the calibrated setup.

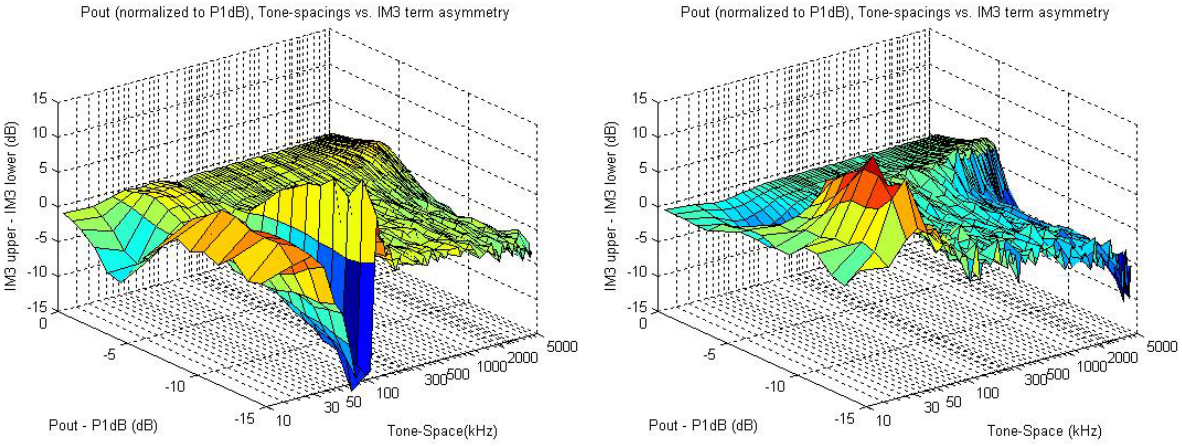

(e) (f)

Figure 3.14 (cont'd): The asymmetry between the IMD3 products in the upper and lower sidebands is given by (e) and (f).

Table 3.3: A list of IMD3 points taken from graphs shown in Figure 3.14 (e) and (f).

Tone Spacing	$P_{out} - P_{1dB}$ (dB)	Asymmetry (dB) Calibrated Setup	Asymmetry (dB) Uncalibrated Setup
50 kHz	-10.44	14.26	-4.89
100 kHz	-14.92	1.49	-14.38
50 kHz	-0.42	-0.78	0.26
4.8 MHz	-4.17	3.19	1.59

As explained in [2], asymmetry is one key indicator of the existence of memory. As shown in Figure 3.15 (a) and (b), the calibrated and uncalibrated measurements of the IMD3 especially show very different asymmetrical behavior. Thus, above the noise floor, the calibrated and uncalibrated measurements of the same PA with memory, if extracted

into models, would give two very different models. That is, each model would, in essence, exhibit distinct memory effects. Thus, the small and large asymmetries, which are both needed in characterizing the memory effects of a PA, are both made useless without first ensuring a calibrated setup, which includes ensuring a well-behaved set of fundamental tones.

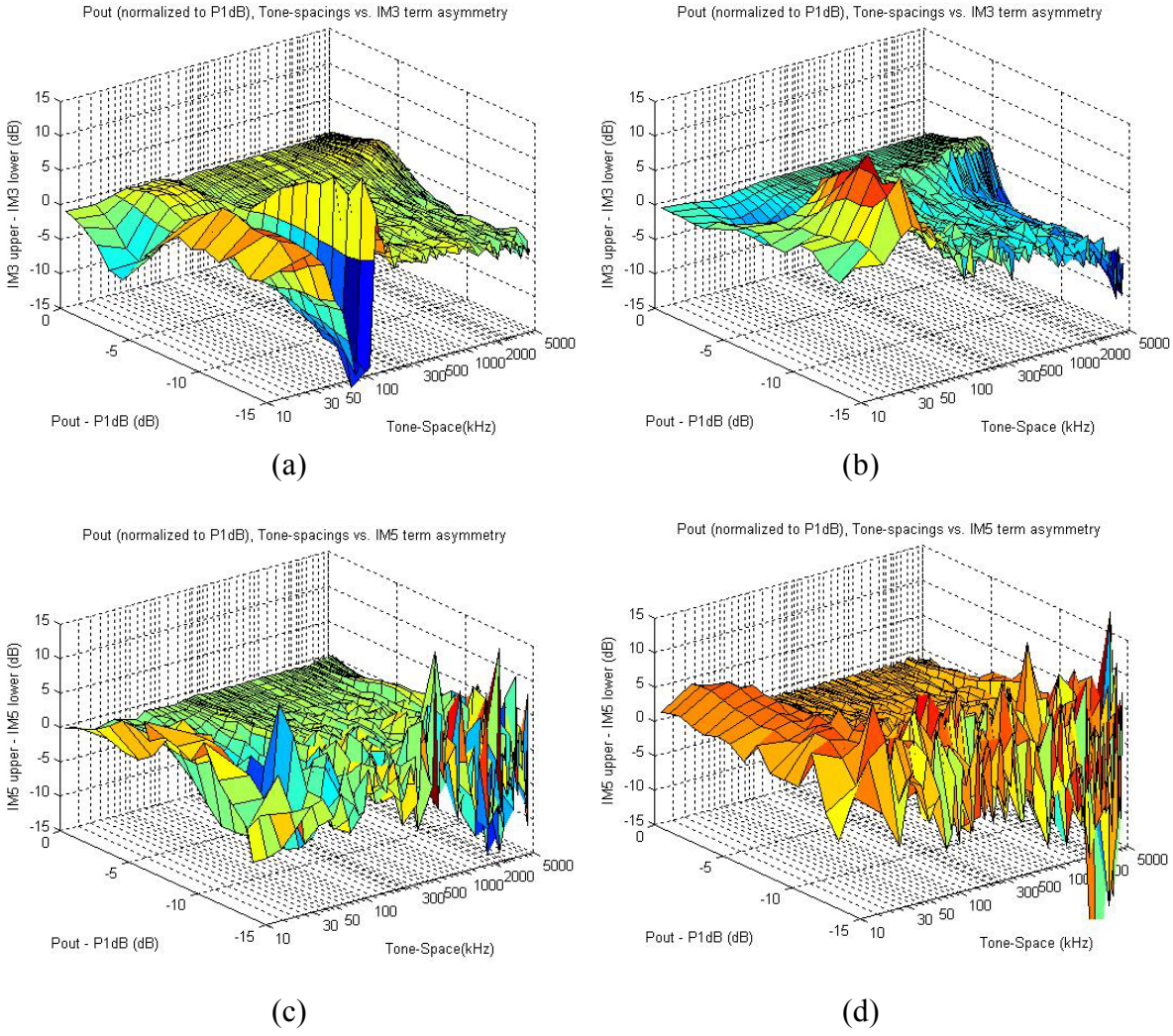

Figure 3.15: IMD measurements for the 30 W two-stage Class AB LDMOS PA module taken with an uncalibrated (left-hand figures) and calibrated (right-hand figures) setup. The IMD3 asymmetry is given by (a) and (b). The IMD5 asymmetry is given by (c) and (d).

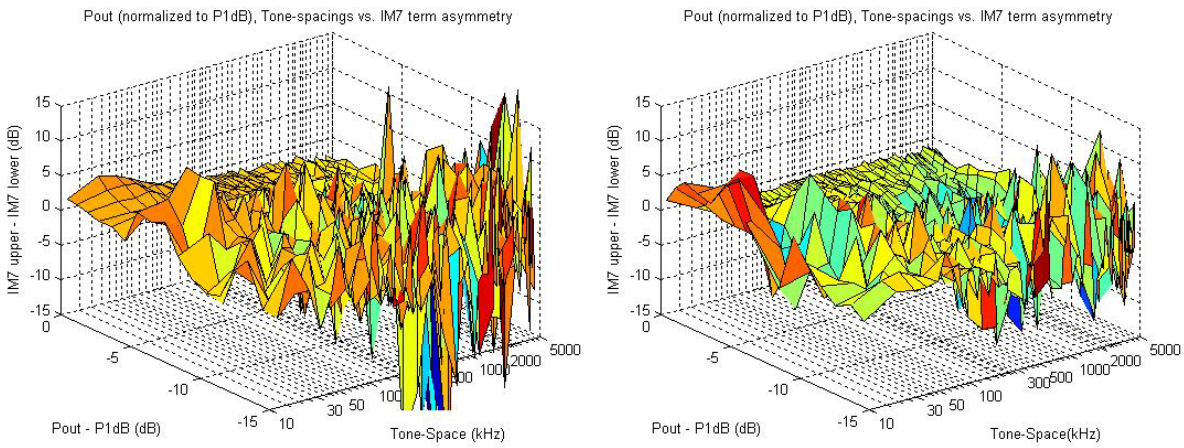

(e) (f)

Figure 3.15 (cont'd): The IMD7 asymmetry is given by (e) and (f).

3.6. Conclusions

This section focused on the measurements related to characterizing memory effects in power amplifiers. The setup was optimized to measure high power amplifiers that needed input powers >10 dBm. The main sources of error in the measurement setup were the nonlinearity and other artifacts of the SA and the improper setting of P_{IN}.

Both a memoryless PA and a PA with memory were measured with and without calibration. Both PAs were Class AB. It was found that the IMD behavior of the Class AB memoryless PA did not track with that of the Class A amplifier. However, the IMD variations in the Class AB memoryless PA appear to track in-phase with variations in the fundamental tones. That is, an increase in the fundamental tones gives an increase in the IMD and vice versa.

It was also noted that a PA with strong memory effects results in IMD vectors of the upper sideband having different amplitudes and phases as compared to those in the lower sideband. This causes the various odd orders of vectors to add unpredictably. It was

found in the resulting IMD data that the accuracy of the memory effects was greatly degraded in the presence of data errors, such as those in the uncalibrated measurements. The IMD asymmetry between the data taken without calibration and that taken with calibration on the 30 W two-stage Class AB LDMOS PA module were so different that models based on them would not even be recognizable as coming from the same PA.

Chapter 4: Modeling Propagation Environments

4.1. Introduction

This chapter introduces the concept of modeling in multipath environments. In general, a channel in a multipath environment is treated as a collection of linear time-varying filters, where the time variance of the channel is independent of the input signal [44]. Studies in modeling multipath channel characteristics will often start with three classic narrowband models: Gauss, Rayleigh and Rice [44]-[48]. The Gauss model includes only the signal and Gaussian noise. It is the best-case channel since it includes one dominant signal—and noise—with no interfering multipath copies of this signal and no path loss. The worst case channel is given by the Rayleigh model. Along with including noise, the Rayleigh multipath is so severe that no received signal is dominant compared to the others and signal fades are often deep. Bridging the divide between

Gauss and Rayleigh is the Rice model. It contains both Gauss and Rayleigh PDF representations within its PDF expression, reducing to one or the other in special cases. Even more recent multipath models often have Gauss and Rayleigh components in their PDFs and reduce to at least Rayleigh in special cases [47].

Due to their relevance and prominence, these three classic multipath models will be introduced in this chapter after first discussing the multipath environment. In addition to this, some other narrowband multipath models that are also commonly used will be briefly introduced.

In the last section, the implications of wideband signals in multipath environments will be discussed. Though narrowband signals allow the understanding of aspects of multipath, they require some simplifying assumptions that are not relevant to the present work, which is wideband. The last section in this chapter will introduce considerations needed for wideband cases.

4.2. Multipath Environment

Except for unrealistically simple cases, multipath environments have so many variables that they are impossible—or nearly impossible—in most cases to model deterministically. Path loss, shadowing and fading are three of these variables that affect transmitted signals in various ways, as illustrated in Figure 4.1. Due to the large number of variables, statistics must be used when modeling multipath [44]. Signals transmitted over the air can be scattered, reflected and diffracted [45], which results in shifts in frequency [47], delays in time [44], and variations in angles of arrival at the receiver [47]. A signal scatters when the size of an object on which it impinges is on the order of a

wavelength or less. Reflection occurs when the size of the object on which the signal impinges is much greater than a wavelength. Diffraction happens when the primary signal encounters an obstacle such that secondary waves are produced behind it [45]. Shifts in frequency (i.e. Doppler shift) occur when a signal copy encounters a moving object in its propagation path. Time delays occur when a signal copy takes a path that is longer than the line-of-sight path between the transmitter and the receiver.

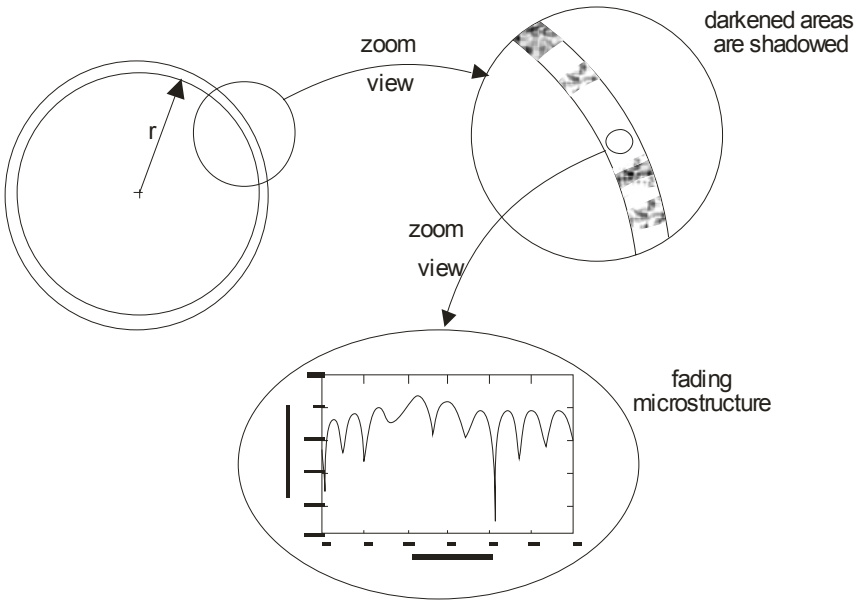

Figure 4.1: Relationship between path loss, shadowing and fading [44].

In essence, the multipath environment produces multiple copies of the original signal and causes them to take multiple paths, where each path affects its signal copy uniquely, before reaching the receiving antenna. These effects cause multiple distorted copies of the original signal to arrive at the receiver. These copies add vectorially (and often destructively) at the receiver to give the final distorted signal. The final signal at the receiver can be great or small depending on how these phases line up. The overall term commonly used to describe the effects of this type of channel is multipath fading [47],

which is a fluctuation in the envelope of the signal [45]. Though fading happens in space, the receiving antenna, which is often not distributed in space, experiences such things as a function of time as the receiver moves through its multipath environment [47].

Fading is further described as fast or slow. Fast fading gives short-term fluctuations in the signal due to small movements in the transmitter, receiver or objects in the multipath channel. These movements are on the order of a half wavelength. Slow fading gives more long-term fades and comes from much larger movements in the transmitter, receiver or objects in the multipath channel [44], [47]. In practice, there is no clear cut division between these two types of fading, and they are usually viewed with the fast effects being superimposed upon the slow effects, as shown in Figure 4.2. In this figure, most common fast fades are less than 20 dB with a fair number of deeper fades exceeding 30 dB.

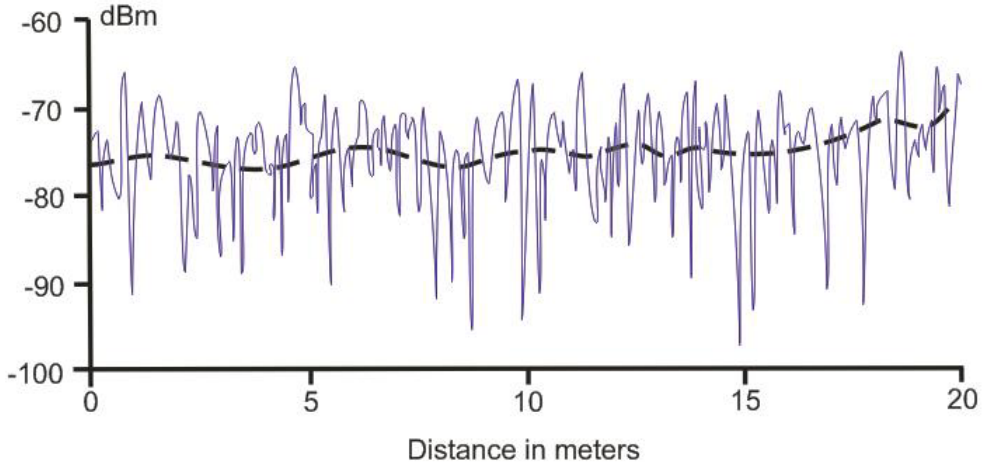

Figure 4.2: Experimental record of received signal envelope in an urban area, taken from [47].

The multipath environment is commonly referred to as a linear time-varying (LTV) channel [44] and is often represented by its impulse response, $h(t,\tau)$. The

derivation of $h(t,\tau)$ given in [49] illustrates the characteristics of the LTV property of a multipath channel. The first step is to assume that both the receiver and the transmitter are stationary with the receiver being at a fixed position *d*. This assumes that the channel is linear and time invariant (LTI). Using this, the system can be represented as $h(d,t)$. This impulse response of the system is given as a function of position with respect to the receiver and time with respect to the input signal.

If the input signal from the transmitter is taken to be $x(t)$, the received signal is given by the following convolution relation

$$y(d,t) = x(t) * h(d,t) \ . \tag{4.1}$$

In integral form, this becomes

$$y(d,t) = \int_{-\infty}^{\infty} x(\tau) h(d, t-\tau) d\tau \ . \tag{4.2}$$

The impulse response of the system in (4.2) now has three variables. The variables t and τ relate the time dependence of the response on the time nature of the signal.

Using the relation $d = vt$, where v is the constant velocity of the receiver, vt can be substituted into (4.2) and the variables of the impulse response function can be reduced to time only

$$y(vt,t) = \int_{-\infty}^{\infty} x(\tau) h(vt, t-\tau) d\tau \ . \tag{4.3}$$

Removing the constants from (4.3) and expressing it only in terms of its variables results in the expression commonly used to combine the input signal, $x(t)$, with the time-varying channel, $h(t,\tau)$, to obtain the final output, $y(t)$.

$$y(t) = \int_{-\infty}^{\infty} x(\tau)h(t,\tau)d\tau \tag{4.4}$$

where

$$h(t,\tau) = h(vt, t-\tau) = h(d, t-\tau) \tag{4.5}$$

Thus, it can be seen from (4.5) that $h(t,\tau)$ resembles a linear filter with the addition of time variation that is independent of the signal [50]. Though decoupled in the expression $h(t,\tau)$, t represents the time of measurement and $t-\tau$ represents the time when the impulse entered the channel [51].

The independence of the channel variation from the input signal adds an unknown to the environment. As can be seen, multipath environments quickly lead to the multiplication of variables: movement of the receiver or transmitter and the number of individual multipaths, even in the static case. This makes the exhaustive description of multipaths impossible and motivates the need for some level of simplification.

Due to the complexity and unpredictability of multipath channels, their effects on the input signals are commonly modeled as random processes. Probability techniques allow key simplifying assumptions, which greatly aid the ability to model the channel. These probabilistic methods allow the details of the multiple copies of the signal at the receiver to be summarized into the PDF of the model and into such key parameters as the mean, standard deviation and variance. This allows an environment to be described using

these key constants, which are surrounded by random deviations—the copies of the signal at the receiver. Thus, the number of variables can be reduced and the environment can be described adequately.

Nevertheless, there are definite contributors to signal distortion in a multipath environment: frequency (Doppler) shift, time delay and angle of arrival. Time delay and the varied angles of arrival due to scattering and reflection result in echoes of the signal arriving at the receiver at any given time. In this sense, radio multipath can be seen as similar to reverberating sound waves forming nulls and peaks in a room. Similar to the sound waves in this room, the signal in a multipath environment does not weaken linearly with distance. Also, unlike a signal traveling line of sight and having obstacles with a distance of at least 0.6 times the radius of the first Fresnel zone of the signal [52], which has the possibility of being predicted reasonably, multipath adds too many variables to a signal to make it easily predictable.

Mathematically, time delays and angles of arrival cause the signals to add vectorially at the receiver. As illustrated in Figure 4.3, these signals add over the full 360° phase range—and do not add in a simple ± (i.e., 0/180°) fashion—due to the various phase differences between the copies of the received signals. Therefore, for significant amplitudes, the phases play an important role in the integrity of the received signal [45], [53].

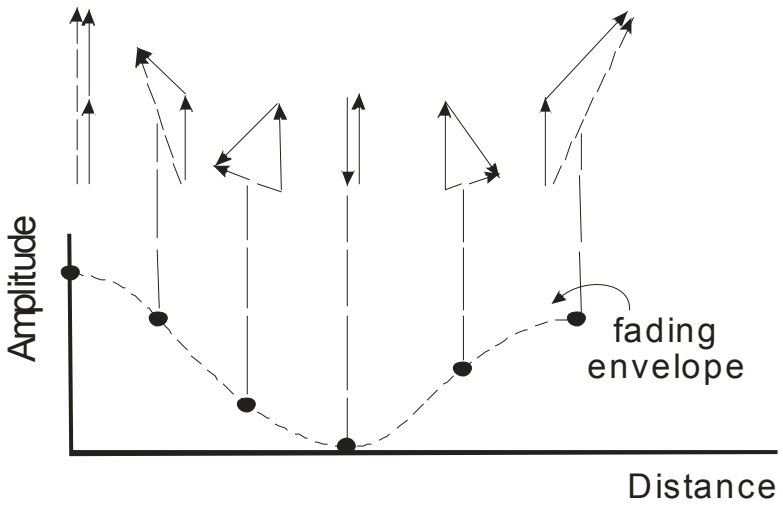

Figure 4.3: Envelope fading for two signals as they combine with different phases [47], [54].

In addition to the echoes from time delay effects, there are Doppler effects. Any moving objects that a signal (or one of its many copies) encounters will cause the signal to shift some amount in frequency. This is what is meant by a Doppler (or frequency) shift. The shifts in frequency from Doppler effects cause the spectrum to smear, producing, in effect, an increased error floor for the signal. This is illustrated for the n^{th} signal copy with a center frequency of f_c as follows [45]

$$\begin{aligned} f_n &= f_c + f_{D,n} \\ &\approx f_c + \frac{v}{\lambda_c}\cos\theta_n \ , \end{aligned} \tag{4.6}$$

where $f_{D,n}$ is the Doppler shift, v is the velocity of the reflecting object, λ_c is the wavelength of the center frequency, and θ_n is the spatial angle between the direction of motion of the reflection object and the direction of the wave impinging on it.

All of these effects are implied in channels described as linear time varying (i.e. multipath channels) with the result of causing fading in the composite received signal.

Since the common modeling methods describe the envelope of a signal, they are baseband representations. As such, it helps to see how these effects interplay.

The mathematical model given in [49] illustrates the inner mechanisms of the baseband $h(t,\tau)$ well.

$$h_b(t,\tau) = \sum_{i=0}^{N-1} a_i(t,\tau) e^{j2\pi f_c \tau_i(t)} e^{j\Phi_i(t,\tau)} \delta[\tau - \tau_i(t)] \tag{4.7}$$

Eq. (4.7) contains the real amplitude as a function of the input signal and channel variations with time, $a_i(t,\tau)$. It contains the phase shift of the i^{th} propagation path due to free-space propagation, $2\pi f_c \tau_i(t)$, which is based on the length of the path. Finally, it contains the excess phase shift encountered in the channel of the i^{th} propagation path as a function of the input signal and channel variations with time, $\Phi_i(t,\tau)$. Thus, Eq. (4.7) shows the variation of the LTV channel for the multipath waves as they combine at the receiving antenna in terms of delay, amplitude and phase. LTV equations similar to (4.7) are given in [44], [53] and [55].

Just as the input and output signals of a multipath channel can be represented in both time and frequency, the multipath environment can also be represented in multiple domains. In addition to time and frequency, the multipath channel also introduces delay and Doppler spread. Consequently, the multipath channel has four possible representations for these four domains, as given in Table 4.1.

Table 4.1: Functions representing the four multipath domains [45], [56], [57].

Function Name	Math Term	Channel Attributes	Input	Output
Time-Variant Transfer	$T(f,t)$	Frequency, Time	Freq: $Z(f)$	Time: $w(t)$
Input Delay-Spread	$g(t,\tau)$	Time, Delay	Time: $z(t)$	Time: $w(t)$
Output Doppler-Spread	$G(f,\nu)$	Frequency, Doppler	Freq: $Z(f)$	Freq: $W(f)$
Delay Doppler-Spread	$U(\tau,\nu)$	Delay, Doppler	Time: $z(t)$	Time: $w(t)$
Delay Doppler-Spread	$U(\tau,\nu)$	Delay, Doppler	Freq: $Z(f)$	Freq: $W(f)$

The time-variant transfer function $T(f,t)$ is used to perform a frequency-to-time conversion, where it takes the time dependence of the multipath channel into account [50], [56], [57]. Physically, this function best represents a multipath channel where there are minimal delay-scattering and Doppler-shifting elements. This allows the engineer to take advantage of frequency-domain analysis techniques—commonly used in fixed linear networks—in a variable linear network [50]. The I/O function for $T(f,t)$ is given in [56], [57] as

$$w(t) = \int Z(f)T(f,t)e^{j2\pi ft}df \ . \tag{4.8}$$

As can be seen from this equation, $T(f,t)$ represents the frequency domain of the channel but with a dependence on the time variable. Thus, the time output $w(t)$ is obtained by taking the inverse Fourier transform of the $Z(f)T(f,t)$ product.

The input delay-spread function $g(t,\tau)$ describes the response of the channel to a unit impulse [56], [57]. Since the delay is expressly modeled on the input side of the channel, and before the modulation by the differential scattering gain $g(t,m\Delta\tau)\Delta\tau$, $g(t,\tau)$ is used here to differentiate it from the more general $h(t,\tau)$ mentioned earlier.

Delay spread causes adjacent symbols to interfere with each other, resulting in intersymbol interference (ISI) [45] and frequency expansion around the signal frequency [51]. Thus, when ISI is dominant, the multipath channel is best represented by a model that has a continuous array of nonmobile reflecting scatterers [45], such as $g(t,\tau)$. The reflecting scatterers each produce modulation on the signal envelope, which is shown in the relation $g(t,\tau)d\tau$, in the interval given by $(\tau, \tau + d\tau)$. The I/O function is given by [56], [57]

$$w(t) = \int z(t-\tau)g(t,\tau)d\tau \,. \tag{4.9}$$

In discrete form, this is represented by [45]

$$w(t) = \sum_{m=0}^{n} z(t-m\Delta\tau)g(t,m\Delta\tau)\Delta\tau \,, \tag{4.10}$$

which allows the channel to be modeled as a series of delay taps $[\Delta\tau]$ and gains $[g(t,0); g(t,\Delta\tau); g(t, 2\Delta\tau)\ldots]$, as shown in Figure 4.4.

The output Doppler-spread function $G(f,\nu)$ represents the multipath channel as a continuous array of Doppler-shifted components, where each component is shifted in frequency in the interval $(\nu, \nu + d\nu)$. $G(f,\nu)d\nu$ equals the Doppler-spread generated by the Doppler-shifted components in the interval $(\nu, \nu + d\nu)$. Doppler shift creates new frequencies by shifting the signal frequency [51] and causes spectral broadening on the output spectrum. This results in co-channel interference (CCI). Thus, when CCI is dominant, the multipath channel is dynamic and is best represented by a model that has a continuous array of mobile Doppler-shifted scatterers [45], [47], such as $G(f,\nu)$.

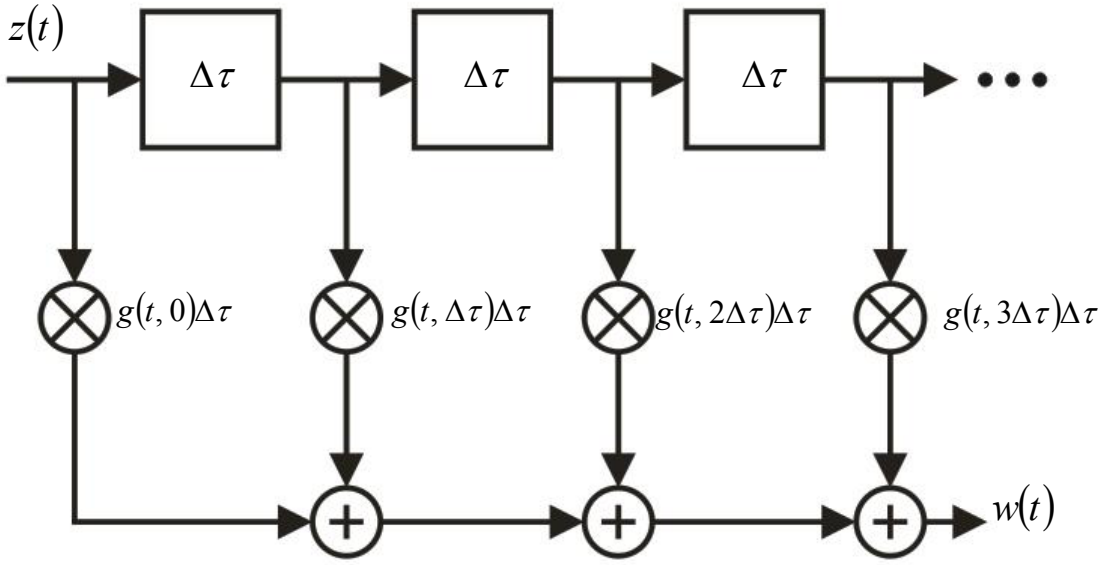

Figure 4.4: Discrete time-tapped delay line model for a multipath-fading channel [56], [57].

The I/O expression for the output Doppler-spread function is [56], [57]

$$W(f) = \int Z(f-\nu)G(f,\nu)d\nu \tag{4.11}$$

The discrete representation is given by [45]

$$W(f) = \sum_{m=0}^{n} Z(f-m\Delta\nu)G(f-m\Delta\nu, m\Delta\nu)\Delta\nu \tag{4.12}$$

This allows the multipath channel to be represented by a bank of filters with transfer functions $G(f,\nu)d\nu$ followed by a frequency-conversion chain that produces the Doppler shifts. Figure 4.5 gives a graphical representation of this model.

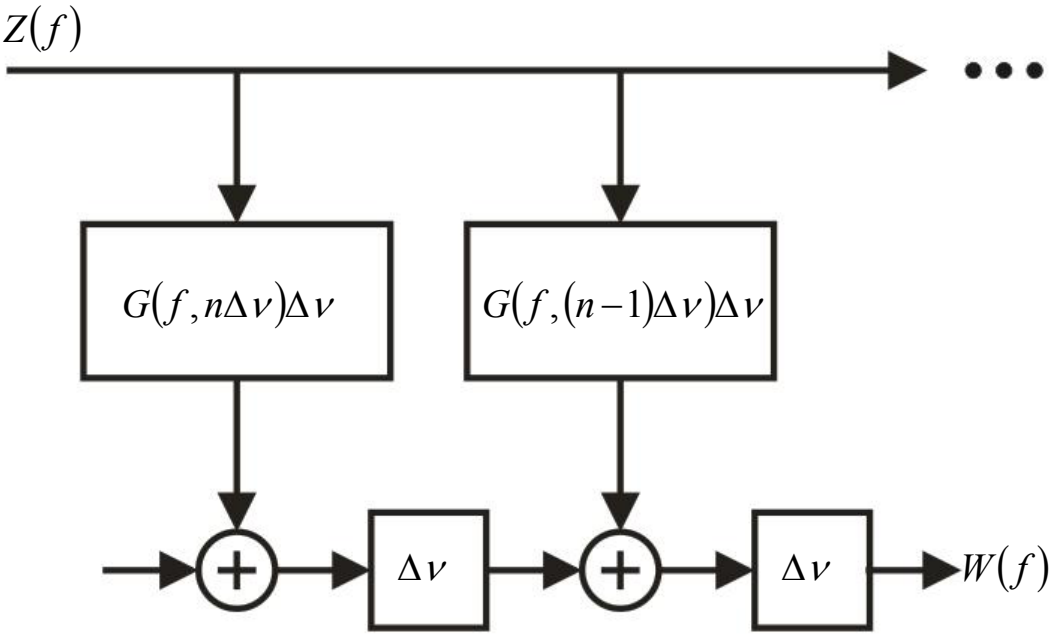

Figure 4.5: Frequency-conversion model for a multipath fading channel [56], [57].

The delay Doppler-spread function $U(\tau,\nu)$ represents a linear time-varying channel as a continuous array of delay elements, in the interval $(\tau, \tau + d\tau)$, on the input and Doppler-shifted elements, in the interval $(\nu, \nu + d\nu)$, on the output, with the differential scattering amplitude of $U(\tau,\nu)d\tau\, d\nu$ [56], [57]. Thus, a multipath channel with both delay scatterers and moving elements is best represented by $U(\tau,\nu)$. There are two I/O functions that use $U(\tau,\nu)$. These are given in [56], [57] as

$$w(t) = \iint z(t-\tau)e^{j2\pi\nu t}U(\tau,\nu)d\nu\, d\tau \tag{4.13}$$

and

$$W(f) = \iint Z(f-\nu)e^{-j2\pi\tau(f-\nu)}U(\tau,\nu)d\nu\, d\tau\,, \tag{4.14}$$

where (4.14) is obtained by performing a Fourier transform on both sides of (4.13) with respect to t.

The functions $T(f,t)$, $g(t,\tau)$, $G(f,\nu)$ and $U(\tau,\nu)$ are related to each other through various Fourier and inverse Fourier transforms. These relationships are illustrated in Figure 4.6.

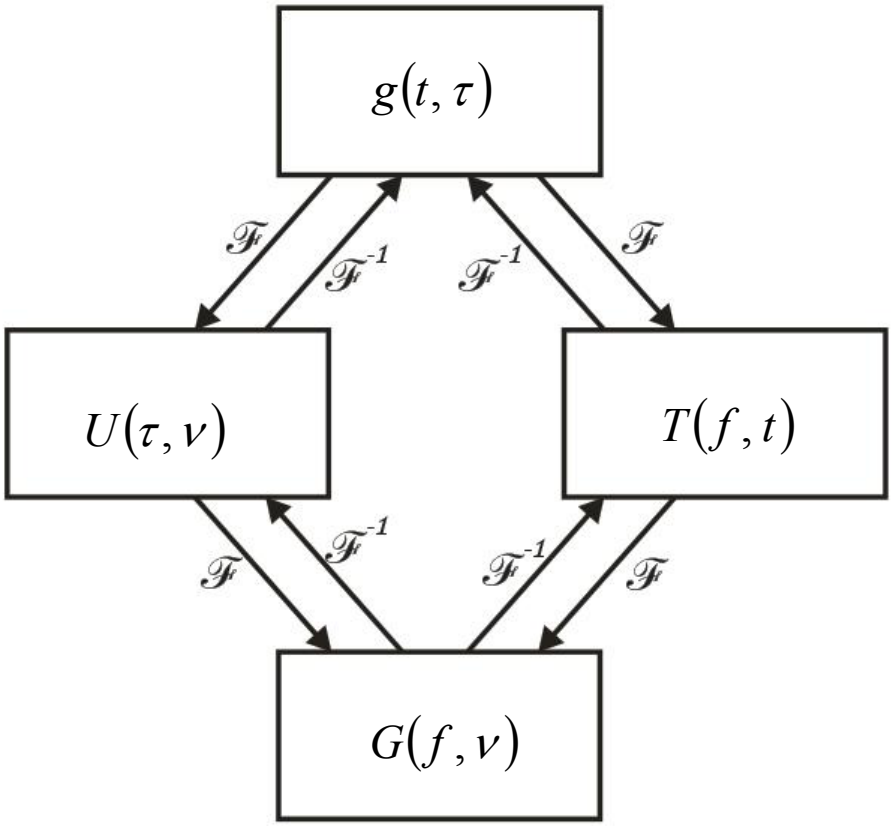

Figure 4.6: The four multipath models and their Fourier transformation relationships [56], [57].

4.3. Classic Multipath Models

In general, there are three ways to view multipath channels. The latter two of these use baseband models and assume the channel is narrowband and flat-fading. For the simplest case, a nonfading channel with added noise is described. This model, called Gauss, only includes the signal and noise. The second case involves modeling a channel with a dominant signal and several smaller signals and noise superimposed on it. This second approach is classically described by a Rice model. The third case involves modeling a channel with noise and many signal copies of equal amplitudes and equally distributed phases and angles of arrival with none dominant. The classical description for this approach is the Rayleigh model. Since these models describe first-order statistics, they are not expressed in terms of time or distance [47].

4.3.1. Gauss Model

This section summarizes the classical description of the nonfading model: the Gauss model. For the most part, there are three components included in the three classic nonfading and multipath models: a dominant signal, thermal noise power and multipath components [48]. The Gauss model does not include any multipath components. It is composed of the specular component with noise added [48], [58]. Variations of the dominant signal are due to the added noise power. The added thermal noise power is often approximated by additive white Gaussian noise (AWGN), which is flat over the whole frequency spectrum.

Multipath has distortion characteristics of delay and Doppler shift. Thus, noise is considered external to it. However, since noise is always present in multipath fading

environments, it is often referred to as Gauss fading [56]. This can mistakenly give the impression that a Gauss model is a multipath fading channel model. However, this is not the case.

The Gaussian PDF is of the form $e^{\frac{-x^2}{2\sigma^2}}$ [54]. Both Rayleigh and Rice, two other classical models for LTV channels, contain this Gaussian form in their PDFs [53]. Thus, the Gaussian PDF is a core element to these models.

The complete Gaussian PDF with zero mean is given in [54] as

$$PDF(x) = \frac{1}{\sigma\sqrt{2\pi}} e^{\frac{-x^2}{2\sigma^2}} \quad , \tag{4.8}$$

where x is the signal strength in voltage and σ is the standard deviation and σ^2 is the variance. Both σ and σ^2 are due to noise and represent the standard deviations and variance in the signal due to noise. Thus, the exponent of this PDF represents a signal-to-noise ratio, with x^2 being the signal power and σ^2 being the noise power. The PDF of the Gauss model has the distribution shown in Figure 4.7.

Figure 4.7 graphs the Gaussian PDF with three standard deviations: 0.5, 1 and 2. The peak is equal to $\frac{1}{\sigma\sqrt{2\pi}}$ and is, thus, higher for lower standard deviation values. The PDF when $x = \sigma$ is $\frac{1}{\sigma\sqrt{2\pi e}}$. The peak is located where the signal has the least deviation from its original state. Less noise indicates lower noise power, which would mean a lower standard deviation. This results in a higher peak and a higher SNR.

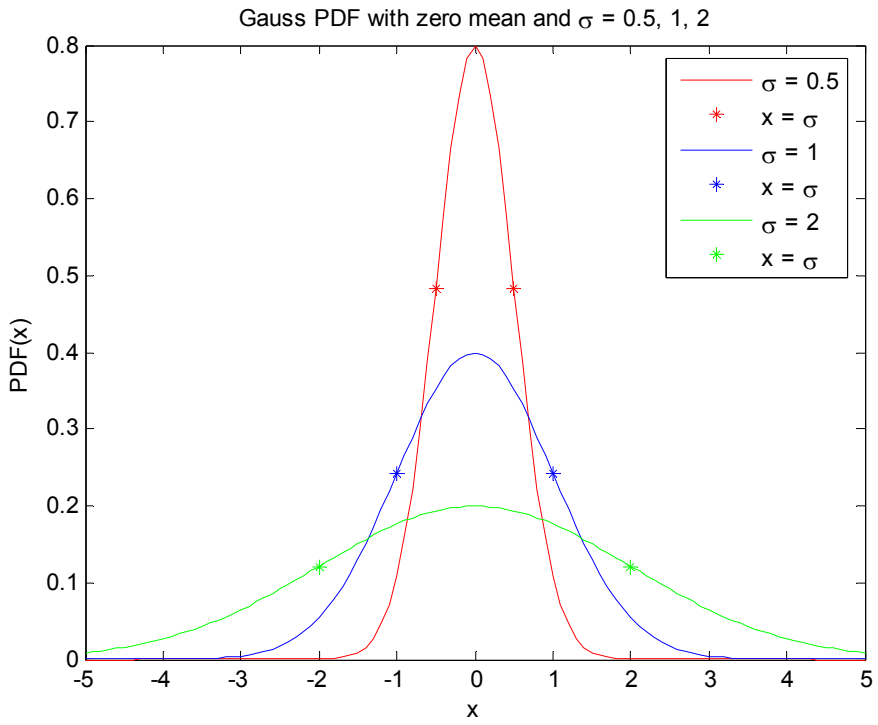

Figure 4.7: Gaussian PDF plotted versus *x* for three standard deviation values: 0.5 (red), 1 (blue) and 2 (green).

4.3.2. Rayleigh Fading

This section summarizes the first of the two baseband multipath models: the Rayleigh fading model. This model represents the worst-case multipath. It is where the line-of-sight (LOS) path is completely blocked, and there is no dominant signal at the receiver. The model represents the effects of multipath components with added noise on the in-phase and quadrature signal components [44], [48].

The Rayleigh channel is stochastic, and so it can also be represented by a PDF. Unlike the Gauss PDF that describes either the in-phase [$g_I(t)$] or the quadrature [$g_Q(t)$] signal component, the Rayleigh PDF takes into account the combined in-phase and quadrature components of the received signal. Each of these components is independent

and identically distributed (i.i.d.), and each is represented by the Gauss PDF shown in Section 4.3.1.

The derivation of the Rayleigh PDF is as follows [59]. In rectangular terms, the received signal is represented as $z = x + jy$, where $x = g_I(t)$ and $y = g_Q(t)$. In addition, p is used to represent the instantaneous received power. The probability that $|z|^2/2 < p$ is

$$F_p(p) = \frac{1}{2\pi\sigma^2} \iint_{x^2+y^2<2p} e^{-\frac{x^2+y^2}{2\sigma^2}} dxdy \,, \tag{4.15}$$

where the integrand is the Gauss PDF in terms of $|z|^2$.

The i.i.d. nature of the Rayleigh model indicates that the received signal is made up of several components all of equal amplitude, with phases equally distributed over $[-\pi, \pi)$ [44] and with equally distributed angles of arrival [45]. Thus, no signal is dominant, which is a worst-case situation for a single omnidirectional receiving antenna [58]. This assumption makes the PDF of the phases to be a constant $1/2\pi$ for all θ. Thus, the magnitude of the signal strength becomes the independent variable of the PDF, which allows an easy conversion of (4.15) to polar coordinates using $dxdy = \rho\, d\rho\, d\theta$:

$$F_p(p) = \frac{1}{2\pi\sigma^2} \int_0^{2\pi} d\theta \int_0^{\sqrt{2p}} \rho\, e^{-\rho^2/2\sigma^2} d\rho = \frac{1}{\sigma^2} \left[\sigma^2 e^{-\rho^2/2\sigma^2} \right]_0^{\sqrt{2p}} \,, \tag{4.16}$$

which simplifies to

$$F_p(p) = 1 - e^{-p/2\sigma^2} \quad . \tag{4.17}$$

Taking the derivative of (4.17), gives us the Rayleigh PDF in terms of power

$$f_p(p) = \frac{d}{dp} F_p(p) = \frac{1}{2\sigma^2} e^{-p/2\sigma^2} \quad . \tag{4.18}$$

Taking the derivative of $p = \rho^2/2$ to obtain $dp = \rho\, d\rho$, and the relation $\left| f_\rho(\rho) d\rho \right| = \left| f_p(p) dp \right|$ to convert from power to the composite signal amplitude, the Rayleigh PDF becomes

$$f_\rho(\rho) \left| d\rho \right| = \frac{1}{2\sigma^2} e^{-\rho^2/2\sigma^2} \rho \left| d\rho \right| , \tag{4.19}$$

which simplifies to the familiar Rayleigh PDF [54]

$$PDF(\rho) = f_\rho(\rho) = \frac{\rho}{2\sigma^2} e^{-\rho^2/2\sigma^2} \quad . \tag{4.20}$$

Figure 4.8 graphs the Rayleigh PDF for three standard deviations: 0.5, 1, and 2. The peak, which represents the best case for the received signal in a Rayleigh channel, is equal to $\frac{1}{\sigma} e^{1/2}$ and, as expected, is inversely proportional to the square root of the received noise power.

In physical terms, as the dominant signal goes through many reflections and scattering, it becomes weak relative to its multipath components. Its envelope approaches that of a Rayleigh envelope [45], and the signal fades occur rapidly and often deeply, depending on how the received signal vectors add together [47].

Figure 4.9 gives a plot of a signal with Rayleigh fading characteristics presented in [54]. Its similarity to fast fading, as shown in Figure 4.2, is why Rayleigh fading is in essence equated with fast fading [54].

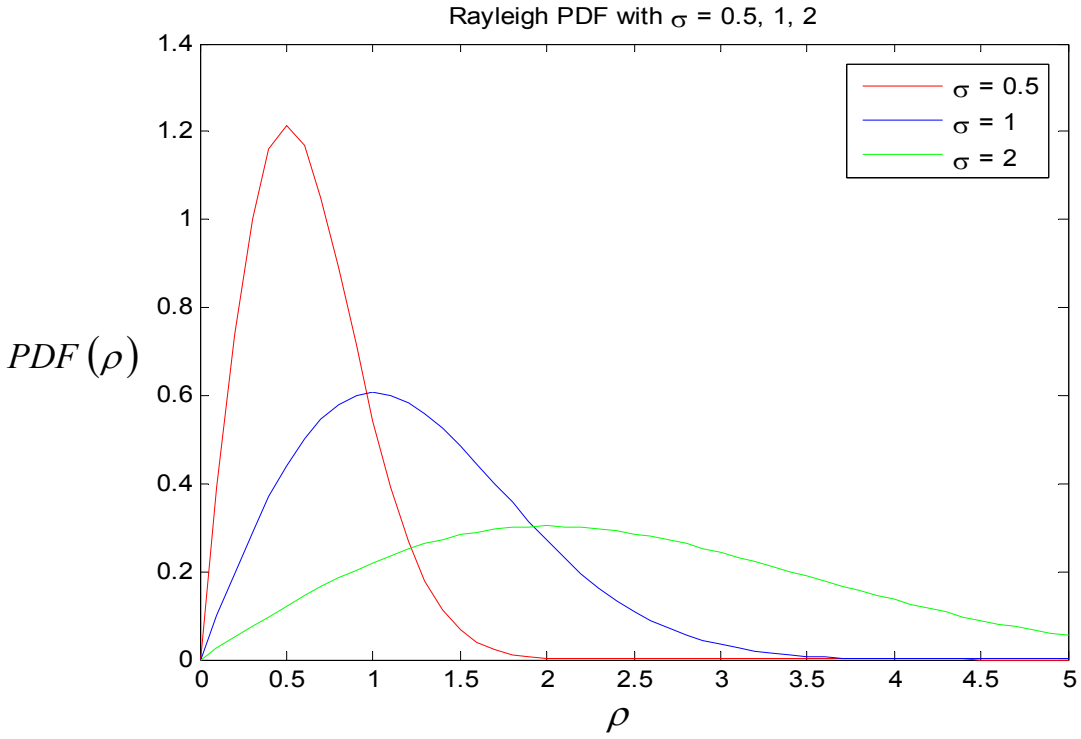

Figure 4.8: Rayleigh PDF plotted versus ρ for three standard deviation values: 0.5 (red), 1 (blue), and 2 (green).

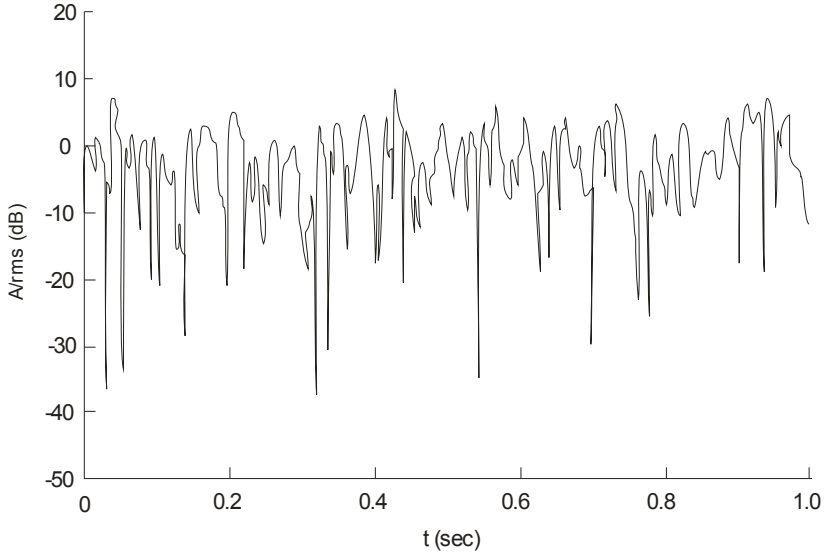

Figure 4.9: The Rayleigh signal fading for f = 900 MHz and for a vehicle speed of 120 km/hr (from [54]).

4.3.3. Rice Fading

This section summarizes the second classical baseband multipath model: the Rice fading model. The original and detailed treatment of this model is given in [60] and [61]. Graphically, Rice can be reduced to either the Gauss (with nonzero mean) or the Rayleigh model [47], [54]. Whereas the Rayleigh models equal amplitudes and equally-distributed phases arriving at the receiver from all directions, the Rice models the case where there is a specular component with interfering multipath signals, where the interfering signals only are assumed Rayleigh in nature [45]. In this case, the amplitude and phase of the specular component is dominant [47].

A key component in the Rice model is the signal-to-noise ratio (SNR) factor *K*, where the denominator includes both the multipath components and noise. This is similar to the way a sine wave (i.e., the dominant component) with random noise (i.e., smaller, scatter components) would be viewed [61]. This factor indicates that the specular element has *K* times as much power as the dispersed element.

Though the *K* factor is often viewed as a ratio of the LOS specular component to the multipath components at the receiver, it is in general the ratio of the dominant signal component at the receiver to the multipath, or scattered, signals that are less dominant plus noise [44], [45]. This latter allowance is important as there can be many cases where there is no LOS component between the transmitter and receiver, but there is still a dominant signal envelope that is received. Thus, *K* can be viewed as:

$$K = \frac{\text{line of sight}}{\text{multipath}} = \frac{\text{dominant spectral component}}{\text{multipath and thermal noise}} \quad . \tag{4.21}$$

When the *K* factor of the Rice PDF is zero, the Rice PDF reduces to the Rayleigh PDF. When the *K* factor approaches infinity, a Gauss PDF, resembling an impulse with a finite width and nonzero mean, becomes dominant, and the signal only experiences shallow fades [44]. This can be seen by examining the individual parts of the Rician PDF, given in [47], [54] as

$$PDF(\rho) = \frac{\rho}{\sigma^2} e^{\frac{-\rho^2}{2\sigma^2}} e^{-K} I_0\left(\frac{\rho}{\sigma}\sqrt{2K}\right), \tag{4.22}$$

where

$$K = \frac{A^2}{2\sigma^2} \ . \tag{4.23}$$

The two new terms, A and I_0, are the peak voltage of the envelope of the specular component and the modified Bessel function of the first kind and zeroth order, respectively.

These noise assumptions allow generalizations for the combination of noise and multipath components that allow their details to be ignored. Modern designs have to further define these generalized areas to exploit advantages available in them [58].

Due to the complexity of the Rice PDF, two plots were generated to help explain its characteristics. In Figure 4.10, the effect of various σ for the standard Ricean case are shown, where $K = 0$, and for a case where $K > 0$. There is a wider distribution as σ increases and the mean is at a higher value of ρ. Note that the distribution has a Gaussian appearance for $K > 0$. However, since the total received power is proportional to $A^2 + \sigma^2$, Figure 4.10 would imply that the overall power of the signal actually

changes. If the received power is made constant for some limited amount of time, it would imply that K and σ interrelate so that the area under the PDF is constant.

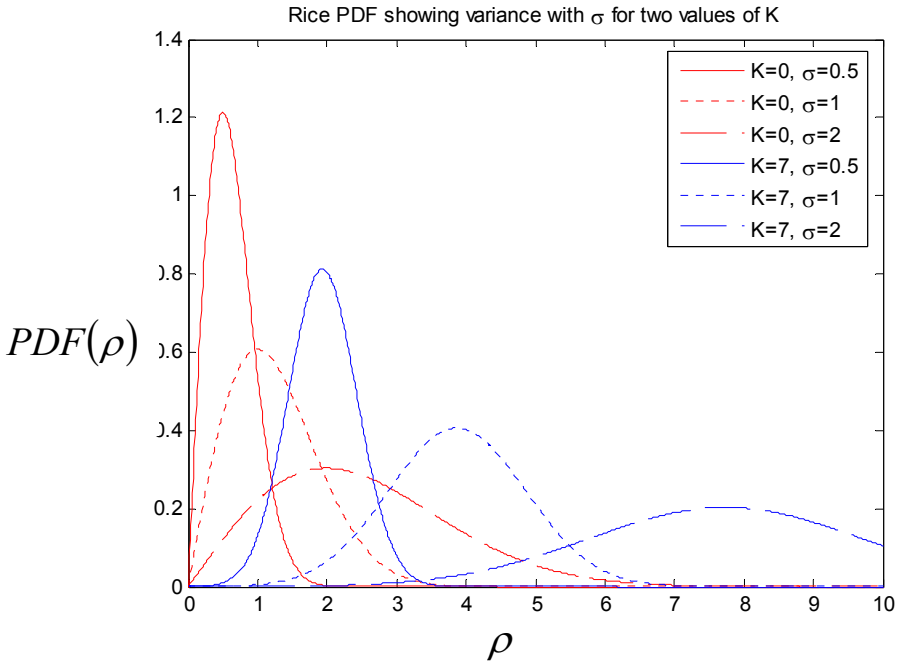

Figure 4.10: Rice PDF for two values of K and three values of σ.

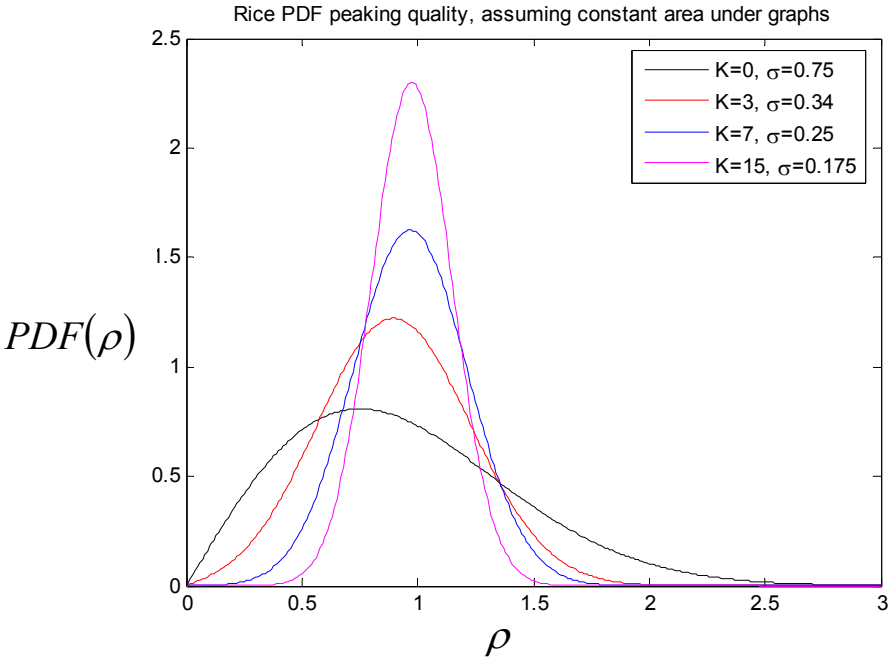

Figure 4.11: Rice PDF for various values of K (from [45]).

In [45], a Rice PDF is plotted with a constant area of 100. This is replicated in Figure 4.11. This plot shows that the Gauss PDF becomes dominant in the Rice distribution as K increases and becomes increasingly narrow (implying a reduced σ), resembling an impulse function. When a Rice PDF is graphed, the constant area assumption is commonly implied.

4.4. Other Narrowband Channel Models

Many newer narrowband channel models tend to be variations on the Rice model and try to have less simplifying assumptions. That is, they include more of the details that the previous models simply categorize as noise. For instance, a model by Clarke [47], [62] allows for two-dimensional analysis. It assumes the waves impinging on the antenna are all horizontal, making it a two-dimensional model. Since the dominant received waves are horizontal, this model explains nearly all the detectable characteristics of the signal envelope. Like Rayleigh, it assumes a uniform PDF for the phases of all signal copies, and it assumes all angles of arrival are equally probable.

Many newer narrowband models also include the Rayleigh distribution as a special case. An example of this is the Nakagami model, given in [47] as

$$PDF_m(\rho) = \frac{2}{\Gamma(m)}\left(\frac{m}{\Omega}\right)^m \rho^{2m-1} e^{\left(-\frac{m}{\Omega}\rho^2\right)} \qquad \rho \geq 0, \quad m \geq \frac{1}{2} \tag{4.13}$$

where ρ is the composite signal strength, m is a shape parameter and Ω $(=2\sigma^2)$ controls the spread. When $m=1$, the Nakagami PDF reduces to the Rayleigh distribution

$$PDF_1(\rho) = \frac{2\rho}{\Omega} e^{\left(-\frac{\rho^2}{\Omega}\right)} = \frac{\rho}{\sigma^2} e^{\left(-\frac{\rho^2}{2\sigma^2}\right)} \quad . \tag{4.14}$$

Thus, the value of m determines the relationship of the dominant signal to the scattered signals amidst fading. It also bears some resemblance to the Rician K factor, and the Nakagami PDF can be approximated by a Gaussian PDF with nonzero mean at higher values of m [44]. One advantage of this PDF over the Rician PDF is that, in the absence of the Bessel function, it is easier to acquire analytical solutions using the Nakagami distribution.

A good reference for understanding the complexity and trade-offs in channel modeling is [47].

4.5. Wideband

This chapter started by introducing the concept of multipath. Multipath affects signals through fading, path loss and shadowing. Conceptually, multipath can be represented as a collection of linear, time-varying filters. To further understand the relationship between diffuse components and the dominant component in multipath channels, three classic models for narrowband signals were discussed: Gauss, Rayleigh and Rice.

The signal of interest for this work, OFDM, is spectrally wideband. It occupies 16.6 MHz in the 802.11a Standard [63]. But each of its 52 subcarriers is narrowband. Each subcarrier occupies 312.5 kHz of bandwidth. This combination allows the signal to play to the strengths of both wideband (e.g., using diversity to avoid nulls) and the

strengths of narrowband (e.g., coherent bandwidth behavior within a subcarrier). It is thus helpful, even if on a high level, to understand some of the ways wideband differs from narrowband. Various approaches to OFDM channel modeling will also be presented.

A narrowband signal has a coherent or correlation[1] bandwidth [47]. A coherent bandwidth implies the spectral elements experience flat fading—that is, the same amount of attenuation and phase shift—across the entire signal bandwidth. It also means that the time period given by the inverse of the signal bandwidth far exceeds the time dispersion of the signal echoes [45].

For wideband, the bandwidth is extended such that it is wider than the coherence bandwidth. Thus, its inverse no longer exceeds the time dispersion of the signal echoes. The time delays, random attenuation and random phase shifts are no longer experienced uniformly across the band [45], [47]. One part of the band will experience more or less time delay, attenuation and phase shift than another. The fading is then dependent upon the location of the spectral component in the band and is thus frequency selective. Severe attenuation can occur as a null in a portion of the band even when the other spectral components experience relatively little attenuation.

The extension of a signal beyond its coherence bandwidth weakens the correlation between spectral components. As two spectral components, for example, move apart in frequency, their time delays, attenuation and phase shifts become increasingly uncorrelated [47]. As a result, the characteristics of each spectral component easily differ.

This lack of correlation increases the modeling complexity considerably and obtaining *a priori* knowledge of a channel becomes a significant challenge. Since this

[1] That is, the signals within the bandwidth are correlated. They become less so as they separate in frequency.

work compares different sets of measurements in the same channel, these effects do not have to be predicted but merely recognized. In other words, if two wideband signals are to be compared, they need to have shallow and deep attenuation in the same sections of their bands. This indicates that the channel characteristics have not changed, which allows the signals and their figures of merit to be compared directly. If the channel had changed, the resulting signals appear as uncorrelated when directly compared. To increase the correlation, the change in the channel would have to be modeled before the signals could be compared. By stabilizing the channel, this difficult task is avoided.

Where *a priori* knowledge of the channel is needed, the wideband channel must be modeled. A common approach to modeling a wideband channel is to model it as an array of narrowband subchannels [64]-[68]. With this approach, the modeler can often still use Gauss [65], Rayleigh [65], [66], [68] and Rice [66] as baselines for the new models and even as integral parts of them. For OFDM, which is a multicarrier system composed of an array of narrowband subcarriers, these narrowband subchannels are assumed to be uncorrelated to each other due to their orthogonality [64], [65]. Thus, modeling approach makes sense for OFDM. This approach can start to break down, due to ISI and other factors, as it approaches the length of the guard interval (that is, the cyclic prefix) of the OFDM signal.

Chapter 5: Accuracy in Multipath Measurements

5.1. Introduction

This chapter covers experimental work done on in-band distortion in lab and multipath environments. As in chapter 3, the use of frequency-domain techniques is explored. Instead of a two-tone signal, a 55-tone multisine was used for these experiments. The multisine is faster to measure than the two-tone and compares more directly to the digital signal. Using a multisine such as this extends the experimental capabilities to the large signal network analyzer (LSNA), such as that produced by Maury Microwave[2]. For the digital signal, an orthogonal frequency-division multiplexing (OFDM) signal was used instead of a CDMA signal. The multisine provides more insight into the characteristics of a measured channel than the OFDM signal alone. Since the

[2] www.maurymw.com

OFDM signal is made to mitigate—and thus mask—effects of multipath, it obscures the ability to characterize the channel. However, since the application is digital, a way is needed to compare the digital signal to the purely analog signal. What is needed is a figure of merit for the OFDM signal that has sufficient analog characteristics to be compared—even indirectly—to the multisine. This figure of merit is called error vector magnitude (EVM). This figure of merit allows the use of a very similar one for the multisine. Since it is calculated in much the same way, it is called the multisine error vector magnitude (MEVM).

This chapter is a follow-on to Chapter 4 and shows the differences when measuring in a time-varying environment (i.e., a constantly changing environment gives unrepeatable measurements) and a time-invariant environment. In the latter case, the environment in which the multipath measurements were taken is called quasi-time-invariant; whereas, the lab measurements could be taken as more truly time invariant.

It is interesting to note that both LTV and nonlinear time-invariant (NTI) environments produced in-band and out-of-band distortion. The out-of-band distortion appeared as spectral regrowth, and was viewed in terms of ACPR. The in-band distortion appeared as magnitude and phase variances in the transmitted signal and was quantified via EVM (digitally as bit error ratio (BER) or frame error ratio (FER)). In the NTI environment, these distortions occurred mainly from the nonlinearities of the power amplifier. In the LTV environment, the ACPR was generated by Doppler spread, and the EVM was worsened by both Doppler shifts and delay spreads. In the linear quasi-time-invariant (LQTI) environment in this work, nearly all moving objects were eliminated, and delay spread was the dominant distortion. In this case, two different OFDM

modulation types were compared, and an OFDM modulation type and a multisine were compared.

In Sections 5.2 and 5.3, OFDM and its figure of merit, EVM, are discussed. In Sections 5.4 and 5.5, the multisine and its figure of merit, MEVM, are covered. In Sections 5.6 and 5.7, the different aspects of measuring OFDM and multisine signals, respectively, are discussed. In Sections 5.8-5.10, measurement results taken in an LTI an LTV and an LQTI environment are discussed. In the LQTI environment, the environment is stable enough to compare the figures of merit for the OFDM signal and the multisine signal. The summary and conclusions are in Section 5.11.

5.2. Orthogonal Frequency Division Multiplexing

OFDM achieves a high data rate in a compact bandwidth. OFDM takes symbols at a high data rate, which on a single carrier would make the signal inherently wideband, and converts them into N parallel streams at a rate of $1/N$ that of the original stream. Lower data rate for each subcarrier means that each acts like it is going through its own narrowband channel. This allows each subcarrier to experience flat fading (i.e., the gain within each subcarrier does not vary with frequency) and thus avoid the frequency selectivity that would be an issue with the inherently wideband signal. Though this simplifies the receiver by eliminating the need for a sophisticated time-domain equalizer, it provides other challenges when deep fading obscures one or more subcarriers [55], [69]. Thus, all modern OFDM systems use coding, as shown in Figure 5.1 to allow the recovery of lost bits. The coder—or convolutional coder—maps each bit to two other bits, and then the interleaver spaces these bits far apart in the band [69]. This spacing of

the bits on widely-spaced carrier frequencies is commonly known as frequency diversity [46]. Combined, they make up a wide bandwidth. With frequency-division multiplexing (FDM), this type of strategy is not bandwidth efficient. However, using the inverse fast Fourier transform (IFFT) to map the symbols such that their subcarriers overlap and are orthogonal to each other reduces their bandwidth so that each subcarrier can be spaced just 312.5 kHz from its adjacent subcarriers [55], [69]. Just as the data rate is reduced by $1/N$, the time duration of the symbol, T_S, is increased by N to become NT_S [45]. This longer time duration, along with adding a guard interval, allow a considerable reduction in ISI due to the preceding burst [45]. The guard interval also aids with maintaining orthogonality among the subcarriers in the presence of fading due to time dispersion [55]. Orthogonality allows each received subcarrier to be easily distinguished from its neighboring subcarriers [55].

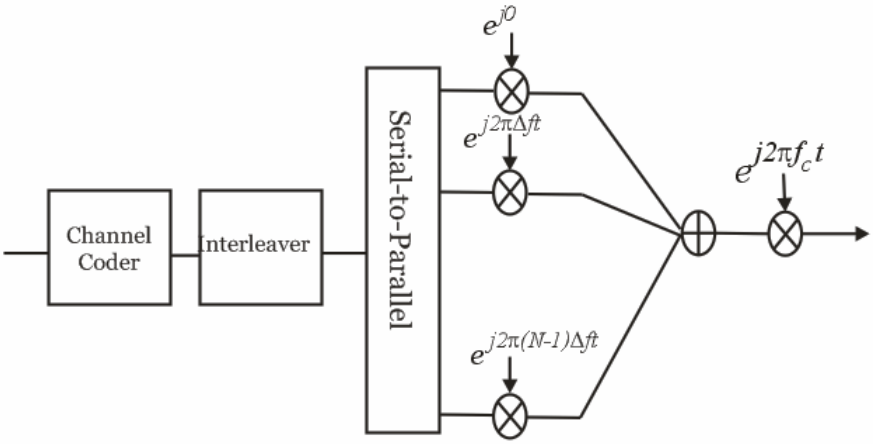

Figure 5.1: Coded OFDM transmitter, from [69].

A disadvantage is that OFDM gives a high peak-to-average power ratio (as high as N times the average) due to its subcarriers being individually modulated [69], [70].

This causes the power amplifiers of the transmitter to run in the less efficient back off region of operation.

A key to OFDM remaining orthogonal is to maintain strict timing requirements. The receiver must first detect the start of a burst, and then use the pilot subcarriers to estimate the amount of phase derotation for each data subcarrier [63]. The pilot subcarriers use the fixed modulation type binary phase-shift keying (BPSK) and have a known sequence and number of symbols. The receiver can then use its correlator to detect the pilot signal, perform the time synchronization using a known sequence and number of symbols. In addition, the cyclic prefix (CP) aids in reducing multipath echoes from the previous bursts. Then the receiver can calculate the variance and mean of the phase deviation in the frequency domain to derotate the symbol phases of the data subcarriers [71]. The pilot subcarriers help track systematic phase rotation. This allows the estimation of the systematic rotation of each data subcarrier so that they can be derotated and demodulated coherently [46].

OFDM was first introduced as an 802 standard via the 802.11a™-1999 Standard [63]. This standard specifies operation in the 5 GHz band. It is the place to start when studying 802 standards that specify OFDM. For instance, the 802.11g™-2003 Standard, which specifies wireless OFDM operation in the 2.4 GHz band, was written with the assumption that the reader was already well acquainted with the 802.11a Standard. Some specifications for the 802.11a Standard are shown in Table 5.1.

Table 5.1: 802.11a parameters, taken from [46], [63].

Parameter	Value
Bands of Operation	5.15-5.25, 5.25-5.35, 5.725-5.825 GHz
Data Rates	6, 9, 12, 18, 24, 36, 48, 54 Mbits/s
Subcarriers	52 (48 data, 4 pilot)
Modulation	BPSK, QPSK, 16-QAM, 64-QAM
Subcarrier Frequency Spacing	312.5 kHz (=20 MHz/64)
Sampling Rate	20 Msamples/s
Channel Spacing	20 MHz
Signal Bandwidth	16.6 MHz
IFFT/FFT period	3.2 μs
Guard Interval	800 ns
Symbol Interval	4.0 μs

5.3. Error Vector Magnitude

EVM is a common figure of merit for assessing the quality of digitally modulated telecommunication signals. EVM expresses the difference between the expected complex voltage value of a demodulated symbol and the value of the actual received symbol. While another common figure of merit, bit error rate, gives a "go," "no-go" level of system characterization, EVM can be more useful to the microwave engineer because it contains information about both amplitude and phase errors in the signal [63], [72]. This additional information can allow a more complete picture of the channel distortion and is more closely related to the physics of the system [71].

Because of the potential for the mixing of in-band frequency components, EVM is often used to characterize signals that use broadband schemes for transmitting large amounts of data at relatively high speeds. The most common of these schemes at 5 GHz is known as OFDM, as specified by the IEEE 802.11a^{TM}-1999 Standard [63]. OFDM is used in wireless local-area networks (WLANs), in the Dedicated Short-Range

Communication (DSRC) systems for tracking and observing loads in commercial vehicles [73], and in the recently opened public-safety band at 4.9 GHz [71].

The goal of OFDM transmission in the 802.11a Standard is to transmit a sequence of bits over the air. Thus, the transmission starts with a sequence of bits, and the final result of the received and demodulated OFDM signal at the other end is ideally that same sequence of bits. Before transmission, the bits are formed into symbols, which are modulated, transmitted, received and demodulated. Along with each symbol having a specific sequence of bits assigned to it, these symbols also have individual magnitudes and phases. For the quadrature phase-shift keying (QPSK) modulation case, the symbols can be mapped as a constellation diagram as shown in Figure 5.2.

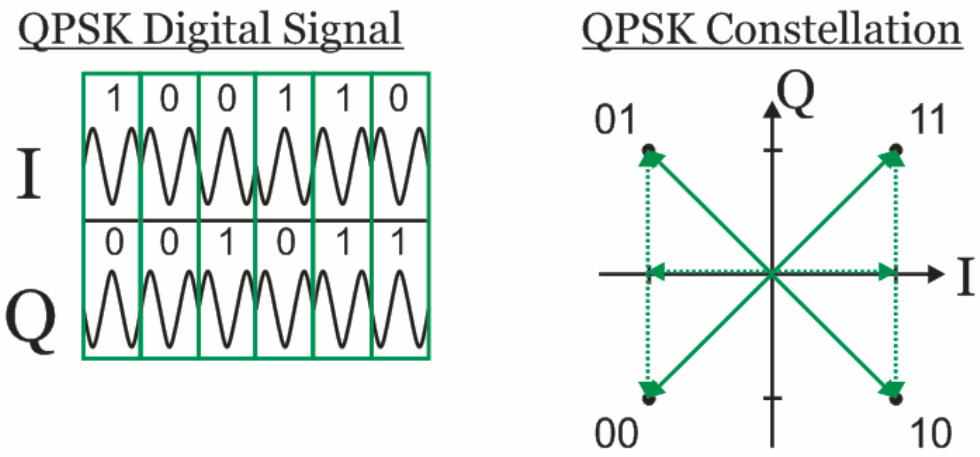

Figure 5.2: QPSK bits and constellation diagram.

To aid in visualizing demodulated signals, constellation diagrams are often used to represent digital bits in terms of symbols. In a sense, constellation diagrams are the bridge between digital and analog representations of a data stream. A constellation diagram is a plot of symbols where each symbol represents one or more bits (depending

on the modulation type)—the digital aspect. It is also a plot where each symbol is represented by a unique magnitude and phase—the analog aspect.

Bit or frame error rates (BER or FER) mark performance in purely digital terms. That is, they will only indicate if there is or is not a data error. They give no measure of the level of in-band degradation in a signal leading up to the onset of data errors. For this, an analog figure of merit is needed. Constellation diagrams, like Figure 5.2, illustrate that this type of figure of merit is possible for the OFDM signal. The diagram illustrates that each symbol has a unique magnitude and phase. The analog figure of merit specified in the 802.11a Standard is the EVM. For the case of a single received signal, this is merely the magnitude of the vector that stretches between the ideal symbol and the measured symbol. An example of this is given in Figure 5.3, which gives a zoomed in view of one quadrant of a 16-symbol quadrature amplitude modulation (16QAM) constellation diagram. The four locations where a symbol would ideally fall are shown by black dots. These ideal symbols are needed to be able to associate the measured symbols to the bit patterns they represent.

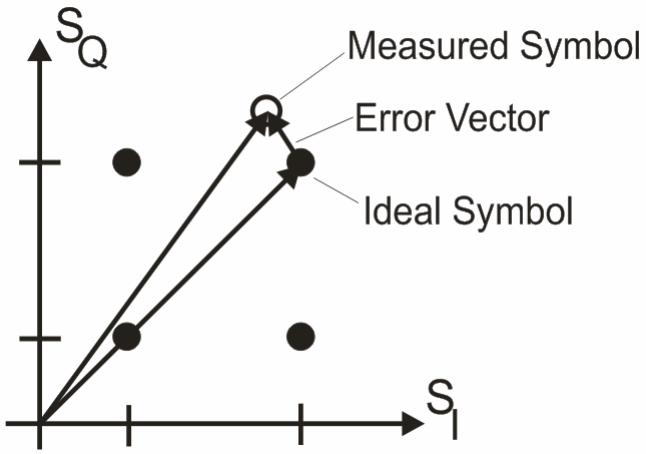

Figure 5.3: Upper right quadrant of a 16-QAM constellation diagram, taken from [63].

Said another way, EVM expresses the difference between a complex voltage value of a demodulated symbol and its expected value. Thus, EVM summarizes information about both amplitude and phase errors in the signal [63], which can give insight into the physical behavior of a channel. Furthermore, EVM, with mean-square normalization, for a given channel is independent of the modulation scheme used; whereas, FER varies with a change in modulation. Since different modulation schemes may be used within a burst, or between adjacent bursts [74], this motivates the use of normalization—implicit in the EVM equation of the IEEE 802.11a™-1999 Standard—to calculate EVM easily and to enable direct comparison of EVM for a given average power level per symbol between modulation types.

The IEEE 802.11a™-1999 Standard specifies use of several different OFDM modulation types (i.e., BPSK, QPSK, 16QAM, 64-symbol quadrature amplitude modulation (64QAM), etc.) that may be used in adjacent bursts. Even within one burst more than one modulation format may be used since the four pilot subcarriers are always transmitted using BPSK. This motivates the use of normalization, to calculate EVM easily and to enable direct comparison of EVM for a given average power level per symbol between modulation types. Such normalization is implicit in the IEEE 802.11a™-1999 Standard and was the focus of the work in [71].

The 802.11a Standard allows for two types of normalization. One type is to normalize all symbols so that the outermost ideal symbols each equal one. The second type is to normalize all symbols so that the mean-square value of the ideal constellation equals one. For most cases, the first method will give different EVM values for different modulation schemes even in the most ideal cases. As a general rule, the second method

will give a consistent EVM between modulation schemes.[3] Due to this ability to obtain the same EVMs for different modulation schemes, the second method of normalization is presented next [75].

Figure 5.4 shows three constellation diagrams for 16QAM, which has 16 symbols by which it modulates the RF carrier in both magnitude and phase. In each case, I / Q represent the in-phase (0° relative phase) and quadrature (90° relative phase) values of each symbol. Figure 5.4(a) represents a measured set of symbols in an I / Q voltage space (i.e., V_I / V_Q axes). Scattered dots on this diagram represent small errors in the measured symbols. Figure 5.4(b) represents the ideal constellation in a dimensionless I/Q integer space (i.e., C_I / C_Q axes). To calculate EVM, the diagrams in Figure 5.4(a) and (b) are scaled to form the normalized constellation diagram in Figure 5.4(c) with axes represented by S_I / S_Q.

To efficiently calculate EVM, the diagrams in Figures 5.4(a) and 5.4(b) are scaled to form the normalized (dimensionless) constellation diagram in Figure 5.4(c). The in-phase (S_I) and quadrature (S_Q) axes are similar to the real and imaginary axes used in complex voltage representations. A scaling for these constellations is derived in this section.

To enable normalization, a uniform distribution of the transmitted symbols on the constellation is assumed. Thus, the transmitted symbols have an equal probability of visiting each location on the constellation and the number of symbols transmitted is a multiple of the number of unique symbols in a constellation. Before normalization occurs it is assumed that the receiver has derotated the received symbols so that they are aligned

[3] In some cases, like when a PA is in compression, this may not hold.

in the constellation. Systematic rotation of symbols occurs, for example, when there is a difference between the sampling frequency (typically set by the center frequency) and that of a given subcarrier. Due to the commonality of the problem, all OFDM receivers have derotation operations built into their synchronization routines.

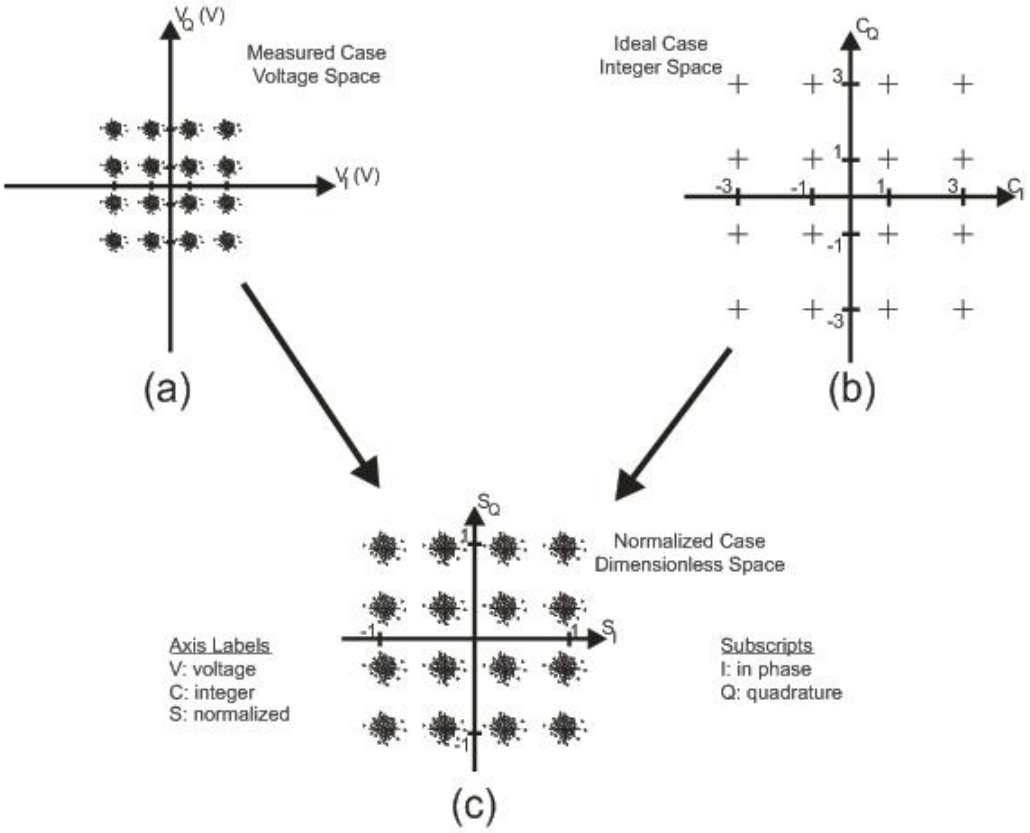

Figure 5.4: Graphs of (a) measured symbols, (b) the ideal constellation diagram, and (c) a normalized space that facilitates calculation of EVM.

The first step for symbol normalization is to obtain the ideal constellation diagram. This diagram shows the ideal placement of symbols at integer levels (e.g., Figure 5.4(b)). To obtain this diagram, start by calculating the number of levels along either axis (n) from the total number of symbols (N):

$$n = \sqrt{N} \quad . \tag{5.1}$$

The integer coordinates of for each symbol of Figure 5.4(b) are

$$C_{\text{ideal},pq} = C_{\text{I,ideal},pq} + jC_{\text{Q,ideal},pq} = (2p-1-n)+ j(2q-1-n), \qquad (5.2)$$

where the integers p and q satisfy $1 \le p \le n, 1 \le q \le n$, and n is defined in (5.1).

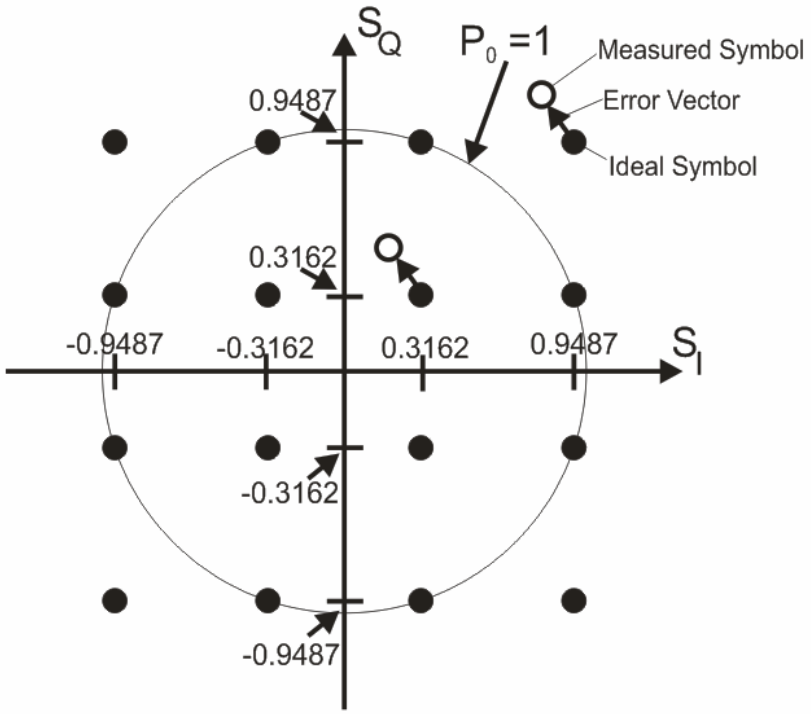

Figure 5.5: Normalized constellation diagram for 16QAM.

Figure 5.5 shows just the ideal 16QAM constellation, after normalization, with one measured symbol and its error vector. In this special case with only one measured symbol and with $P_0 = 1$, the magnitude of this small vector equals the EVM. If there were more symbols acquired than just this one, the EVM would equal the root-mean-

square (RMS) of all the error vectors and is often shown as a percent of the average power per symbol of the constellation.

As given in (2) of [76], EVM can be expressed mathematically as

$$EVM_{\text{RMS}} = \left[\frac{\frac{1}{N}\sum_{r=1}^{N} | S_{\text{ideal},r} - S_{\text{meas},r} |^2}{\frac{1}{N}\sum_{r=1}^{N} | S_{\text{ideal},r} |^2} \right]^{\frac{1}{2}}, \tag{5.3}$$

where $S_{\text{meas},r}$ and $S_{\text{ideal},r}$ are, respectively, the normalized measured and ideal r^{th} symbols, and N is the number of unique constellation symbols. To find this EVM, both ideal constellation symbols and arbitrary voltage values must be normalized and compared, as shown in Figure 5.4.

First, the power in each measured symbol, $P_{V,\text{symbol}}$, must be divided by the average symbol power calculated over all symbols in the constellation, to obtain $P_{S,\text{symbol}}$:

$$P_{\text{S,symbol}} = \frac{P_{\text{V,symbol}}}{P_{\text{V}} / T}, \tag{5.4}$$

where P_{V}, the total power of a measured constellation having T symbols, is

$$P_{\text{V}} = \sum_{r=1}^{T} \left[\left(V_{\text{I,meas},r} \right)^2 + \left(V_{\text{Q,meas},r} \right)^2 \right] \quad (\text{W}), \tag{5.5}$$

where $V_{\text{I or Q,meas},r}$ is the RMS voltage level of the in-phase and quadrature components of the measured symbols and T is typically >> N. From (5.4), it is seen that $P_{\text{S,symbol}}$, is dimensionless, and its overall average is one, as shown by P_0 in Figure 5.5.

To calculate EVM, the normalization factor $|A_{\text{meas}}|$ needs units of $1/V$. From (5.4),

$$|A_{\text{meas}}| = \sqrt{\frac{1}{P_{\text{V}}/T}} \ . \tag{5.6}$$

For the ideal case, the normalization is carried out in an integer space. Here N is used instead of T where N is the number of unique symbols in a constellation, and P_{C} is the sum of the squares of the amplitudes of all symbols:

$$P_{\text{C}} = \sum_{p=1}^{n}\left[\sum_{q=1}^{n}\left(C_{\text{I,ideal},pq}{}^{2} + C_{\text{Q,ideal},pq}{}^{2}\right)\right] . \tag{5.7}$$

Here, $C_{\text{I,ideal},pq}$ and $C_{\text{Q,ideal},pq}$ are, respectively, the real and imaginary integer values of each symbol and are defined by (5.2).

Similar to (5.6), the normalization scaling factor for ideal symbols, $|A_{\text{ideal}}|$, is written as

$$|A_{\text{ideal}}| = \sqrt{\frac{1}{P_{\text{C}}/N}} \ . \tag{5.8}$$

Using (5.6) and (5.8), the EVM is represented as

$$EVM_{\text{RMS}} = \left[\frac{\frac{1}{T}\sum_{r=1}^{T}\left(\left|\left(V_{\text{I,meas},r}\right)\cdot|A_{\text{meas}}| - \left(C_{\text{I,ideal},r}\right)\cdot|A_{\text{ideal}}|\right|^{2} + \left|\left(V_{\text{Q,meas},r}\right)\cdot|A_{\text{meas}}| - \left(C_{\text{Q,ideal},r}\right)\cdot|A_{\text{ideal}}|\right|^{2}\right)}{P_{\text{S,avg}}}\right]^{\frac{1}{2}} , \tag{5.9}$$

where

$$P_{\mathrm{S,avg}} = \frac{\left|A_{\mathrm{ideal}}\right|^2}{N}\left[\sum_{p=1}^{n}(2p-1-n)^2 + \sum_{q=1}^{n}(2q-1-n)^2\right]. \qquad (5.10)$$

In (5.10), $P_{\mathrm{S,avg}}$ is the mean-square amplitude of the symbols in the normalized constellation. It is always equal to one and is the same as P_0 in [63]. $V_{\mathrm{I\,or\,Q,meas},r}$ and $C_{\mathrm{I\,or\,Q,ideal},r}$ are, respectively, the unnormalized voltages and integer values for the r^{th} symbol for the measured and ideal in-phase and quadrature components. The limit T encompasses all measured symbols and satisfies the relation $T >> N$.

From the representation of (5.9), the expression for EVM in the 802.11a standard is easily derived. First, the normalized symbols must be identified in terms of I/Q to get

$$EVM_{\mathrm{RMS}} = \left[\frac{\frac{1}{T}\sum_{r=1}^{T}\left(|\,I_r - I_{0,r}\,|^2 + |\,Q_r - Q_{0,r}\,|^2\right)}{P_0}\right]^{\frac{1}{2}}, \qquad (5.11)$$

where $I_r = \left(V_{\mathrm{I,meas},r}\right)\cdot\left|A_{\mathrm{meas}}\right|$, $Q_r = \left(V_{\mathrm{Q,meas},r}\right)\cdot\left|A_{\mathrm{meas}}\right|$, $I_{0,r} = \left(C_{\mathrm{I,ideal},r}\right)\cdot\left|A_{\mathrm{ideal}}\right|$, and $Q_{0,r} = \left(C_{\mathrm{Q,ideal},r}\right)\cdot\left|A_{\mathrm{ideal}}\right|$.

After including some specifics of multiplexing types: the subcarriers (52 total), the number of symbols in a packet, L_{P}, and the number of frames, N_{f}, the 802.11a Standard equation is obtained, as given in [63].

$$EVM_{\mathrm{RMS}} = \frac{\sum_{i=1}^{N_f}\left[\frac{\sum_{j=1}^{L_P}\left\{\sum_{k=1}^{52}\left[\,|I(i,j,k)-I_0(i,j,k)|^2+|Q(i,j,k)-Q_0(i,j,k)|^2\right]\right\}}{52\cdot L_P\cdot P_0}\right]^{\frac{1}{2}}}{N_f} \tag{5.12}$$

With the normalization derived above applied in (5.12), EVM can be compared across subcarriers, packets and frames for bursts with different modulation types as long as the average power per symbol and the center frequency of the signal remain consistent. In Figure 5.6, this is illustrated graphically with two modulation schemes: QPSK and 16QAM. EVM is often shown in terms of the mean square value per symbol of the constellation, represented by these circles. When normalized, this mean square value is one. The ability to directly compare EVM for different modulation types is essential since the 802.11a Standard specifies use of BPSK modulation for the four pilot subcarriers, while the 48 remaining data subcarriers may use a different modulation scheme.

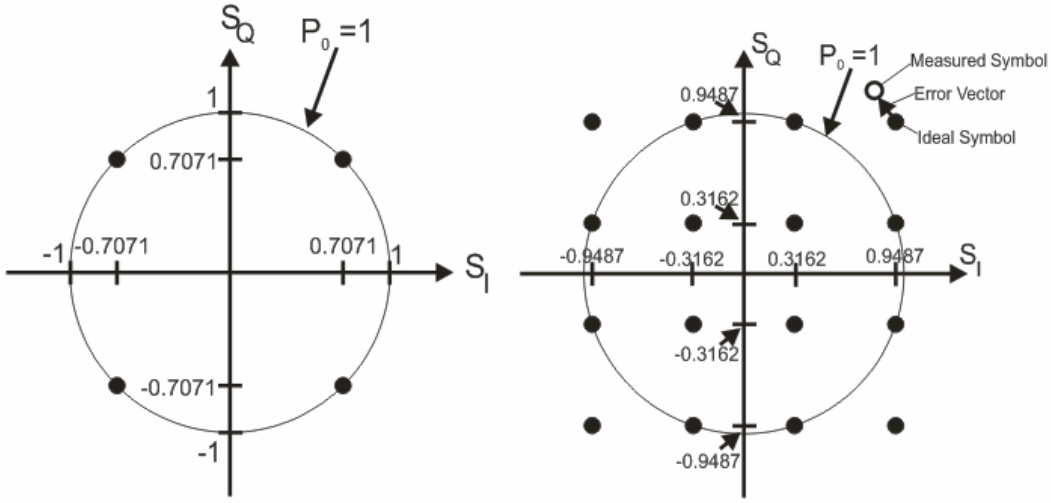

Figure 5.6: Normalized constellation diagrams for QPSK and 16QAM, from [63].

5.4. Multisine Generation

As discussed in Chapters 2 and 3, testing power amplifiers with two-tone signals is a common method. It is a natural extension to try expanding analysis of PAs to periodic signals with more than two tones, that is, multisine signals. Thus, it is no surprise that a large amount of work where multisine (i.e., deterministic/periodic) signals are substituted for digitally-modulated (i.e., random/stochastic) signals has been done in the nonlinear time-invariant test environment of the power amplifier. As an example, the algorithm used to generate a multisine with the same PDF as an OFDM signal was first developed by Schoukens [77] and then improved upon by Pedro and Carvalho [78]-[80]. All these works were in PA environments.

In [81], work that was also done in a PA environment, the author presented a method where the generation of a multisine that gives an accurate EVM and is less computationally intensive than the method by Pedro. However, the method in [81] requires accurate triggering and timing for it to work. The multipath environment did not allow this luxury. The Pedro method did not require the need for synchronization and triggering.

In [77], Schoukens generates a multisine that approximates another signal using spectral data and a crest factor reduction method. In [78], Pedro uses the amplitude-only information from the spectrum and the PDF to generate a multisine from a digitally-modulated reference signal. The result is that the PDF of the multisine matches, with some level of error, the PDF of the digitally-modulated signal (a.k.a., the noise sequence in [78]).

In [78], Pedro showed that the PDF of the input signal played an integral role in determining the output signal of a nonlinear memoryless system. In terms of power, the output power for the output signal is expressed as

$$P_{out} = E\left\{ y^2(s) \right\} = \int_{-\infty}^{\infty} f^2(x) pdf_x(x) dx \ . \tag{5.13}$$

The excitation PDF is given in (5.13) as $pdf_x(x)$, and the system response at instance s is $y(s) = f_{NL}[x(s), x(s-1), \ldots, x(s-Q+1)]$. As indicated, the output is dependent on a limited number of past input samples.

Although the multisine could be based on the range of immediate amplitude values covered by the digitally-modulated signal, it would be missing the significance, or weight, of each of these amplitude values. Using the PDF of the digitally-modulated signal when generating the multisine input signal, a multisine-plus-distortion output signal from the PA is obtained that closely resembles the digitally-modulated (plus distortion) output signal. It gives the probability that the signal will reach each instantaneous amplitude value. In other words, the instantaneous amplitude values become weighted by the PDF as opposed to each of the amplitude values having equal weight.

The algorithm used to extract a multisine that is statistically similar to an OFDM signal is laid out in [79]. In this algorithm, there are two variables that help reduce the error between the multisine PDF and the digitally-modulated signal PDF: the number of tones used to make up the multisine and the number of iterations the algorithm is run. Up to a point, more tones and iterations lower the error but increase the computation time. The goal is to find the best approximation of the noisy signal given a reasonable number

of tones in the multisine. Sharing approximately the same PDF allows these two dissimilar excitations (i.e., stochastic versus deterministic) to act the same [80].

The algorithm used is [79]:

1. Specify a PDF and then generate a noisy signal in the time domain that adheres to it. Convert this signal to a PDF, or referred to here as the PDF domain, by rearranging the amplitudes at each time instance descending order.

2. Decide on a number of tones for the multisine and generate them such that they all have equal amplitudes.

3. In the time domain, generate this multisine. Convert this signal to the PDF domain by rearranging its amplitudes at each time instance such that they are now in descending order. This gives the PDF of the multisine.

4. In the PDF domain, swap the noisy amplitudes for the multisine amplitudes.

5. Recalling the time sample positions of the bins in the multisine, reorder the noisy amplitudes in the PDF domain of the multisine back to the time domain of the multisine. This makes a new multisine.

6. Convert the multisine to the frequency domain using the DFT and then level the amplitudes until the power equals the original total power level setting. The phases will stay the same.

7. Since this power leveling changes the PDF, check the level of error between the PDF of the leveled multisine and the PDF of the noisy signal. If the error is too high, go back through steps 1-6 starting with the multisine generated in step 6.

In the end, a multisine that varies in both amplitude and phase is generated. Mathematically, it is simply

$$x(t) = \sum_{k=-(N-1)/2}^{(N-1)/2} A_k \sin\left(\left(k\omega_{os} + \omega_c\right)t + \phi_k\right) \quad , \tag{5.14}$$

where N is the total number of tones in the multisine, A_k is the amplitude of each tone, ω_{os} is the frequency spacing between each tone and $k\omega_{os}$ gives the specific offset location of each tone, ω_c is the center frequency, and ϕ_k is each tone's unique phase.

In this work, a 55-tone multisine was used. The 55-tone multisine was able to give a multisine PDF with a minimum error level of $x = 3.243x10^{-13}$ from the OFDM PDF signal after the first pass.

5.5. Multisine Error Vector Magnitude

The goal in generating a multisine that was statistically-similar to an OFDM signal was to be able to compare the two signals directly in a multipath channel. Since the phases of the multisine components can be derotated [82] similar to the derotation of symbols in OFDM, and the tone amplitudes can be normalized just like the symbols in OFDM, an error vector magnitude can be calculated for the multisine signal. Due to its similarity, this new figure of merit is called multisine error vector magnitude (MEVM).

The constellation diagram for the multisine will not look like a neat grid, as it would with 16-QAM or QPSK. Its ideal values, which depend on the initial magnitude and phase settings of the multisine, will vary all over the diagram, as shown in Figure 5.7.

Since MEVM is calculated in the same way as EVM, the steps will not be reviewed in this section. However, this section will highlight the need for a scaling factor in MEVM to be able to accurately compare it to EVM. MEVM is related to EVM by a scalar. Mathematically, this is simply

$$MEVM = \frac{MEVM_{\text{meas}}}{N} = EVM \ . \tag{5.15}$$

This scaling factor is dependent upon the environment in which the multisine and OFDM signals propagate. It appears to have some similarity with the K factor in the

Rician propagation model. That is, with a more ideal propagation environment, a higher value of N is obtained. Similarly, a less ideal propagation environment gives a lower value of N.

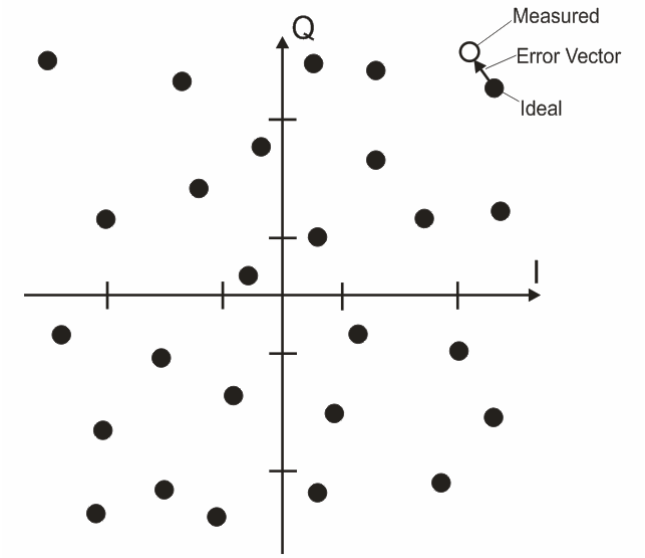

Figure 5.7: Example of the ideal constellation diagram for a multisine.

For narrowband signals, just about every multipath environment can be described by what is called a Rician distribution, of which the Rayleigh and (nonzero-mean) Gauss can be considered as special cases. Rician distributions have a *K* factor, which indicates if there is a specular signal and how dominant it is. A higher *K* indicates a more ideal environment, which results in a strongly dominant signal. A lower *K* indicates a more scattered environment, which results in a weakly dominant, to no dominant, signal.

The multipath measurements were done with a directional antenna, which was rotated through 360 degrees. Some LOS measurements were also taken. It was found that there is not a one-size-fits-all N for those different situations with which the MEVM data could be scaled to get it to line up with the EVM data. The environment had to be taken into account. Thus, it was found that the line-of-sight measurement required a

higher N, just at it would require a higher K to describe it in Rician terms. As the environment became more scattered, the value of N required to line MEVM points up with EVM points became lower, similar to how the Rician K would also become lower.

Why is there a difference between the EVM and MEVM? OFDM signals have functions built into them to mitigate the effects of multipath. Two of its prominent functions are its convolutional coder and its cyclic prefix. The convolutional coder allows symbols to be duplicated and then spaced far apart in frequency within its transmission bandwidth. Thus, in the case of one being obscured in a null, the receiver can throw out the bad symbol and just keep the good one. The cyclic prefix allows time for the previous burst to fade before beginning the data for the next burst. This greatly reduces ISI. Thus, up until the receiver can no longer discern symbol locations, this will give a more ideal result for EVM. The multisine is a continuous signal and has no cyclic prefix or duplicate tones. Thus, it would by nature give a different value for MEVM than the OFDM signal would for EVM.

Due to its lack of cyclic prefix and duplicate symbols, the multisine would be a better symbol in the end for measuring multipath effects. Its behavior could more easily be related to the Rician model. Since the MEVM is inversely related to the signal-to-noise (and multipath) ratio, it is inversely related to *K*. Even though EVM is similarly related to the SNR, the cyclic prefix in OFDM allows it to practically eliminate ISI from the denominator in many cases [83], [84]. Thus, it only includes noise and co-channel interference (CCI), along with the dominant component, in its *K*. Thus, though *N* does not directly relate to *K*, it would very possibly relate to the ratio of the *K* given by OFDM and the *K* given by the multisine.

5.6. Measuring OFDM Signals

Broadband digital measurements are readily performed on a vector signal analyzer (VSA), real-time analyzer or other instrument that captures a time record and internally performs a fast Fourier transform (FFT) to enable frequency-domain analysis [85]. This time-domain capture also allows the VSA to obtain phase information on the signal. After downconversion, the VSA, with special interpretive software (89601A in this case), demodulates the signal and calculates its EVM.

OFDM signals are digitally-modulated, bursted signals. As such, they are aperiodic, which leads to inherent discontinuities. These discontinuities in the captured time-domain record will lead to spectral leakage (or smearing) after the signal has been transformed by the FFT into the frequency domain. Though the receiver can be set for a periodic signal such that it receives an integer number of envelope cycles, this is not possible for it to do with any current digitally-modulated signal. Because of this, the receiver must have some type of windowing in the time domain to force continuity at the ends of the time-captured signal by forcing both ends toward zero. This can be set by the user on the Agilent 89640 VSA, though the filter is set automatically to FlatTop, which is optimized for amplitude accuracy, when measuring using the B7R option of this VSA.

Besides windowing, the most important user setting on the VSA is the attenuation leading into the analog-to-digital converters (ADCs). On the Agilent 89640 VSA, this setting is called the Range. More generally, it can be called the ADC amplitude resolution (AR) setting. Since it controls the attenuation of the signal arriving at the ADCs, this setting controls the resolution with which the amplitude of the signal is sampled. This is illustrated in Figure 5.8.

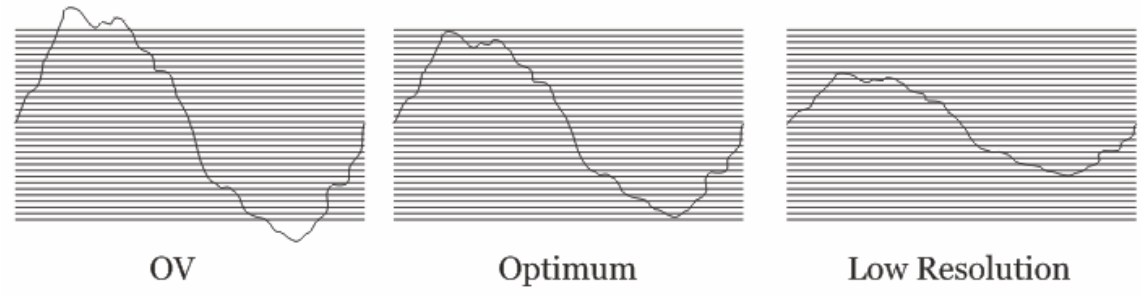

Figure 5.8: Three cases of AR: clipping due to over voltage (OV), optimum accuracy and low resolution from setting attenuation too high.

The AR also has a significant effect on the EVM. This is illustrated in Figure 5.9(a). There are three regions for the AR. First is the overvoltage condition, where the magnitude of a signal is too great for the ADC input. This results in a warning from the instrument and an invalid EVM altogether. This condition is shown as OV in Figure 5.9(a). Second is the optimal condition, where the signal amplitude is set within the upper and lower limits of the ADC input. Figure 5.9(a) shows this stage as having the lowest EVM, and it may be noted that this is only just above the last OV condition. Third is the low resolution condition, where an increase in error—and, hence, EVM—results since the amplitude of the signal is well within the upper and lower bounds of the ADC input. This results in a coarser stepping for the digitized amplitude of the signal. As the attenuation of the input signal increases, resulting in coarser amplitude stepping, the EVM increases, as shown in Figure 5.9(a) in the "increase in error" section.

Another factor to consider when measuring OFDM signals is the distortion added by the measurement equipment itself. EVM is a function of the entire system. Even with the simplest set-up, where the VSG is attached by a coaxial cable to the VSA, the EVM level can be changed by merely changing the output power of the VSG. This is illustrated in Figure 5.9(b). This figure shows a definite sweet spot—where EVM is lowest—in its

power output. At the high power end, the VSG is distorting. At the low end, the EVM is affected by noise. Only in the sweet spot is the VSG/VSA combination able to fall within the manufacturer's specification for EVM of <1%. Thus, great care must be taken in measuring EVM as it is a function of the transmitter, channel and receiver. Figure 5.10 shows how AR affects a constellation diagram.

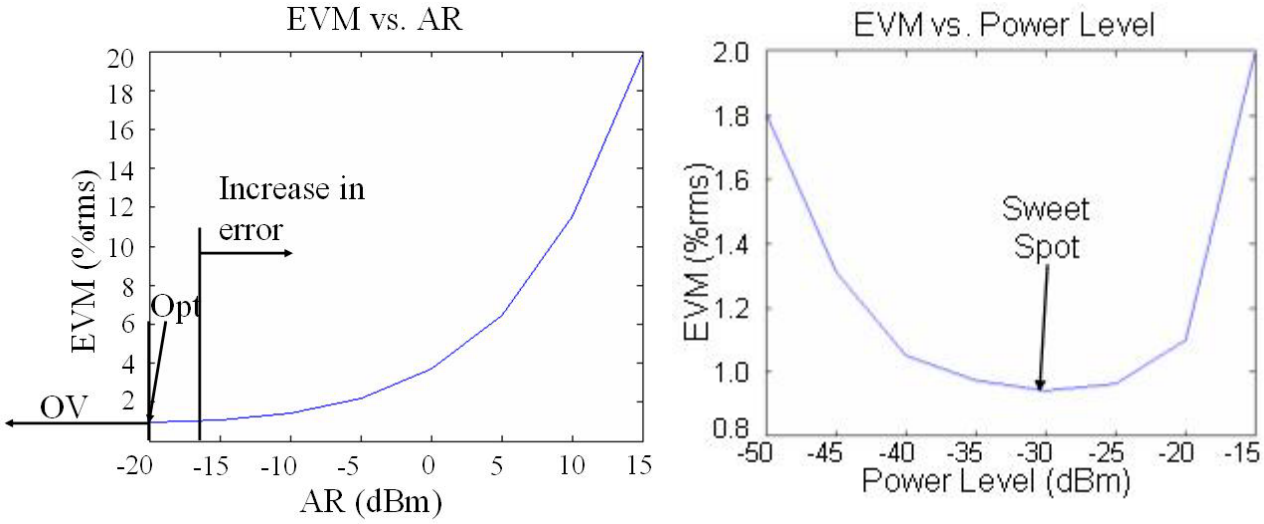

Figure 5.9: (a) EVM vs. AR with the VSG OFDM output power set to -30 dBm. (b) EVM vs. VSG power level. The AR is set optimally for each EVM calculation.

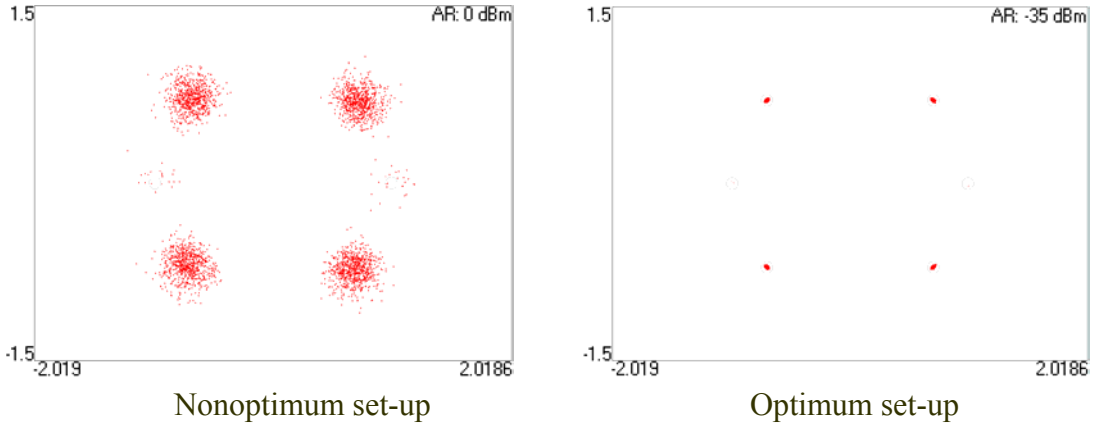

Figure 5.10: The effect of AR on QPSK constellation diagrams.

5.7. Measuring Multisine Signals

The VSA has several measurement advantages over a spectrum analyzer when acquiring bandpass RF signals. These include its time-domain capture, which enables measurement of magnitude and phase information, and its ability to display data in both time and frequency [86], [87]. The highly sampled, downconverted waveform gives a good amount of spectral detail around the carrier frequency. However, the resolution of the frequency spectrum is affected by the relation of the length of the time capture to the envelope period of the bandpass signal for periodic signals like multisines [88]-[90].

This section presents a procedure for optimizing VSA[4] measurements of periodic signals to minimize spectral leakage. The underlying principle of this method has been known for years [90], but it finds new application with the recent emphasis on the use of periodic, well-behaved signals to characterize complicated wireless devices, systems and channels [79], [91]. In these situations, multisines—test signals consisting of a collection of sine waves at frequencies that are slightly offset from each other—may be used to emulate digital test signals. In these test environments, where complete knowledge of the stimulus is known, it becomes practical to use this type of measurement method.

This procedure determines the proper VSA settings such that the VSA will obtain an integer multiple of the envelope period of the measured signal, as illustrated in Figure 5.11. Specifying an integer multiple of periods preserves an undistorted time-domain signal. Thus, the FFT used by the VSA will portray the frequency-domain characteristics of the signal with minimal distortion as well. This method also negates the need for time-domain filtering (windowing) for periodic signals, which is one method for improving the

[4] The Agilent 89640 VSA was used for these experiments.

spectrum when a fraction of an envelope period is present at the input, as discussed in [92]. Eliminating filtering removes one more potential source of distortion in the measurement and is useful when looking for a weak adjacent tone or distortion product.

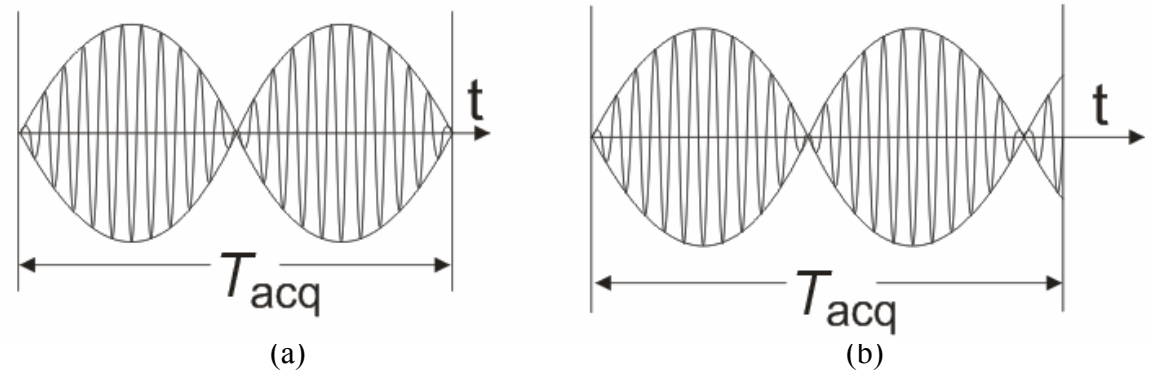

Figure 5.11: A two-tone multisine in the time domain, where (a) shows an integer multiple of acquired envelopes and (b) shows a fraction of an envelope being acquired on the end.

First, this procedure covers FFT considerations. The beauty of this procedure is in its simplicity. Though the VSA has many advanced features, such as filters, which ensure amplitude accuracy and help reduce side lobes on the acquired signals, and modulation/demodulation functions to interpret digital signals, this procedure only uses the digitized RF signal and the FFT function of the VSA, as in Figure 5.12.

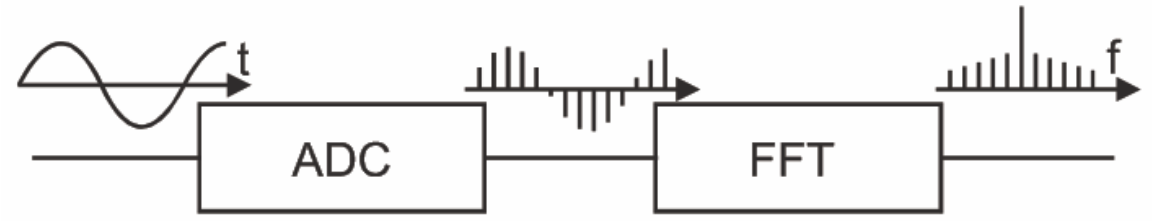

Figure 5.12: Sine wave incident on ADC and FFT of VSA. The frequency domain shows spectral leakage.

The FFT in the VSA is integral for transforming the acquired time record to the frequency domain. It is an efficient algorithm for calculating the discrete Fourier transform (DFT) by significantly decreasing the quantity of calculations, from $2N^2$ to $2N\log_2(N)$, for N points in a sequence [89], [93]. The FFT algorithm essentially replicates the captured section of the time-domain signal applied to its input such that it is periodic for all time. For modulated RF signals, if the FFT input does not have an integer number of time-domain envelope cycles, there will be a discontinuity on the input to the FFT, which results in finite amounts of power being spread over multiple frequency bins in the spectrum, as shown in Figure 5.12. This spreading decays around a given spectral peak as $1/f^n$, where the degree n is related to the smoothness of the function in the time domain (i.e., n is higher for a smoother function than for one with sharp discontinuities). Superimposed on this decaying function is a sinc function, due to discretization. This smearing of the spectrum is often called spectral leakage [89], [90], [92].

There are four VSA parameters that ensure the periodicity of the time-domain input to the FFT (called "self windowing" in [92]): number of acquired frequency bins, frequency span, resolution bandwidth (RBW) and the length of the acquired time window [94]. The effect of these parameters on the FFT in a VSA will be demonstrated using a five-component multisine $m(t)$, shown mathematically in (5.16).[5]

$$m(t) = \sum_{i=1}^{NS} A_i \cos(\omega_i t + \phi) \tag{5.16}$$

The first parameter considered is the number of frequency bins to use in this VSA measurement. The VSA takes a time-based measurement and then performs an FFT to

[5] Though applied to VSAs in this work, these principles are true for any FFT calculation.

obtain the signal's spectrum. The FFT runs fastest if the actual number of calculated frequency bins is a power of two (e.g., 64, 128, etc.), as discussed in [85], [88], [95][6].

The second parameter considered is the frequency span. The frequency span, the RBW and the time window are all interrelated, and, in this method, a change in one parameter will force a change in one of the other parameters. An approximate value for the frequency span is decided first to ensure the frequency band of interest will be captured in this measurement. However, the time window capture length and the RBW must still be taken into account before settling on the final frequency span that minimizes spectral leakage.

The third parameter, the RBW, sets the spacing between frequency bins when no windowing is applied [96]. In this case, RBW is the inverse of the time window, is proportional to the span and is inversely proportional to the number of frequency bins the VSA is set to calculate.

The fourth parameter is the time window. This sets the time capture length so the VSA either obtains an integer or fractional number of envelope periods for each acquired signal. Thus, the time window determines whether the signal acquired by the FFT is smoothly periodic or has discontinuities.

Figure 5.13 shows the lab set-up used for the five-component multisine. The multisine was centered at 1 GHz and the sine waves were spaced 1 MHz apart. This multisine clearly shows the effects of the VSA parameter settings on the spectral leakage. A VSG creates the five-component multisine, where the components have equal amplitudes and zero-degree relative phases. For the measurement examples shown in this

[6] The number of frequency bins displayed on the analyzer usually does not equal the number of bins calculated. For the calculations shown here, the number of bins actually acquired must be used.

section, the output power of the signal generator was –10 dBm. Figure 5.14(a) shows a measurement of the signal generator output taken without optimized VSA settings. The skirts around each tone demonstrate the spectral leakage referred to earlier. This spectral smearing can cause amplitude and phase errors in the measurement particularly for weak signal components. To make accurate measurements without filtering, it is essential that these five sine waves fall directly on five of the measurement window's frequency bins after the FFT is performed. Otherwise, the VSA calculates amplitudes and phases inaccurately.

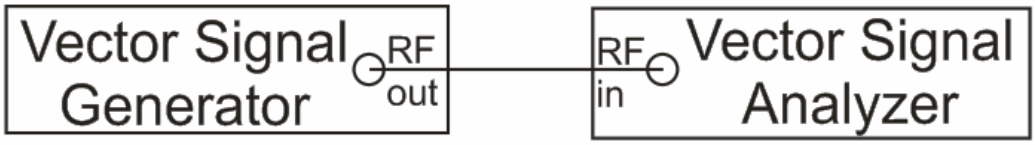

Figure 5.13: A basic diagram of the test setup.

To eliminate spectral leakage and obtain a clean spectrum, the four key parameters mentioned above—frequency bins, frequency span, RBW and time window—must all interrelate properly. Since this procedure requires maximum flexibility in setting these parameters, it requires some adjustments to the VSA's default settings. First, the RBW must be set to change independently from the span. Second, to have maximum flexibility in setting the RBW, the VSA must be enabled to allow a user-defined RBW to be specified. Third, all windowing filters must be disabled. This allows the direct FFT result to be clearly seen. Fourth, set the number of frequency bins. For the example shown in Figure 5.14, the maximum of 131,072 frequency bins was used, which lowered the spectral floor and showed the most detail.

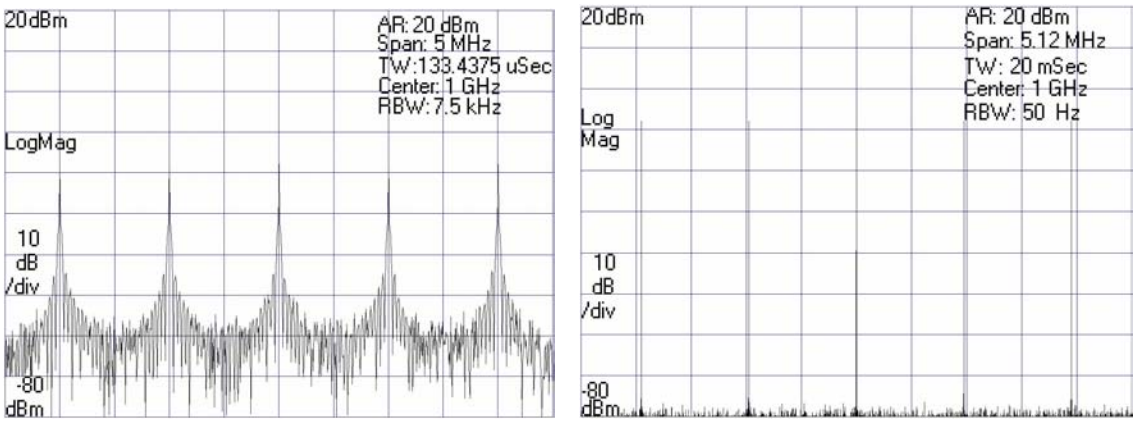

(a) (b)

Figure 5.14: VSA spectral plot of a five-component multisine. The spectral leakage shown in (a) has been minimized in (b). The center frequency is 1 GHz, and the spacing between the tones is 1 MHz. Frequency is shown in the x-axis, and the magnitude of the received signal in dBm is shown on the y-axis. AR is the amplitude resolution of ADCs. Number of FFT bins is 131,072.

The next step is to choose an approximate frequency span ($Span_{\text{approx}}$) that will display the spectrum of interest. For this example, 5 MHz was chosen. Using $Span_{\text{approx}}$ and the number of frequency bins (N), the time window (TW_{approx}) was calculated as 26.2144 ms by the relation

$$TW_{\text{approx}} = \frac{N}{Span_{\text{approx}}} \ . \tag{5.17}$$

Choosing a span in this fashion without considering the RBW and TW will often result in a noninteger number of time-domain cycles on the input, which leads to spectral leakage. The time window needs to equal an integer number of the signal-envelope periods to avoid truncation errors caused by the periodic nature of the FFT. As a result, the TW_{approx} value needs to be refined. For multisines with equally spaced frequency

components, the envelope period can be found by taking the inverse of the frequency spacing between adjacent sine waves (Δf) within the multisine being measured.

This inverse gets multiplied by the largest value of M that satisfies these equations:

$$TW_{\text{opt}} = M\left(\frac{1}{\Delta f}\right) \le TW_{\text{approx}} \ , \tag{5.18a}$$

$$TW_{\text{opt}} \approx TW_{\text{approx}} \ . \tag{5.18b}$$

A high M ensures an integer number of periods are acquired without the need for phase locking or triggering. Using $\Delta f = 1$ MHz, the integer $M = 20{,}000$ was found to give an optimized span of 6.5536 MHz[7], which satisfied the following equation:

$$Span_{\text{opt}} = \frac{N}{TW_{\text{opt}}} . \tag{5.19}$$

The inverse of the optimum time window gives the optimum RBW. The VSA can now be set to these optimized Span/RBW/TW settings. Since the results are optimal when rounding is minimized for each setting, it is important to specify as many digits as possible. Note how the skirts around each sine wave vanished in Figure 5.14(b). This clean spectrum indicates that the FFT has obtained a periodic input with no discontinuities. This corresponds to an integer number of envelope cycles in this case.

This method works for any number of 2^X frequency bins. In all cases, the key is to ensure the length of the acquisition time window is set to an integer multiple of $1/\Delta f$.

[7] The acquired span of 6.5536 MHz is equivalent to the displayed span of 5.12 MHz (or 6.5536 MHz/1.28) on the VSA used for the measurement shown in Fig. 5.15(b).

If it is not, the desired incoming frequencies may miss the frequency bins, and spectral leakage will occur. There is also the possibility of it causing an error in the amplitude read, as shown for two of the five peaks in Figure 5.15.

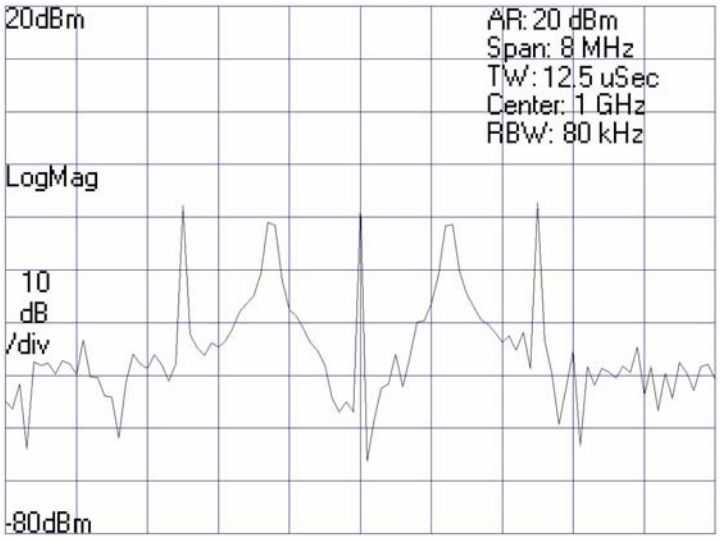

Figure 5.15: Spectral plot of a five-component multisine showing spectral leakage due to nonoptimum VSA settings [71].

Of the parameters discussed in eliminating spectral leakage, it was found that the span had the greatest impact on minimizing amplitude and phase errors for the multisine spectrum. It is however important to optimize all four parameters because measurements of small signals surrounding each sine wave could be distorted or obscured by spectral leakage.

Though not mentioned in this section, it is still important that the AR—discussed in the previous section—is set optimally for these measurements. The principles discussed previously for setting the AR apply whether measuring periodic continuous signals or aperiodic bursted signals.

5.8. Measurement in a Linear Time-Invariant Lab Environment

These next three sections cover different measurement environments and the results obtained from them. This first section covers work that was first presented in [75]. Measurements were initially done in an environment that was as controlled as possible and which allowed good repeatability. Two measurement set-ups were used to test the effects of simple channel distortion on EVM across different OFDM modulation types. Figure 5.16 gives a block diagram view of these set-ups. Figure 5.16(a) gives a simple "thru" set-up, where the only connection between the signal generator and the receiver is the cable. To simulate a more complicated transmission environment, a tuner is added, as shown in Figure 5.16(b). Since these lab set-ups have no nonlinear components or variances independent of the test signal, they were used to emulate a linear time-invariant environment.

A VSG was used to modulate signals in the IEEE 802.11a^{TM}-1999 Standard at 5 GHz. The 5 GHz signals were downconverted externally and sent to the VSA, which downconverted it to baseband and demodulated the signal. The set-up for the low-distortion case—downconverter included—ends up falling within the manufacturer's EVM specification of 1%, which is only for the path directly from the VSG to the VSA. The Agilent 89601A software package was used to demodulate signals.

The first test set-up in Figure 5.16(a) was designed to represent a low-distortion, best-case scenario for the instrumentation. In this case, the output of the VSG was fed directly to the frequency converter through a cable. For the second test in Figure 5.16(b), distortion was intentionally introduced to increase EVM. As shown in this figure, the signal from the VSG was split into two branches. One branch was fed through an

impedance tuner that introduced phase shift and distortion and the other branch through a cable. The two branches were then recombined and down-converted to 1 GHz for the VSA.

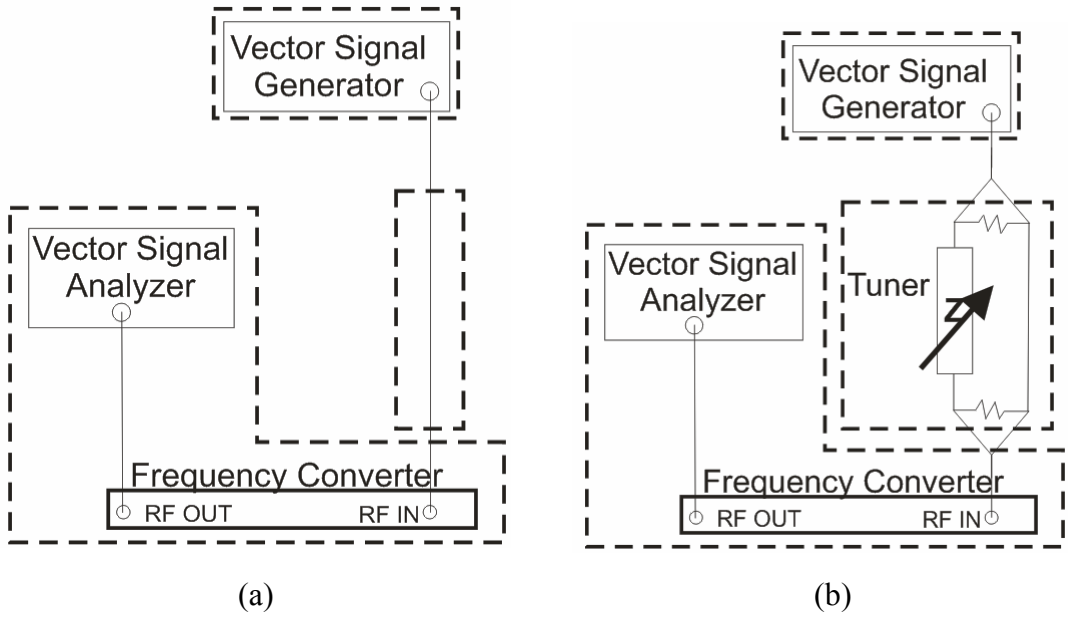

(a) (b)

Figure 5.16: Lab setup for (a) low-distortion and (b) medium-distortion setup.

Figure 5.17 shows that, though the EVM changed between the two set-ups, the EVM variation within each case, low- and high-distortion, was <0.05%. On the scale shown here, the data points resemble a straight line. The measurements demonstrate that the normalization defined by (5.9) enables direct comparison of EVM for the different modulation types for a given average symbol power. While EVM did change between the two set-ups, little change occurred between the various OFDM modulation types. QPSK gave the same EVM as BPSK, 16QAM, or 64QAM. Figure 5.6 gives an indication of why this is the case. It can be seen that since $P_0 = 1$ for both of these (QPSK and 16QAM), an error vector of the same magnitude in either case will give the same EVM.

A similar event happens for the RMS value of several error vectors. Since the signal quality is the same—as indicated by a similar EVM—QPSK is preferred over 16QAM when measuring a channel to determine its characteristics.[8] In fact, since the maximum recognizable EVM is lower for more complex modulation types, such as 64QAM (7% maximum EVM), it is preferable to use BPSK or QPSK in testing. Thus, these simpler modulation schemes become the better choice for analyzing the signal's propagation environment since they give a continuum for EVM in varied environments rather than the more typical pass/fail type of behavior of more complicated modulation schemes. It is much preferred then to use the more robust QPSK in this case than the 16QAM signal. These results were in keeping with the analysis of the 802.11a Standard's EVM equation in Section 5.3.

EVM was measured using the VSA for all of the modulation types used in the 802.11a Standard. Results for the lower- and higher-distortion set-up are shown in Figure 5.17. For each measurement of the low-distortion case, the VSA received an average symbol power of ~1.77 μW (9.41 ± 0.04 mV_{rms} across 50 Ω) with all 48 data subcarriers set to the same modulation format. For each measurement in the high-distortion case, the VSA received an average symbol power of ~28.5 nW (1.194 ± 0.006 mV_{rms} across 50 Ω) with all 48 data subcarriers set to the same modulation format.

The relatively low increase in overall EVM for the higher-distortion case can be attributed to the cyclic prefix that the 802.11a Standard requires to minimize the effects of multipath distortion. The cyclic prefix is obtained by copying the rear part of a burst

[8] Differences in EVM for different modulation schemes may occur in nonlinear environments. For instance, when a PA is in compression, the corner symbols are distorted more than the other symbols. In this case, QPSK, which has all corner symbols, may give a higher EVM than 64QAM, in which only four of its 64 symbols would be distorted. This has not been verified either way by the author.

and attaching it to the front. This allows any carry-over energy due to multipath effects or ISI from a previous burst to fall into the cyclic prefix and not into the main signal. This mitigates interference effects on the symbols from which EVM is calculated. Thus, any carry-over energy from a previous burst will have little effect on EVM if it falls into the cyclic prefix.

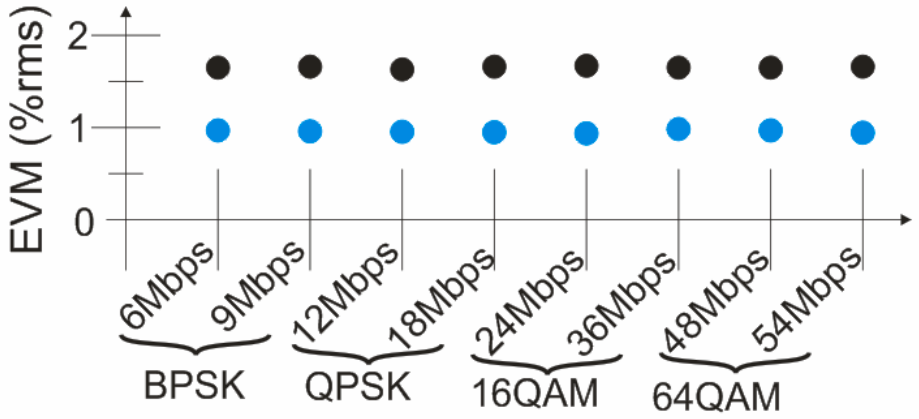

Figure 5.17: EVM for the modulation types used in the 802.11a Standard for (blue) a low-distortion case and (black) a higher-distortion case using a two-path channel and tuner.

5.9. Measurement in a Linear Time-Varying Multipath Environment

In Section 5.8, the same level of EVM was calculated in an LTI environment for various OFDM modulation types, and it was found to be independent of the OFDM modulation type. Finding anywhere near this consistency of measurement results in a multipath environment is much more difficult.

With the lab measurements in which the signal passed through cables, there were no changes in the received signal that were independent of the input signal. But for the time-varying environment, many more variables are added to the experiment. Nearly all

these additional variables were due to the channel, which was multipath. Multipath is where, due to diffraction, reflection and refraction, a signal takes more than one path to reach its destination—similar to the echo effect in a canyon. These paths also tend to change between signal bursts in ways unrelated to the signals themselves. Since these paths vary in time independent of the signal, they are called time varying.

These variances in the channel affect the received signal significantly. These cause differences between the measurements due to the time variance in the multipath. There were differences mainly between modulation types and not so much within the same modulation type. The different EVM results between modulation types can be attributed in large part to the movement of the receiving antenna between measurements of different modulation types. Specifically, the antenna was swept a full 360° before changing to another modulation type. This technique ruined repeatability by changing the multipath characteristics entirely. A change in antenna position of even a small distance, like 1 cm, changes the phase relationship between the various signal echoes and thus can change the received signal power by multiple tens of decibels [47]. The graphs of fast fading in Chapter 4 illustrate this. In addition, the multipath itself varied between each measurement causing further differences. The fix for this time variance is illustrated in Sect. 5.10.

Since the VSG and VSA were too far apart to synchronize at 10 MHz, they had to be left unsynchronized. The lack of synchronization between transmitter and receiver also increases the EVM. However, lab tests showed that this raised the EVM consistently for all the OFDM modulation types and does not nullify their comparison.

Figure 5.18 maps out the multipath environment measured in this work. Figure 5.19 gives pictures of the measurement site. A directional antenna, which ranged from about 6 dBi at 2.4 GHz to about 30 dBi at 5.2 GHz,[9] was used to transmit signals down a 100' tunnel. This allowed the signal to be focused down the tunnel and limited the multipath effects to the tunnel and the room with the receiver. Signals were received by another directional antenna in the room at the other end of the tunnel. The receiving antenna was purposely set to eliminate any line-of-sight path with the transmitter. The directional antenna used at the receiver was rotated from 0 to 330° to measure the EVM at various angles. This gave a good scattering environment that was more generally applicable to the environment of a mobile transceiver [47].

The 2.4 GHz band is an unlicensed band generally used for wireless LAN communication. The 4.9 GHz band is a new band opened for Public Safety to use when operating in the midst of an emergency. Since this work required multipath measurements at both of these frequencies, the work in this section reflects that.

Figures 5.20 and 5.21 display the results for EVM for these multipath experiments. Though there is closer agreement for both the more- and less-direct paths at 2.412 GHz than at 4.95 GHz, it is evident that the EVM does not show the same level of agreement between modulation schemes (64QAM and QPSK for this experiment) as it did in the lab. It is also interesting that from 30-150°, which is in the general direction of the tunnel opening, there is better agreement between the two OFDM modulation types. Overall, however, it could not be said that an EVM calculation taken for QPSK would be

[9] $G_0 = 32ab/\left(\pi\lambda^2\right)$, where $a \cong 6"$ and $b \cong 8-12"$ [97].

equivalent to one taken for 64QAM. The many variations in the multipath environment ensured this outcome.

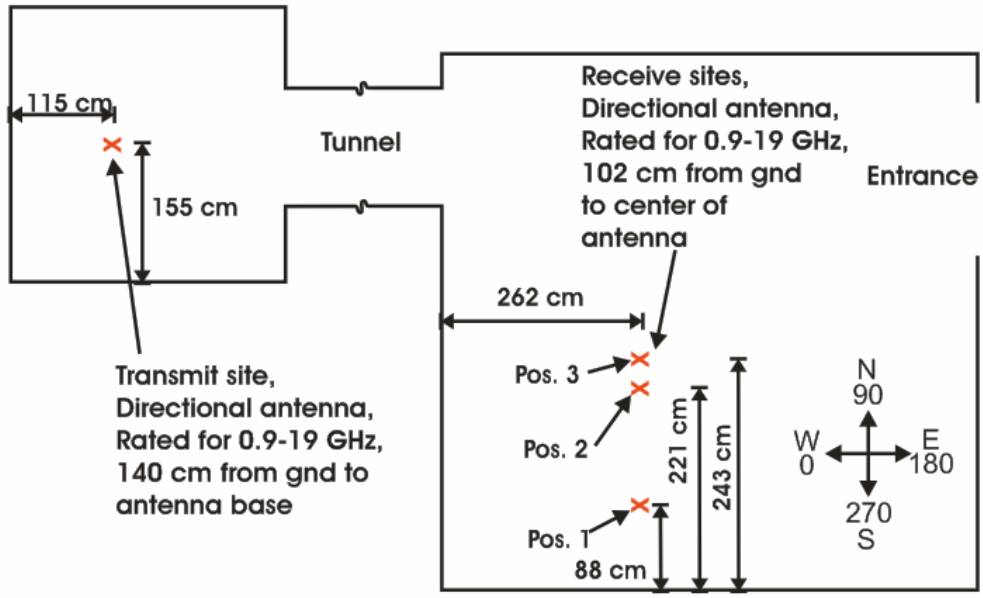

Figure 5.18: Multipath measurement setup at 2.412 and 4.95 GHz.

(a) (b) (c)

Figure 5.19: Pictures of multipath environment. View from the transmit sight (a). Line-of-sight view from the other end of the tunnel (b). Receiver in Position 3 (towards the middle of the room) (c).

5.10. Measurement in a Linear Quasi-Time-Invariant Multipath Environment

In the section covering the LTI environment, a well-controlled environment was used, and it was easy to see that different OFDM modulation types gave the same EVM. In the last section on multipath, it was pointed out that this environment easily adds its own time variance to the signal transmitted through it. The result was that the received signals changed stochastically at nearly every measurement point and made it impossible to directly compare EVM values for different modulation schemes.

There are two fairly straightforward ways to reduce or eliminate time variance from the measurement. One is to take the samples of sequential signals before the channel changes. This turns the time-varying channel into a time-invariant channel. This is the modeling approach taken by [66] when simulating multipath. In this case, the channel is considered quasi-static [65]. This is also the method used by an 802.11a-based system when it precedes the data subcarriers with the pilot subcarriers [63].

The second method is to take great pains to ensure the multipath environment is stable over a longer period of time. This was the approach used here. The same multipath environment and the same measurement equipment were used. However, the technique when measuring was changed. Though the environment remained multipath, the time variance was removed as far as possible. The main focus was on eliminating the effects of the operator's body in the building and keeping the antenna at the same position and angle until all the OFDM and multisine measurements were completed. Since this setup differs slightly from the one in Section 5.9, a new diagram of the layout is presented in Figure 5.22. Though this figure includes line-of-sight measurements, the focus of this work was on the two non-line-of-sight/multipath receiver positions in this section.

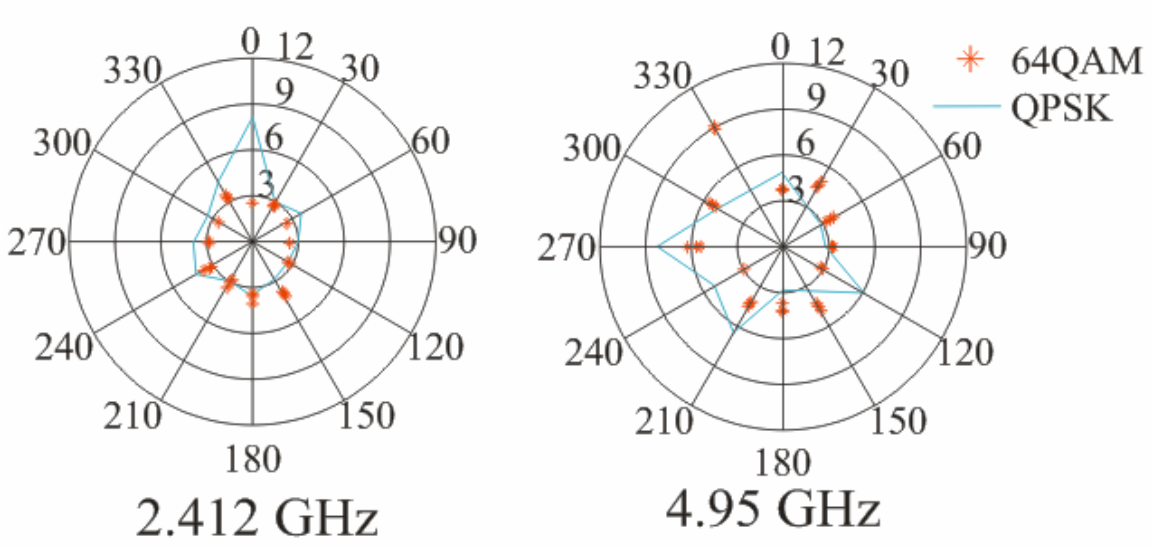

Figure 5.20: EVM calculations for QPSK and 64QAM for first receiver position, which gives the signal a less direct path to the receiver. The radial scale is in percent EVM. The angle is in degrees.

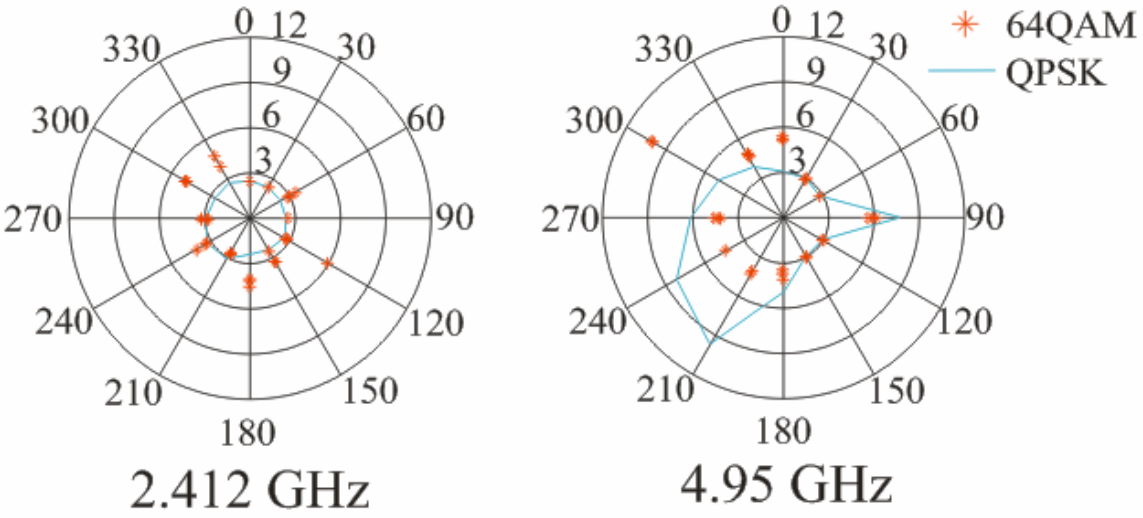

Figure 5.21: EVM calculations for QPSK and 64QAM for second receiver position, which gives the signal a more direct path to the receiver. The radial scale is in percent EVM. The angle is in degrees.

A perfect reduction of time variance due to the multipath environment was not achieved. Thus, this is labeled as a linear, quasi-time-invariant (LQTI) environment. It is a multipath with a high amount of stability to give reasonably repeatable measurements.

In [47], the author calls this a static multipath for the narrow-band case. To test how effectively this reduced time variance, three measurements each of QPSK and 64QAM signals were taken. The antennas were rotated from 0 to 330° at positions 1 and 2, as illustrated in Figure 5.22. The results are shown for both of these positions at 2.412 and 4.95 GHz in Figures 5.23 and 5.24.

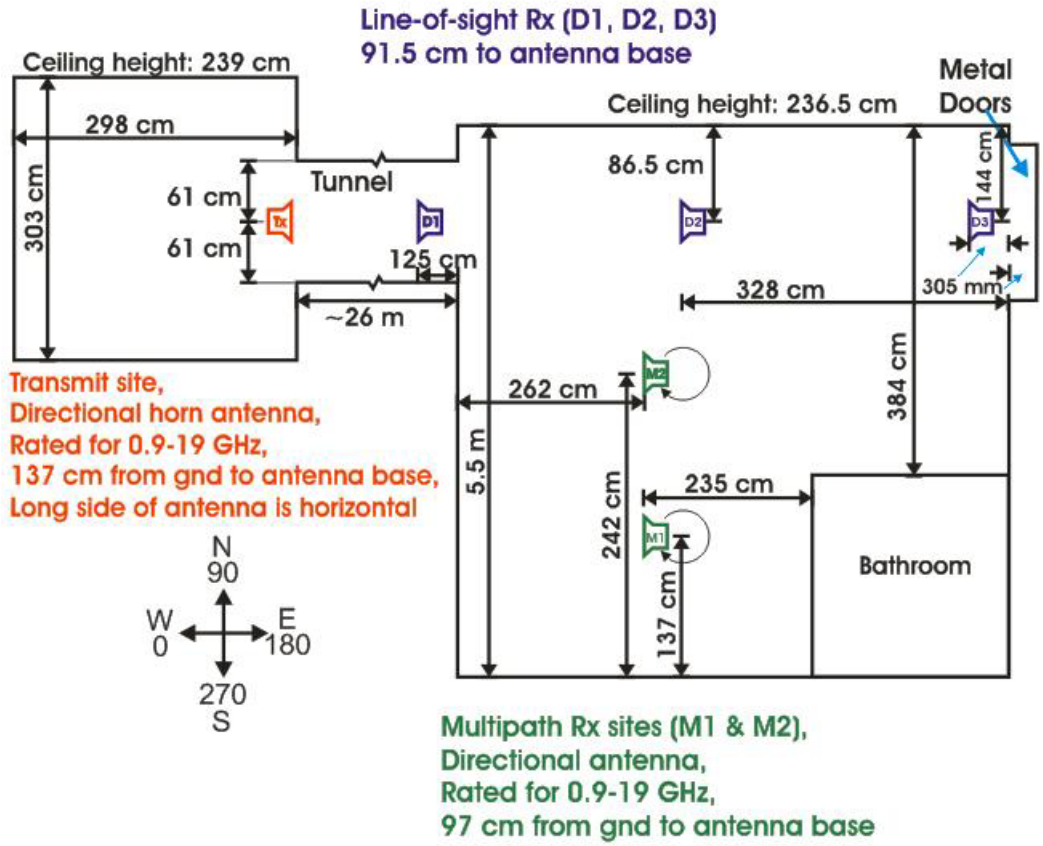

Figure 5.22: Diagram of multipath environment for LQTI measurements.

In both cases the QPSK and the 64QAM EVM values track well at most angles, an exception to this being the cases where the EVM values exceed 10%. The EVM values track a little better at 4.95 GHz than they do at 2.412 GHz, and the EVM at 4.95 GHz also tends to be less than the EVM at 2.412 GHz. However, the graphs show the EVM for

QPSK and 64QAM are sufficiently similar when the EVM is under 10% to say the EVM for QPSK could predict the EVM for 64QAM in this region, as could be expected from theory and lab measurements.

Due to the number of variables in a multipath environment, the similarity of EVM between different modulation types will not be as apparent as it was in the lab experiments. Even without time variance, the signal received out of a multipath environment is still highly distorted due in part to interference from all the signal copies.

Thus far, OFDM signals have been used in the measurements to verify repeatability of measurements and comparability of the EVM. Now, the EVM from an OFDM will be compared to the MEVM from a multisine with the same PDF. Since MEVM had to be calculated later in the lab, some comparison was needed to determine whether the multisine and the OFDM signal were behaving similarly. This was determined by looking at the spectra of the two signals. It was found that the multisine and the OFDM signal would acquire nulls in the same area of the band when there was no time variance in the multipath environment. If there were any time variance to the environment, the nulls would shift to a different part of the band. After ensuring a stable environment, the EVM for the QPSK signal was acquired and then the magnitude and phase data for the multisine. Back in the lab, the multisine phases were derotated using the program Detrendo [82] and their magnitudes normalized. Since the initial magnitude and phase settings of the multisine were known, they were used as the ideal symbols. MEVM was then calculated in the same way as EVM. Figures 5.25, 5.26 and 5.27 give the results for the two receiver positions at 2.412, 4.95 and 5.2 GHz, respectively.

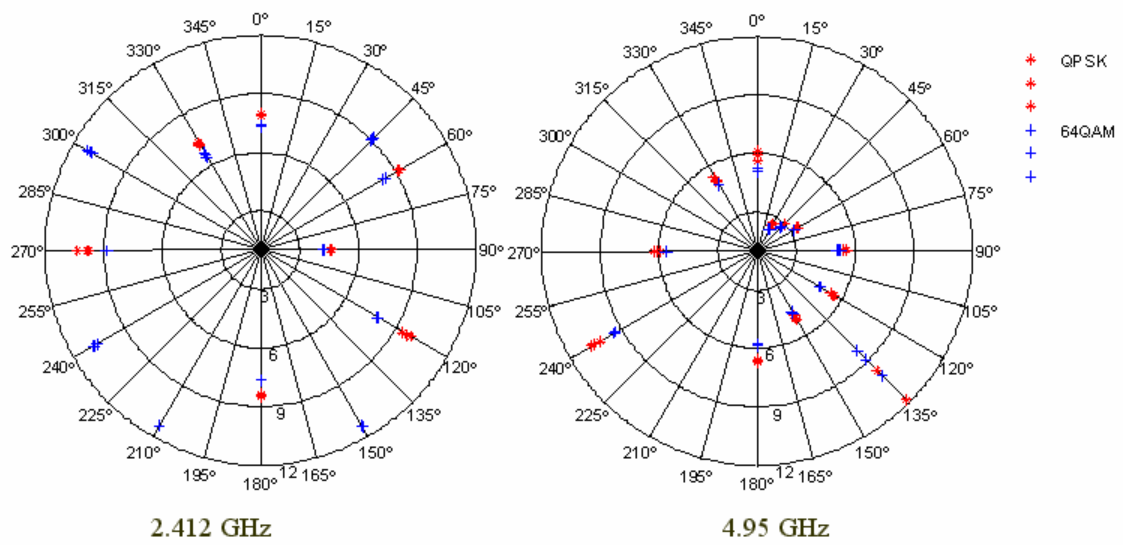

Figure 5.23: Multipath position one, which is farthest from the tunnel opening. This displays EVM results for QPSK and 64QAM signals at 2.412 and 4.95 GHz for this position. The radial scale is percent EVM.

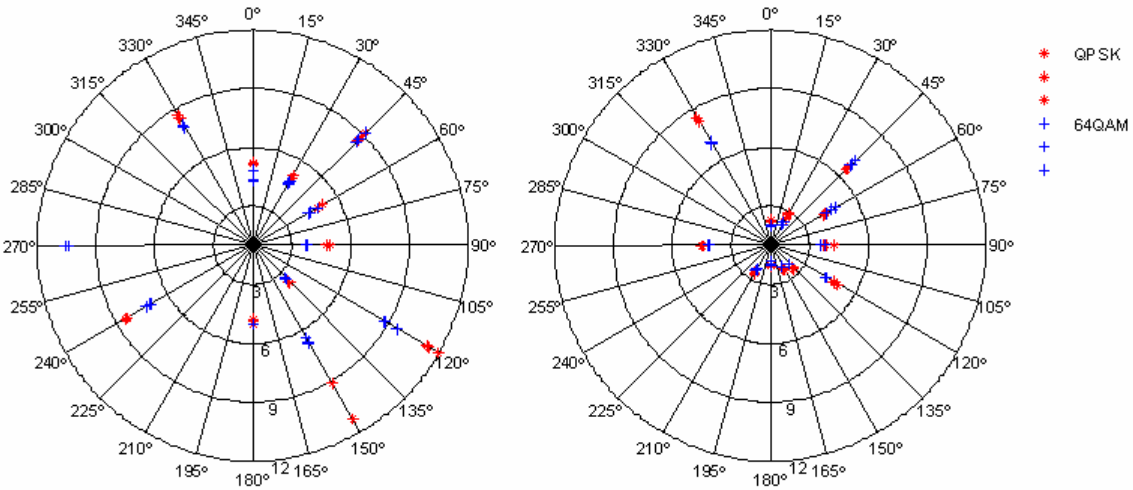

2.412 GHz 4.95 GHz

Figure 5.24: Multipath position two, which is closest to the tunnel opening. This displays EVM results for QPSK and 64QAM signals at 2.412 and 4.95 GHz for this position. The radial scale is percent EVM.

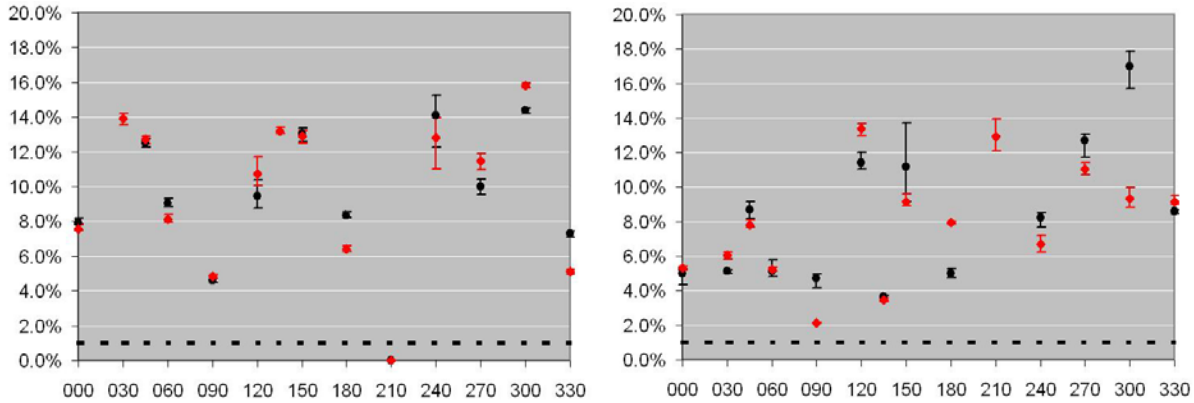

(a) (b)

Figure 5.25: EVM (black) and MEVM (red) results at 2.412 GHz for the position farthest from (a) and closest to (b) the tunnel opening.

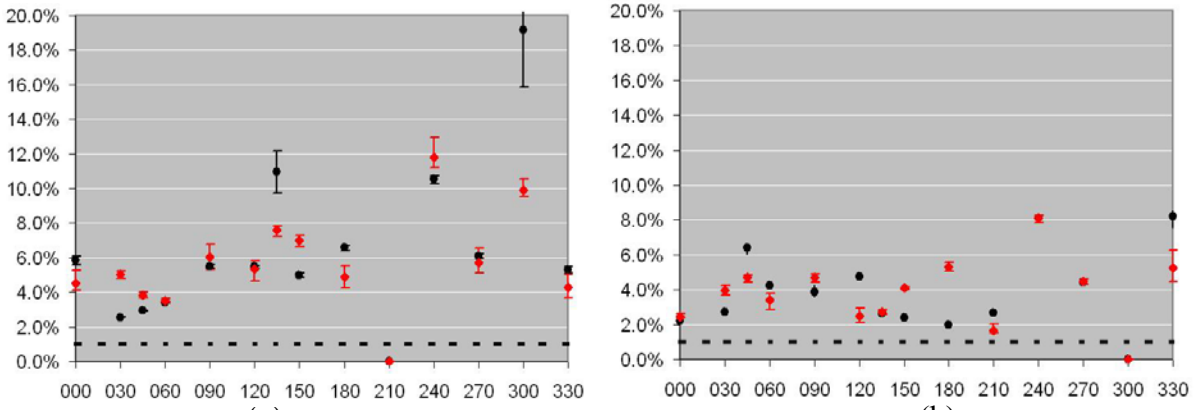

(a) (b)

Figure 5.26: EVM (black) and MEVM (red) results at 4.95 GHz for the position farthest from (a) and closest to (b) the tunnel opening.

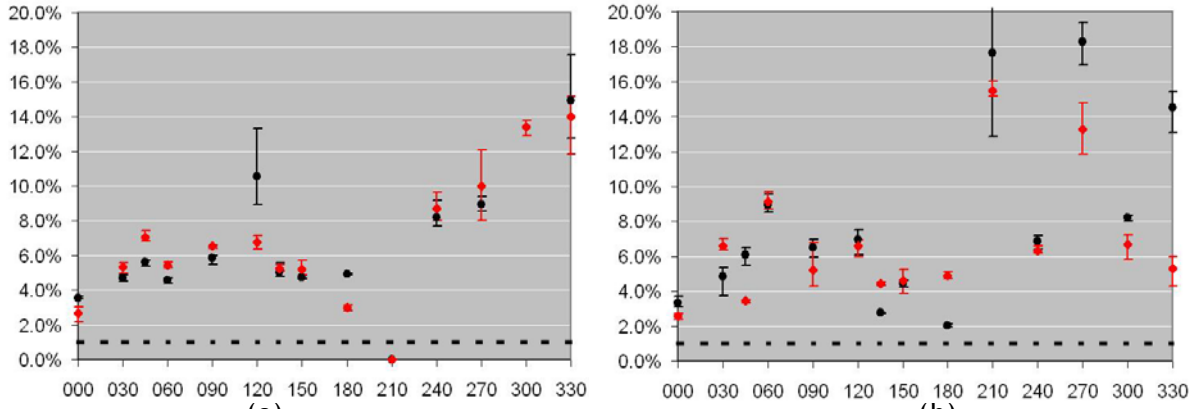

(a) (b)

Figure 5.27: EVM (black) and MEVM (red) results at 5.2 GHz for the position farthest from (a) and closest to (b) the tunnel opening.

After the filter and pulse detector, the VSA performs a coarse frequency offset estimation and timing synchronization with the symbols of the received signal. If the SNIR is too high, the VSA is not able to recover the correct symbol timing. If the VSA cannot accurately lock onto the symbols, the resulting error vectors increase significantly as the VSA is unable to accurately map the symbols on the constellation diagram.

Furthermore, since the VSA normalizes the received symbols before plotting them onto the constellation diagram, the VSA compensates for the decrease in signal power by increasing the multiplication factor used to normalize the symbols. Along with magnifying the symbols, this also magnifies the error vectors. Thus, the combination of signal corruption, SNIR degradation and poor time synchronization with the received symbols work together when multipath signals add significant interference power to the received signal to give a 2-3x increase in EVM.

Other than the cases when EVM is greater than about 15%, the MEVM data points lined up with the EVM data points to within 1-2% in most cases. Also notice that in most cases EVM and MEVM follow the same trend. Though a difference of 1-2% may seem like a large error, comparing QPSK to 64QAM in the same multipath environment rarely gives much better agreement. In other words, if the EVM from a QPSK measurement was used to predict the EVM of 64QAM in that environment, it would differ from the actual by 1-2% in most cases and up to 3% in some cases. Thus, the MEVM tracked with the EVM surprisingly well.

It should be noted that MEVM, though calculated initially in the same way as EVM, did need an additional step before being compared to EVM. MEVM needed a

scaling factor, N, to compare it to EVM. As will be recalled, this is related to the ability of the receiver to reduce the ISI in the OFDM signal using its cyclic prefix.

Though more work would have to be done to confirm and refine how N relates to K, some intuitive connections can be made. For instance, N was found to be typically higher for 0-150° than for 180-330°, as shown in Table 5.2. This would fall in line with 0-150° having less scatter and thus a higher K factor and with 180-330° having more scatter and thus a lower K factor. The scaling factor N was found empirically by programming a simplified least-squares method into Matlab. This program compared EVM data points that were less than 15%, in most cases, to their corresponding MEVM points for various scaling factors. The scaling factor that gave the least amount of error was used.

To obtain this scaling factor *a priori*, the relationship between the K (that is, the ratio of the dominant signal component to the noise and CCI) given by OFDM (K_{OFDM}) and the K (that is, the ratio of the dominant signal component to the noise, ISI and CCI) given by the multisine (K_{MSINE}) would have to be clarified. Thus, the effect of ISI would have to be determined. Since ISI increases as the LOS distance between transmitting and receiving directional antennas approach the distance covered by the cyclic prefix (~240 m), several measurements of the OFDM and multisine signals could be taken while increasing the distance between the antennas in a linear quasi-time-invariant channel. As the distance increases, it spans more of the maximum length covered by the cyclic prefix and the rms delay spread of the signal increases, which causes the ISI to increasingly become a factor in EVM. This experiment should allow insight into the relationship between K_{OFDM} and K_{MSINE} in terms of ISI. Since K_{OFDM} and K_{MSINE} relate inversely to

EVM and MEVM, this relation could possibly allow the prediction of EVM from MEVM. Experiments like this, but related strictly to the Rician *K*, are discussed in [83].

Table 5.2: Scaling factors for MEVM.

Frequency	Position of Rx	Angle of Rx	Scaling Factor (N)
2.412 GHz	M1	0-150°	4.5
2.412 GHz	M1	180-330°	3.4
2.412 GHz	M2	0-150°	5.7
2.412 GHz	M2	180-330°	4.4
4.95 GHz	M1	0-150°	6
4.95 GHz	M1	180-330°	4.9
4.95 GHz	M2	0-150°	10
4.95 GHz	M2	180-330°	7.7
5.2 GHz	M1	0-150°	7.3
5.2 GHz	M1	180-330°	3.9
5.2 GHz	M2	0-150°	6.8
5.2 GHz	M2	180-330°	3.7

These different scaling factors also point to the usefulness of directional antennas at the receiver. In typical mobile environments, the mobile device uses an omni-directional antenna, which is used to detect vertically-polarized electric fields [47]. However, it can cloud the description of a multipath channel since this can result in mixing of various fading modes from various sets of angles on the receiving end. For instance, for one set of angles upon which the received signal impinges on the antenna, it may appear to have Rayleigh-type behavior. For another set of angles, it may appear to have Rician-type behavior. Since different environments affect the signal differently, the directional antenna was used on the receiving end to help resolve the different environments. The directional antenna was used on the transmitting end to isolate the signal from the room where the transmitter was located so that it would include only the effects of the tunnel and the room with the receiver.

5.11. Summary and Conclusions

This section focused on measurement accuracy in multipath environments. OFDM was introduced first, and it was shown how it simultaneously obtains a high data rate and a compact bandwidth. Using coding and many subcarriers operating at slow data rates, it is able to effectively combat fading in a multipath channel. Its advantages come at the cost of a high peak-to-average ratio and strict timing requirements.

EVM was introduced as a figure of merit for OFDM that has both digital and analog representations but is mainly analog when summarizing the quality of a received signal. Through normalization of the received ideal and measured symbols, the EVM value remains the same for all OFDM modulation types when both signals have the same channel parameters.

To compare a multisine to an OFDM signal, an extraction algorithm developed by Pedro was used to give a 55-tone multisine the same PDF as a corresponding OFDM signal. Since EVM is a vector comparison of ideal and measured symbols, a similar figure of merit was developed for the multisine and was called MEVM. Initially, MEVM is calculated in the same way as EVM. After the initial calculation, MEVM required the additional step of scaling after which it lines up reasonably well with EVM.

Even though the figures of merit for OFDM and the multisine are similar, the measurement setup for these two signals is different. The OFDM signal is bursted and aperiodic. As such, it needs time-domain windowing to prevent its spectrum from smearing. Also, it needs special software to demodulate the signal. In this process, the equipment was found to have, at certain power levels, “sweet spots” where measurements were cleanest. For the multisine, its periodicity eliminated the need for windowing when

proper care was taken on the setup. This allowed the magnitudes and phases of the multisine to be read directly without any special computation.

In regard to the measurements, it was found that a cable connection between the VSG, the downconverting tuner and the VSA gave a good stable LTI environment where the EVM was found to remain the same no matter the OFDM modulation type received. In regard to the multipath environment, it was found that the time variance in this environment made the measurements unrepeatable, and the results for different modulation types appeared quite different from each other. Using greater care in the measurements, the time variance in the multipath was reduced enough to find that QPSK and 64QAM did indeed give very similar EVMs in cases where the EVM did not exceed about 10%. It was also found that MEVM could be made to line up nicely with EVM with proper scaling.

Chapter 6: Summary and Suggestions for Future Work

This work focused on reducing or fixing measurement inaccuracies to which models and figures of merit are susceptible in two common distortion environments for microwave communication systems: power amplifier and multipath. Since models emulate the performance of systems and figures of merit rate the performance of systems, the data used to generate them must be as clean as possible.

Enhanced measurement techniques and a new figure of merit to aid in the analysis of these wireless communication systems were proposed. It was demonstrated that periodic and digital, bursted signals could be compared, directly and indirectly, using models and/or figures of merit in power amplifier and multipath environments. This was verified by comparing figures of merit directly extracted from measurement and through extracting models from measurements. A summary of these projects follows.

The first distortion environment was the power amplifier, which created a nonlinear time-invariant distortion environment. The second was multipath, which created a linear time-varying distortion environment. To aid the multipath measurement, the linear time-varying environment was made into a linear quasi-time-invariant environment.

For the PA, nonlinear modeling is important. To improve the speed of the modeling response and reduce the modeling complexity, behavioral models are often used. Most behavioral models have some basis in the Volterra series model. This model shows the effect on the IMD of fluctuations in the fundamental tones of a two-tone signal. A simplification of Volterra that allows the modeling of long-term memory effects is the parallel Wiener model.

A high power (i.e., $P_{IN} > 10$ dBm) two-tone measurement method was developed to ensure a P_{IN} to within 0.1 dB over a 5 MHz wide frequency band and over tens of decibels of power. In addition, it greatly reduced the number of glitches and eliminated sharp transitions in the power measured by the SA. An earlier version of this test setup demonstrated experimentally what Volterra showed theoretically that fluctuations in the fundamental tones of a two-tone signal will obscure memory effects in the IMD. In the end, fluctuations in the fundamental tones were reduced from 0.3 dB to 0.05 dB, which allowed greatly improved IMD measurement accuracy. Measurement of the PA without the calibration gave such different IMD data so as to make the calibrated and uncalibrated sets of data appear to come from two separate power amplifiers.

These measurements allowed the extraction of a parallel Wiener model that included these low-level memory effects. This precise model allowed 4 dB of increased

accuracy in ACPR prediction over the quasi-memoryless model for a power amplifier driven by a CDMA signal. This allowed the demonstration through modeling that memory effects show similar intrinsic behavior for a given nonlinear system whether it has CDMA or a range of two-tone signals passing through it. The predicted ACPR from the model agreed well with that of the CDMA signal.

The next part of this research shifted from measuring PAs to measuring multipath environments. The bandwidth was widened to 16.6 MHz, the speed of measurement (instant for each power level) was improved by using a multisine instead of a swept two-tone. It also enabled the acquisition of phases and allowed a direct comparison of the figures of merit of periodic (multisine) and digital bursted (OFDM) signals. This method required no synchronization or triggering between the source and the receiver, which is a necessity in multipath measurements where the transmitter and receiver are often too far apart to make triggering or synchronization practical. An EVM normalization process that enables the calculation of an EVM that is independent of the modulation type used was demonstrated analytically. This was confirmed experimentally in an LTI (lab) and an LQTI (multipath) environment. A VSA setup that gave distortion-free multisine measurements of periodic signals in both time and frequency and in the absence of filtering was detailed. This method eliminated spectral leakage and minimized the distortion from the ADCs in the VSA, which allowed the measurement of a multisine in a multipath environment with minimal distortion from the measurement equipment.

Though having a basic understanding of propagation modeling is important, this multipath measurement method focused on a direct comparison of figures of merit from an OFDM signal and a multisine. Even with the aforementioned minimization, the

measurements could only be directly compared after minimizing the time variant nature of the environment.

Some possible topics for future research are the following: The two-tone measurement is a time-consuming measurement. Taking the thru run into account, it typically takes two days to perform one set of measurements. Furthermore, only amplitude could be measured. A great deal of time could be saved by developing a method for model extraction from multisine measurements. The inclusion of phase along with amplitude data would allow greater insight into how the upper and lower IMD products relate.

A great challenge in studying thermal memory effects is measuring the temporal thermal dispersion of the PA. This would aid in the accurate mapping of thermal transients in the device. Also, this would aid in separating memory effects due to DC bias from those due to thermal and would give insight into the dynamic nature of thermal dispersion on memory effects.

This work showed that the digitally-bursted OFDM and periodic multisine could be compared in the multipath environment via EVM and MEVM. It could easily be extended to compare them in the PA environment. Also, it would be useful to predict the scaling factor in the MEVM/EVM equation without having to measure a digital bursted signal. This would require a correlation of N to the environment being measured such that N could be determined *a priori* and without empirical scaling. Suggestions for an experiment to do this are given in Sect. 5.10.

A powerful tool in nonlinear analysis of two-port devices, especially when operating under large-signal conditions, is the LSNA. The LSNA extends the capability

to measure PAs beyond the small-signal S-parameter ability of the VNA and into the large-signal operation region of the device to give a more complete picture of its nonlinear behavior. However, the LSNA is limited to measuring periodic signals. Since the behavior of the DUT depends on the characteristics of the signal applied to it, a signal that is periodic and yet would cause the DUT to operate as if a digital, bursted signal were applied to it would be needed. With the multipath work showing a good comparison between the multisine and the OFDM signal, the DUT measurements could now be extended to the LSNA.

Bibliography

[1] S. C. Cripps, *RF Power Amplifiers for Wireless Communications*, Boston, MA: Artech House, 1999.

[2] H. Ku, "Behavioral modeling of nonlinear RF power amplifiers for digital wireless communication systems with implications for predistortion linearization systems," Ph.D. Dissertation, Georgia Institute of Technology, Oct. 2003.

[3] C. P. Silva, C. J. Clark, A. A. Moulthrop and M. S. Muha, "Survey of characterization techniques for nonlinear communication components and systems," *2005 IEEE Aerospace Conference*, pp. 1713-1737, Sept. 2005.

[4] C. J. Clark, C. P. Silva, A. A. Moulthrop and M. S. Muha, "Power-amplifier characterization using a two-tone measurement technique," *IEEE Trans. Microwave Theory and Tech.*, vol. 50, no. 6, pp. 1590-1602, June 2002.

[5] S. A. Maas, *Nonlinear Microwave and RF Circuits*, 2nd Ed., Boston, MA: Artech House, 2003.

[6] M. Schetzen, *The Volterra and Wiener Theories of Nonlinear Systems*, Malabar, FL: Krieger Publishing Company, 1980.

[7] N. M. Blachman, "Bandpass nonlinearities," *IEEE Trans. Inform. Theory*, vol. IT-10, pp. 162-164, Apr. 1964.

[8] N. M. Blachman, "The signal x signal, noise x noise, and signal x noise output of a nonlinearity," *IEEE Trans. Inform. Theory*, vol. IT-14, no. 1, pp. 21-27, Jan. 1968.

[9] N. M. Blachman, "Detectors, bandpass nonlinearities, and their optimization: Inversion of the Chebyshev transform," *IEEE Trans. Inform. Theory*, vol. IT-17, pp. 398-404, July 1971.

[10] R. Blum and M. C. Jeruchim, “Modeling nonlinear amplifiers for communication simulations,” *ICC89*, Boston, MA, pp. 1468-1472, 1989.

[11] S. C. Cripps, *Advanced Techniques in RF Power Amplifier Design*, Boston, MA: Artech House, 2002.

[12] P. Crama and J. Schouken, “Wiener-Hammerstein system estimator initialisation using a random multisine excitation,” *58th ARFTG Conf. Dig.,* Dec. 2001.

[13] Y. Zhang and S. Li, “Parameter identification for Wiener model using particle swarm optimization with a case study,” *IEEE Int’l. Conf. on Automation and Logistics*, pp. 1725-1730, 2007.

[14] S.-L. Chang and T. Ogunfunmi, “LMS/LMF and RLS Volterra system identification based on nonlinear Wiener model,” *Proc. of the 1998 IEEE ISCAS*, pp. 206-209, 1998.

[15] S.-L. Chang and T. Ogunfunmi, “Performance analysis of third-order nonlinear Wiener adaptive systems,” *Proc. of the 2002 IEEE ISCAS*, vol. 2, pp. 197-200, 2002.

[16] H.-X. Li, “Identification of Hammerstein models using genetic algorithms,” *IEE Proc. Control Theory and Applications*, vol. 146, pp. 499-504, Nov. 1999.

[17] G. Belforte and P. Gay, “Hammerstein model identification with set membership errors,” *1999 Proc. of the 38th IEEE Conf. on Decision and Control*, pp. 592-597, 1999.

[18] W. Greblicki, “Continuous-time Hammerstein system identification from sampled data,” *IEEE Trans. on Automatic Control*, vol. 51, pp. 1195-1200, Jul. 2006.

[19] H. H. J. Bloeman, T. J. J. van den Boom and H. B. Verbruggen, “Model-based predictive control for Hammerstein systems,” *Proc. of the 39th IEEE Conf. on Decision and Control*, pp. 4963-4968, 2000.

[20] P. Crama and J. Schoukens, “Initial estimates of Wiener and Hammerstein systems using multisine excitation,” *IEEE Trans. on Instrumentation and Measurement*, pp. 1791-1795, 2001.

[21] P. Crama and J. Schoukens, “First estimation of Wiener and Hammerstein systems using multisine excitation,” *Proc. of the IMTC*, pp. 1365-1369, 2001.

[22] A. Krzyak, J. Z. Sasiadek and B. Kegl, “Identification of nonlinear systems by Hermite series approach,” *Proc. of the 40th IEEE Conf. on Decision and Control*, pp. 2143-2144, 2001.

[23] E.-W. Bai and M. Fu, “A blind approach to Hammerstein model identification,” *IEEE Trans. on Signal Processing*, vol. 50, pp. 1610-1619, Jul. 2002.

[24] J. Jeraj and V. J. Mathews, “A stable adaptive Hammerstein filter employing partial orthogonalization of the input signals,” *IEEE Trans. on Signal Processing*, vol. 54, pp. 1412-1420, Apr. 2006.

[25] J. Jeraj, V.J. Mathews and J. Dubow, “A stable adaptive Hammerstein filter employing partial orthogonalization of the input signals,” *Proc. of ICASSP*, pp. 1349-1352, 2002.

[26] A. Balestrino and A. Caiti, “Approximation of Hammerstein/Wiener dynamic models,” *Proc. of the IEEE-INNS-ENNS*, pp. 70-74, 2000.

[27] Y. Tingqi, L. Changlu and L. Wenjiang, “Identification of Hammerstein model based on dynamical separation technology,” *Proc. of the 3rd World Congress on Intelligent Control and Automation*, pp. 2124-2128, 2000.

[28] E.-W. Bai and M. Fu, “A blind approach to Hammerstein model identification,” *Proc. of the 40th IEEE Conf. on Decision and Control*, pp. 4794-4799, 2001.

[29] W. Jang, “Modeling asymmetric distortion in multichannel radio frequency communication systems,” Ph.D. Dissertation, North Carolina State University, 2006.

[30] P. Crama and J. Schoukens, “Wiener-Hammerstein system estimator initialisation using a random multisine excitation,” *58th ARFTG Conf. Dig.*, pp. 1-6, 2001.

[31] P. Crama and J. Schoukens, “Computing an initial estimate of a Wiener-Hammerstein system with a random phase multisine excitation,” *IEEE Trans. on Instrumentation and Measurement*, vol. 54, pp. 117-122, Feb. 2005.

[32] P. Crama and Y. Rolain, “Broad-band measurement and identification of a Wiener-Hammerstein model for an RF amplifier,” *60th ARFTG Conf. Dig.*, pp. 49-57, 2002.

[33] M. Schetzen, “Nonlinear system modeling based on the Wiener theory,” *Proc. IEEE*, vol. 69, no. 12, pp. 1557-1573, Dec. 1981.

[34] D. T. Westwick and R. E. Kearney, “Use of eigenvector expansions in generalized Wiener system models,” *Proc. of the 16th Annual Int’l. Conf. of the Engineering in Medicine and Biology Society*, pp. 1328-1329, 1994.

[35] D. Silveira, M. Gadringer, H. Arthaber, M. Mayer and G. Mageri, “Modeling, analysis and classification of a PA based on identified Volterra kernels,” *European Gallium Arsenide and Other Semiconductor Application Symp.*, pp. 405-408, 2005.

[36] H. Ku and J. S. Kenney, “Analysis of ACPR performance for memoryless predistorter considering power amplifier memory effects,” in *IEEE MTT-S Int. Microwave Symp. Dig.,* vol. 1, pp. 1863-1866, June 2004.

[37] L. Ding, G. T. Zhou, D. R. Morgan, Z. Ma and J. S. Kenney, “Memory polynomial predistortion based on the indirect learning architecture,” *GLOBECOM*, pp. 967-971, 2002.

[38] G. T. Zhou and J. S. Kenney, “Predicting spectral regrowth of nonlinear power amplifiers,” *IEEE Trans. on Communications*, vol. 50, no. 5, pp. 718-722, May 2002.

[39] H. Ku, M. D. McKinley, and J. S. Kenney, "Extraction of accurate behavioral models for power amplifiers with memory effects using two-tone measurements," in *IEEE MTT-S Int. Microwave Symp. Dig.,* vol. 1, pp. 139-142, June 2002.

[40] H. Ku, M. D. McKinley, and J. S. Kenney, "Quantifying memory effects in power amplifiers," *IEEE Trans. Microwave Theory and Tech.,* vol. 50, no. 12, pp. 2843-2849, Dec. 2002.

[41] J. S. Kenney and Pavlo Fedorenko, "Identification of RF power amplifier memory effect origins using third-order intermodulation distortion amplitude and phase asymmetry," in *IEEE MTT-S Int. Microwave Symp. Dig.*, pp. 1121-1124, June 2006.

[42] M. D. McKinley, Y. Park, J. S. Kenney, and H. Ku, "Obtaining accurate IMD variation and imbalance measurements for identifying memory effects in high-power amplifiers," *62nd ARFTG Conf. Dig.*, pp. 77-80, 2003.

[43] Agilent Data Sheet, E4438C ESG Vector Signal Generator, 2003.

[44] J. K. Cavers, *Mobile Channel Characteristics*, New York, NY: Kluwer Academic Publishers, 2002.

[45] G. L. Stuber, *Principles of Mobile Communications*, 2nd Ed., Boston-London: Kluwer Academic Publishers, 2002.

[46] B. Bing, *Broadband Wireless Access*, New York, NY: Kluwer Academic Publishers, 2002.

[47] J. D. Parsons, *The Mobile Radio Propagation Channel*, 2nd Ed., New York: John Wiley & Sons, 2000.

[48] J. Y. C. Cheah, *Practical Wireless Data Modem Design*, Boston, MA: Artech House, 1999.

[49] B.P. Kumar, Class Notes for EEE 262 Wireless Communication Systems, CaliforniaState University, Sacramento, 2006.

[50] L. A Zadeh, "Frequency analysis of variable networks," *Proceedings of the IRE*, vol. 38, pp. 291-299, Mar. 1950.

[51] T. Kailath, "Sampling models for linear time-variant filters," *M.I.T. Research Laboratory of Electronics*, Cambridge, Rept. No. 352; May 25, 1959.

[52] R. G. Winch, *Telecommunication Transmission Systems*, 2nd Ed., New York, NY: McGraw-Hill, 1998.

[53] A. Silvennoinen, Class Notes for S-72.333 Postgraduate Course in Radio Communications, Helsinki University of Technology, Helsinki, Finland, 2005.

[54] N. Blaunstein and J. B. Andersen, *Multipath Phenomena in Cellular Networks*, Boston, MA: Artech House, 2002.

[55] P. Vandenameele, *Space Division Multiple Access for Wireless Local Area Networks*, Boston-London: Kluwer Academic Publishers, 2002.

[56] P. A. Bello, "Characterization of randomly time-variant linear channels," *IEEE Trans. On Comm.*, vol. 11, pp. 360-393, Dec. 1963.

[57] P. A. Bello, "Time-frequency duality," *IEEE Trans. On Information Theory*, vol. 10, pp. 18-33.

[58] G. D. Durgin, *Space-Time Wireless Channels*, Upper Saddle River, NJ: Pearson Education, 2003.

[59] http://wireless.per.nl/reference/chaptr03/fading/anspdf.htm

[60] S. O. Rice, "Mathematical analysis of random noise," *Bell Syst. Tech. J.,* vol. 23, no. 3, pp. 282-332, 1944.

[61] S. O. Rice, "Statistical properties of a sine wave plus random noise," *Bell Syst. Tech. J.,* vol. 27, no. 1, pp. 109-157, 1948.

[62] R. H. Clarke, "A statistical theory of mobile radio reception," *Bell. Syst. Tech. J.*, vol. 47, no. 6, pp. 957-1000, 1968.

[63] IEEE Standard for Wireless LAN Medium Access Control (MAC) and Physical Layer (PHY) Specifications: High-Speed Physical Layer in the 5 GHz Band, IEEE 802.11a™-1999 Standard.

[64] S. Nedic and N. Popovic, "Per-bin DFE for advanced OQAM-based multi-carrier wireless data transmission systems," *Int'l. Zurich Seminar on Broadband Comm.*, pp. 38-1 – 3 8-6, 2002.

[65] P. Luo and Y. Guan, "Optimum receiver for space-time trellis code in multipath fading channel," *Int'l. Zurich Seminar on Broadband Comm.*, pp. 43-1 – 43-5, 2002.

[66] S. Furrer and D. Dahlhaus, "Mean bit-error rates for OFDM transmission with robust channel estimation and space diversity reception," *Int'l. Zurich Seminar on Broadband Comm.*, pp. 47-1 – 47-6, 2002.

[67] Y. Gong, K. B. Letaief, "Performance evaluation and analysis of space-time coding in unequalized multipath fading links," *IEEE Trans. Comm.*, vol. 48, no. 11, pp. 1778-1782, Nov. 2000.

[68] J. S. Thompson, R. Tanner and D. Bevan, "Weight error loss for wireless systems with antenna arrays," *Int'l. Zurich Seminar on Broadband Comm.*, pp. 4-1 – 4-6, 2002.

[69] C. R. Nassar, B. Natarajan, Z. Wu, D. Wiegandt and S. A. Zekavat, *Multi-Carrier Technologies for Wireless Communications*, New York: Kluwer Academic Publishers, 2002.

[70] T. Ojanpera and R. Prasad, *WCDMA: Towards IP Mobility and Mobile Internet*, Boston: Artech House, 2000.

[71] M. D. McKinley, K. A. Remley, and J. S. Kenney, "Error Vector Magnitude for 802.11a™-1999 Systems," presented at the 2005 *Int'l. Microwave Symp. Workshop*, Long Beach, CA, June 12, 2005 (invited).

[72] IEEE Standard for Wireless LAN Medium Access Control (MAC) and Physical Layer (PHY) Specifications: Higher-Speed Physical Layer Extension in the 2.4 GHz Band, IEEE 802.11b™-1999 Standard.

[73] http://www.leearmstrong.com/DSRC/DSRCHomeset.htm

[74] Agilent Application Note, *RF Testing of Wireless LAN Products*, AN 1380-1.

[75] M. D. McKinley, K. A. Remley, M. Myslinski, J. S. Kenney, D. Schreurs, and B. Nauwelaers, "EVM calculation for broadband modulated signals," *64th ARFTG Conf. Dig.*, pp. 45-52, 2004.

[76] S. Forestier, P. Bouysse, R. Quere, A Mallet, J.-M. Nebus, and L. Lapierre, "Joint optimization of the power-added efficiency and the error-vector measurement of 20-GHz pHEMT amplifier through a new dynamic bias-controlled method," *IEEE Trans. Microwave Theory and Tech.,* vol. 52, no. 4, pp. 1132-1140, Apr. 2004.

[77] J. Schoukens and T. Dobrowiecki, "Design of broadband excitation signals with a user imposed power spectrum and amplitude distribution," *IEEE Inst. and Meas. Tech. Conf.*, pp. 1002-1005, May 1998.

[78] J. C. Pedro and N. B. Carvalho, "Statistics of microwave signals and their impact on the response of nonlinear dynamic systems," *62nd ARFTG Conf. Dig.*, pp. 143-153, 2003.

[79] J. C. Pedro and N. B. de Carvalho, "Designing band-pass multisine excitations for microwave behavioral model identification," *Int'l Microwave Symp. Dig.,* pp. 791-794, 2004.

[80] J. C. Pedro and N. B. de Carvalho, "Designing multisine excitations for nonlinear model testing," *IEEE Trans. on Microwave Theory and Tech.*, vol. 53, no. 1, pp. 45-54, Jan, 2005.

[81] M. Li, K. M. Gharaibeh, K. G. Gard, and M. B. Steer, "Accurate multisine representation of digital communication signals for characterization of nonlinear circuits," *IEEE Radio and Wireless Symp.*, pp. 527-530, 2006.

[82] K. A. Remley, "Phase detrending for measured multisine signals," *61st ARFTG Conf. Dig.*, pp. 73-83, 2003.

[83] C. Evci, M. Beach and G. Romano, "Combating multipath via directional antennas for broadband wireless ATM," *Int'l. Zurich Seminar on Broadband Comm.*, pp. 119-126, 1998.

[84] A. Leke and J. M. Cioffi, "Blind Identification of Channels for Discrete Multitone (DMT) Applications," *Int'l. Zurich Seminar on Broadband Comm.*, pp. 113-118, 1998.

[85] J. Archambault and S. Surineni, "IEEE 802.11 spectral measurements using vector signal analyzers," *RF Design Mag.*, pp. 38-49, June 2004.

[86] Tektronix Technical Brief, Modulation Analysis for Transient RF Signals.

[87] National Instruments Application Note, Perform More Effective RF Measurements Using Vector Analysis.

[88] Agilent Application Note, *The Fundamentals of Signal Analysis*, AN 243.

[89] E. O. Brigham, *The Fast Fourier Transform and its Applications.* Englewood Cliffs, NJ: Prentice Hall, 1988.

[90] R. G. Lyons, *Understanding Digital Signal Processing*, 2nd Ed. Upper Saddle River, NJ: Prentice Hall, 2004.

[91] J. C. Pedro and N. B. de Carvalho, "On the use of multitone techniques for assessing RF components' intermodulation distortion," *IEEE Trans. Microwave Theory and Tech.*, vol. 47, pp. 2393-2402, Dec. 1999.

[92] Agilent Application Note. *Vector Signal Analysis Basics,* AN 150-15.

[93] http://mathworld.wolfram.com/FastFourierTransform.html.

[94] M. D. McKinley, K. A. Remley, M. Myslinski, and J. S. Kenney, "Eliminating FFT artifacts in vector signal analyzer spectra," *Microwave Journal*, pp. 156-164, October 2006.

[95] Agilent Product Note, Time-Capture Capabilities of the Agilent 89400 Series Vector Signal Analyzers, PN 89400-10.

[96] Agilent Product Note, Understanding Time and Frequency Domain Interactions in the Agilent 89400 Series Vector Signal Analyzers, PN 89400-12.

[97] R. C. Johnson, Ed., *Antenna Engineering Handbook*, 3rd Ed., New York, NY: McGraw-Hill, 1993.